X-RAY AND ELECTRON GENERATION IN THE RELATIVISTIC LAMBDA-CUBED REGIME

by

Aghapi G. Mordovanakis

A dissertation submitted in partial fulfillment
of the requirements for the degree of
Doctor of Philosophy
(Electrical Engineering)
in The University of Michigan
2008

Doctoral Committee:

Professor Karl Krushelnick, Co-chair
Emeritus Professor Gérard Mourou, Co-chair
Professor Roy Clarke
Associate Professor Almantas Galvanauskas
Adjunct Associate Professor John Nees

إلى أمي و أبي

To my parents: George and Souad.
Without your sacrifices this would not have been possible.

ACKNOWLEDGEMENTS

First, I would like to acknowledge my advisors Karl Krushelnick and Gérard Mourou for stimulating advice and far-sighted ideas. Working with them has been especially enlightening and rewarding. Also, I wish to thank John Nees, without whose encouragement and useful advice this dissertation would not have come to a completion; Almantas Galvanauskas and Roy Clarke for their substantial contributions and for serving on my dissertation committee.

All the experiments described in this dissertation are the fruit of collaborative efforts by many researchers and fellow students to whom I am grateful. The λ^3 x-ray experiments were undertaken under the supervision of Bixue Hou who also acted as a mentor during my early days in the laboratory. The study of the x-ray source spatial coherence was a collaboration with Davide Boschetto and Antoine Rousse from the Laboratoir d'Optique Appliquée as well as Roy Clarke and Devine Kumah from the Applied Physics program.

The hot electron characterization experiments could not have been done without the help of James Easter. The corresponding simulations were performed by Paul-Edouard Masson-Laborde and Wociek Rozmus from the University of Alberta. The theoretical electron heating model discussed in chapter IV was the product of insightful communications with Malcom Haines from Imperial College.

All fiber-laser experiments were carried out in collaboration with the Galvanauskas' group: Kai-Hsiu Liao, Kai-Chung Hou and Yu-Chung Chang.

Additionally, I would like to acknowledge members of the CUOS family: Stephen

Reed, Erik Power, Takeshi Matsuoka, Pascal Rousseau, Peter Diehr and Tolya Maksimchuk for help and many insightful discussions.

The journey through grad school has been exponentially more enriching and lively thanks to the many great friends I met along the way: Mariano Trigo, Zeina Mneimneh, Imad Btaiche, Hrach Simonian, Karthick Vishwanath, Joe Pentland and the tango club crew.

Finally and most importantly, I wish to honor my father George, mother Souad and brothers Tony, Elie and Paul for their unconditional love and indefinite support, both during the happy moments and especially through the rugged time. I love you.

TABLE OF CONTENTS

LIST OF TABLES

LIST OF FIGURES

CHAPTER I

INTRODUCTION

The invention of the chirped-pulse amplification (CPA) technique [1] in the mid-eighties triggered a rapid increase in peak power achievable by ultrafast table-top lasers. Today, state of the art petawatt systems [2] can produce, in a mere 30 fs, an optical power equivalent to a thousand times the total electrical power consumption of the entire world. When focused onto a spot with 1 μm diameter, these lasers can reach intensities that exceed 10^{22} W/cm^2 [3]. At such extreme intensities, the electron quiver velocity in the electromagnetic field becomes comparable to the speed of light in vacuum, therefore, the material response can no longer be treated by classical optics and relativistic effects must be considered.

The ubiquity of ultrafast lasers capable of exceeding the relativistic regime ($\sim 10^{18}$ W/cm^2 for 800 nm light) has facilitated the exploration of extreme physics (GeV electrons, MeV protons, MegaGauss magnetic fields) and the inception of a wide array of applications (ultrafast x-ray sources, attosecond pulses for metrology). However, most relativistic laser-matter interactions have been carried out with laser systems that produce more than 100 mJ pulses and at a repetition rate of 10 Hz or lower. A less explored regime arises when millijoule femtosecond pulses are focused to a focal spot with a diameter comparable to the wavelength thus producing relativistic intensities with kilohertz rates. Experiments in this so-called relativistic λ^3 regime are discussed in the present dissertation.

1.1 The relativistic λ^3 regime

Conceptually, the λ^3 regime refers to the limit where the pulse energy is delivered over a time duration of the order of a single optical cycle ($\tau \sim \lambda/c$) and tightly focused to the diffraction limit onto an area comparable with the square of the wavelength ($A \sim \lambda^2$). Perhaps the most attractive feature of the λ^3 regime is that it makes accessible relativistic intensities with sub-millijoule pulse energies. For example, a Ti:sapphire laser ($\lambda = 800$ nm) can reach intensities as high as 3×10^{18} W/cm^2 with only 100 μJ under ideal λ^3 conditions. This allows the study of relativistic phenomena – such as electron and ion acceleration, relativistic self-focusing and pair productions – at kilohertz repetition rates [4]. High-repetition relativistic-intensity studies could be characterized by a superior signal-to-noise ratio as compared to single-shot experiments, and as such, have attracted an increasing interest among researchers in recent years [5, 6, 7, 8].

Moreover, the relativistic λ^3 regime possesses unique characteristics that distinguish it from long-pulse regimes. Simulations suggest that an ultrashort pulse could set a near-critical-density plasma into a coherent oscillatory motion which results in the emission of isolated attosecond pulses [9, 10]. This process is several orders of magnitude more efficient than attosecond generation from the high-order harmonics generated in under-dense plasmas. Additionally, due to its sharp gradients, the relativistic λ^3 regime is well suited for the generation of attosecond electron bunches [11].

In reality, however, the λ^3 conditions (single-cycle duration, single wavelength spot) are yet to be reproduced in the laboratory despite recent progress in pulse compression techniques [6, 5]. For the purpose of this dissertation, the λ^3 regime is approximated by focusing a 30 fs pulses ($\sim$ 12 cycles) onto a spot of $1.2 - 1.5$ μm FWHM ($\sim 1.5 - 2\lambda$) yielding a focal volume of about 35 λ^3. The techniques used to achieve the minute focal spot involve using a high-numerical-aperture paraboloidal

mirror along with a computer-controlled deformable mirror that optimizes the laser wavefront for the smallest focus. These techniques will be described with more details in Chapter III (section 3.3.1).

1.2 Fiber laser regime

For laser-plasma interactions that depend weakly on the laser pulse duration, for instance Kα photon production [12], results obtained in the λ^3 regime could be extended to a fundamentally different regime, that of high average-power fiber lasers. Driven chiefly by advances in large-mode-area fibers and high-brightness diodes, this rapidly emerging technology enables millijoule-energy ultrafast pulses [13] delivered at high average-powers exceeding those of conventional solid-state lasers by several orders of magnitude [14]. The robustness and stability of fiber lasers, coupled with their high-power properties, have the potential to transfer some of the key achievements of laser-plasma science at the intermediate intensities toward commercial applications that could be useful in clinical medicine, biology and semiconductor industry. It is one of the goals of the present dissertation to demonstrate, for the first time, the capability of fiber laser pulses to produce a sufficiently-high intensity for the production of x rays (in the sub-picosecond range) an extreme UV radiation (in the nanosecond range).

1.3 Dissertation outline

This dissertation is organized as follows. Chapter II introduces the mathematical formalism used throughout this dissertation and presents a brief overview of laser-plasma physics relevant in the λ^3 regime. The various standard models that describe the heating of the plasma electrons by an intense electromagnetic wave are discussed along with the theory of x-ray production by the hot electrons, both bremsstrahlung continuum and characteristic line emission.

Chapter III discusses a series of experiments aimed at characterizing the x-ray source produced by a relativistic intensity laser in the λ^3 regime. First the experimental set-up, including the λ^3 laser and the x-ray diagnostics, is described. Experimental results of the x-ray source size, obtained by the knife-edge technique, are reported for various target materials [15]. In the last section of this chapter the spatial coherence properties of a Si plasma x-ray source are investigated by measuring the diffraction pattern off a straight edge [16].

Chapter IV is dedicated to the characterization of hot electrons emitted from the plasma at relativistic laser intensities. The electron temperature scaling with the laser intensity is studied for an Al plasma in the $10^{17} - 10^{18}$ W/cm^2 intensity range. Moreover, the effect of plasma scale-length on both the spatial and energy distributions of the hot electrons is also investigated in the range $0.1\lambda < L_n \leqslant \lambda$.

In chapters V and VI are presented two pioneering experiments on the use of high peak-power fiber lasers to generate short wavelength radiation. The first of the two chapters reports on the generation of Kα photons from a Ni target using a high-energy (~ 100 μJ) fiber CPA system capable of delivering intensities as high as 2×10^{15} W/cm^2 [17]. The second chapter reports on the efficient generation of EUV radiation from a nanosecond fiber laser in the context of the next generation lithography light source [18].

The concluding chapter comments on some of the results discussed herein and suggests future directions.

CHAPTER II

THEORETICAL BACKGROUND AND FORMALISM

2.1 Laser interaction with a single electron

2.1.1 A single electron in a sub-relativistic plane wave

Consider a linearly polarized plane wave ($\mathbf{E} = \mathrm{Re}\{\mathrm{E_{x0}e^{i\omega t}}\}\hat{\mathbf{x}}$, $\mathbf{B} = \mathrm{Re}\{\mathrm{B_{y0}e^{i\omega t}}\}\hat{\mathbf{y}}$) propagating in vacuum along the z-direction. The field intensity I associated with the wave is defined as the time average of the Poynting vector over many laser cycles (average over T, where $\omega T \gg 1$):

$$\begin{aligned} I &= |\langle \mathbf{E} \times \frac{1}{\mu_0}\mathbf{B} \rangle| \\ &= \frac{1}{2\mu_0 c}|E_{x0}|^2 \end{aligned} \tag{2.1}$$

The motion of a single electron subject to this wave is then determined by the Lorentz force:

$$\frac{d\mathbf{p}}{dt} = -e\left(\mathbf{E} + \mathbf{v} \times \mathbf{B}\right) \tag{2.2}$$

where $\mathbf{p}$ and $\mathbf{v}$ are the electron momentum and velocity, respectively. At low intensities $|\mathbf{v} \times \mathbf{B}| << |\mathbf{E}|$, and the Lorentz force becomes $\mathbf{F} \simeq -e\mathbf{E}$. It is easy to see that, in this case, the electron follows an oscillatory motion strictly in the transverse direction, with a quiver amplitude and velocity given by:

$$A_{osc} = \frac{eE_{x0}}{m_e\omega^2} \tag{2.3}$$

$$v_{osc} = \frac{eE_{x0}}{m_e\omega} \tag{2.4}$$

In practical units, and for $\lambda = 800$ nm light, these quantities can be written as:

$$\frac{A_{osc}}{\lambda} = 0.11\sqrt{I_{18} \quad [\mathrm{W/cm^2}]} \tag{2.5}$$

$$\frac{v_{osc}}{c} = 0.68\sqrt{I_{18} \quad [\mathrm{W/cm^2}]}. \tag{2.6}$$

Here the intensity I_{18} is taken in units of 10^{18} W/cm^2. The so-called ponderomotive potential, or quiver energy, can be straightforwardly obtained from the quiver velocity via the classical kinetic energy formula:

$$\Phi_{\mathrm{pond}} = \frac{1}{4}\frac{e^2\,E_{x0}^2}{m\,\omega^2}. \tag{2.7}$$

Evidently, as I_{18} approaches 1, the oscillation velocity becomes comparable with the speed of light, and the $\mathbf{v} \times \mathbf{B}$ term in the Lorentz force equation can no longer be neglected. Moreover, in this limit, the classical picture becomes inadequate to describe the electron motion in the laser field, and a relativistic treatment is necessary.

2.1.2 The relativistic intensity threshold

At sufficiently high laser intensities, it is customary to describe the laser field strength by the dimensionless vector potential a_0, defined as the ratio of the electron quiver momentum p_{osc}, to $m_e c$:

$$a_0 = \frac{p_{osc}}{m_e c} = \frac{eE}{m_e\,c\,\omega}. \tag{2.8}$$

The intensity in Eq. 2.1 can then be expressed in terms of a_0:

$$I = \frac{m_e^2\, c\, \omega^2}{2\, \mu_0\, e^2}\, a_0^2 \tag{2.9}$$

$$I\, \lambda^2 = \frac{2\, \pi^2\, m_e^2\, c^3}{\mu_0\, e^2}\, a_0^2, \tag{2.10}$$

or in practical units:

$$I\, \lambda^2 = 1.37 \times 10^{18}\, a_0^2 \quad [\mathrm{W/cm^2 \mu m^2}]. \tag{2.11}$$

At the threshold $a_0 = 1$, the quiver momentum becomes relativistic ($p_{osc} = m_e\, c$). For Ti:sapphire lasers ($\lambda = 800$ nm), this corresponds to an intensity of $\simeq 2.16 \times 10^{18}$ W/cm^2. Using the relativistic momentum expression, a_0 in Eq. 2.8 can be re-written as $\gamma\, v_{osc}/c$. Here, γ is the Lorentz factor $\gamma = (1 - \frac{v_{osc}^2}{c^2})^{-1/2}$ which can be expressed – for linearly polarized light – as follows:

$$\gamma = \sqrt{1 + \frac{a_0^2}{2}}. \tag{2.12}$$

When the laser intensity becomes relativistic, it can be shown [19] that the electron posses an average drift momentum, in addition to the transverse quiver component. In the laboratory frame, the drift momentum and velocity are given by $\overline{p_\parallel} = \frac{a_0^2}{4}$ and $\overline{v_\parallel} = \frac{a_0^2}{a_0^2 + 4} c$, respectively.

2.2 Laser interaction with a plasma

2.2.1 Electron plasma frequency and critical density

Using the two-fluid formalism, it can be shown [20] that a plasma supports collective charge density fluctuations resulting in a high frequency electron plasma wave, and lower frequency ion acoustic wave. In the absence of strong magnetic fields, the electron plasma wave frequency is given by :

$$\begin{aligned} \omega_{pe} &= \sqrt{\frac{e^2 n_e}{\epsilon_0 m_e}} \\ &= 5.64 \times 10^4 \sqrt{n_e}, \end{aligned} \tag{2.13}$$

where n_e is the electron density expressed in units of cm^{-3}.

For a plane electromagnetic wave $\mathbf{E} = \mathrm{Re}\{\mathrm{E_{x0}e^{i\omega_L t}}\}$ incident on a plasma slab with an electron density $n_e = n_e(z)$, the plasma dielectric function $\epsilon(z)$ can be derived from the Lorentz and Maxwell equations [19]. Neglecting the collisional damping term, it is given by:

$$\epsilon(z) = 1 - \frac{\omega_{pe}^2(z)}{\omega_L^2} \tag{2.14}$$

It is evident that when the electron plasma frequency becomes larger than the laser frequency ($\omega_{pe} > \omega_L$) the plasma index of refraction ($\widetilde{n} = \sqrt{\epsilon}$) becomes imaginary and the electromagnetic field becomes evanescent and is reflected back toward lower density region. The so-called critical density – the electron density at the surface where $\omega_{pe} = \omega_L$ – is obtained from Eqs. 2.13:

$$\begin{aligned} n_{cr} &= \frac{m_e\, \epsilon_0\, \omega_L^2}{e^2} \\ &= 1.1 \times 10^{21}\, \lambda_L^{-2} \quad [\mathrm{cm}^{-3}]. \end{aligned} \tag{2.15}$$

Here, the laser wavelength λ_L is in units of μm. As previously stated, at intensities higher than 10^{18} W/cm^2, the electron quiver velocity becomes relativistic and the electron mass is modified by the Lorentz factor γ (Eq. 2.12):

$$m_e = \gamma\, m_{e0} = \sqrt{1 + \frac{a_0^2}{2}}\; m_{e0}. \tag{2.16}$$

Consequently, this will change the effective critical density in Eq. 2.15 to:

$$n_{cr} = \frac{\gamma\, m_{e0}\, \epsilon_0\, \omega_L^2}{e^2} = \gamma\, n_{cr0} \tag{2.17}$$

The electromagnetic wave cannot propagate beyond the critical surface, however, the laser can still indirectly deposit energy in the overdense region via hot electrons. The mechanisms by which these electrons are heated depend on the laser parameters, but also on the gradient of electron density profile, or the so-called plasma scale-length L defined by:

$$L = n(z) \left[\frac{d\, n(z)}{dz}\right]^{-1}, \tag{2.18}$$

evaluated at $n(z) = n_{cr}$.

2.3 Ultra-intense laser heating mechanisms

The energy absorption of an intense femtosecond pulse by a solid-density plasma is governed by both collisional and collisionless processes. Collisional processes, generally referred to by inverse-bremsstrahlung heating, involve discreet particle interactions (electron-ion collisions). However, when the laser pulse intensity is higher than 10^{16} W/cm^2, collisionless mechanisms such as skin-layer heating, resonance absorption, Brunel (vacuum) heating and $\boldsymbol{j} \times \boldsymbol{B}$ heating become important. The various interaction parameters, such as the pulse duration, plasma scale-length and the target composition to name a few, can favor one or more of these mechanisms to be dominant. In the following section we shall briefly discuss some of the processes that could be relevant to the laser-plasma interaction in the λ^3 regime.

2.3.1 Inverse-bremsstrahlung heating

Inverse-bremsstrahlung heating refers to the absorption mechanism involving the damping of the laser pulse due to electron-ion collisions. Therefore, the fundamental parameter describing this interaction is the electron-ion collision frequency ν_{ei}.

Kruer [20] shows a straight-forward derivation of ν_{ei} by considering the small-angle scattering of an electron in the Coulombic field of a nucleus, and calculating the time over which the root-mean-square velocity change is comparable to the initial velocity:

$$\begin{aligned} \nu_{ei} &= \frac{4\,(2\pi)^{1/2}}{3}\,\frac{n_e\,Z\,e^4}{m_e^2\,v_{th}^3}\,\ln\Lambda \\ &\simeq 2.91\times10^{-6}\,Z\,n_e\,T_e^{-3/2}\,\ln\Lambda \quad [\mathrm{s}^{-1}]. \end{aligned} \tag{2.19}$$

Here Z is the number of free electrons per atom, n_e the enelctron density in cm^{-3}, T_e the electron temperature in eV and $\ln\Lambda$ the Coulomb logarithm. The mean free path between collisions λ_{ei}, can then obtained by dividing the electron velocity by the collision rate:

$$\begin{aligned} \lambda_{ei} &= \frac{v_{th}}{\nu_{ei}} \\ &\simeq 1.4\times10^{23}\,\frac{T_e^2}{Z\,n_e\,\ln\Lambda} \quad [\mu\mathrm{m}]. \end{aligned} \tag{2.20}$$

Starting from Maxwell equations, the inverse-bremsstrahlung energy absorption coefficient can be calculated [21]:

$$\kappa_{ib} = 7.8\times10^{-9}\,\frac{Z\,n_e^2}{\omega_L^2 T_e^{3/2}}\,\ln\Lambda\,\frac{4\pi^2}{\left(1-\omega_{pe}^2/\omega_L^2\right)^{1/2}}, \tag{2.21}$$

where ω_L and ω_{pe} are respectively the laser and plasma frequencies given in units of s^{-1}. Note that, from the above equation, κ_{ib} becomes increasingly larger for denser plasmas and lower electron temperatures. Thus, for laser intensities greater than $\sim 10^{15}$ $\mathrm{W/cm}^2$, the electrons become too energetic to effectively couple their energy to the plasma ions, and the inverse-bremsstrahlung mechanism ceases to be important. With relevance to experiments in the λ^3 regime, the

inverse-bremsstrahlung mechanism has little or no contribution to the heating by the ultra-short pulse at relativistic intensities. However, it is important for the pre-heating of the target by the nanosecond pedestal that could alter the electron density profile and strongly influence the main interaction.

2.3.2 Resonance absorption

Resonance absorption is significant for intensities $I\lambda^2 \geq 10^{15}$ W/cm^2 when the plasma scale length is long compared to the laser wavelength.

Consider a p-polarized light wave, incident at angle θ on an inhomogeneous plasma slab ($n_e = n_e(z)$) with a gradient ∇n_e normal to the plasma surface. The wave will have a non-zero component of the electric field that is parallel to the density gradient ($\mathbf{E_z} \parallel \nabla n_e$), and the magnetic field will be perpendicular to the incidence plane ($\mathbf{B} = \mathbf{B_y} \perp \nabla n_e, \mathbf{k_{xz}}$). It can be shown by solving the wave equation that the wave will reflect at the surface $n_e(z) = n_{cr} \cos^2\theta$, where n_{cr} is the usual critical density defined in Eq. 2.15. Also, from the Poisson equation ($\nabla \cdot (\epsilon\, \mathbf{E}) = 0$), it follows that:

$$\nabla \cdot \mathbf{E} = -\frac{1}{\epsilon}\frac{\partial \epsilon}{\partial z}\mathbf{E_z} \tag{2.22}$$

Here $\epsilon = \epsilon(z) = 1 - e^2\, n_e(z)/m_e\, \epsilon_0\, \omega_L^2$. At the critical density, $\epsilon = 0$ and the E_z becomes large. Thus, although the wave is reflected below the critical density, the electric field tunnels to the critical surface and drives a resonant electrostatic wave that grows with the laser pulse.

Earlier analytical treatments of resonance absorption by Denisov [22] and Ginzburg [23] have shown that for a long scale length plasma ($2\pi L/\lambda_0 \gg 1$), the absorption coefficient η_{ra} has a self-similar dependence on the parameter $\xi = (2\pi L/\lambda_0)^{1/3} \sin\theta$ given by:

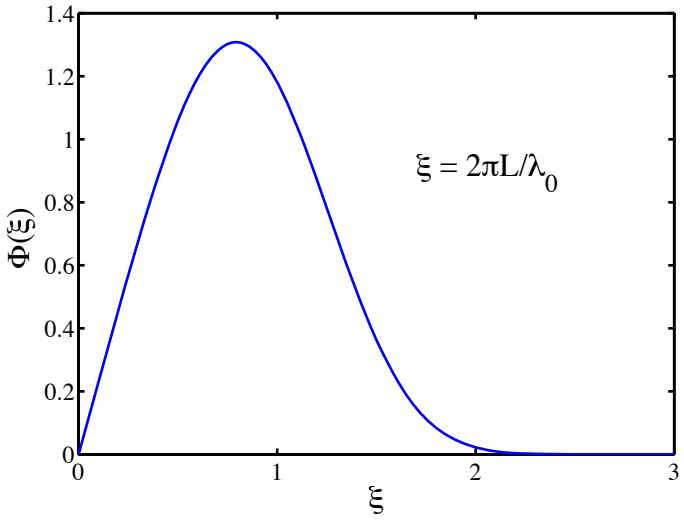

Figure 2.1: The Denisov function $\Phi(\xi)$

$$\eta_{ra} = \frac{1}{2}\Phi^2(\xi), \tag{2.23}$$

where $\Phi(\xi)$ is the Denisov function:

$$\Phi(\xi) \simeq 2.3\,\xi\,\exp\left(-2\,\xi^3/3\right). \tag{2.24}$$

From the behavior of $\Phi(\xi)$ (Fig. 2.1) it becomes evident that, for a given scale length L, there exists an incidence angle θ_{opt} where the resonance absorption coefficient is maximum. θ_{opt} can readily be obtained by equating $d\Phi/d\xi = 0$, and solving for θ:

$$\theta_{opt} = \arcsin\left[\frac{(1/2)}{2\pi L/\lambda_0}\right]^{1/3}. \tag{2.25}$$

Forslund *et al.* [24] showed that the temperature scaling of the resonantly-heated electrons follows:

$$T_h^{ra} \approx 14\left(\frac{I}{10^{16}}\lambda_0^2\right)^{1/3} T_{cold}^{1/3}, \tag{2.26}$$

where T_h^{ra}, T_{cold} are the hot and thermal electron temperatures, respectively, given

in keV. I is in W/cm^2 and λ_0 the laser wavelength in μm.

When the scale length L becomes smaller than the quiver amplitude A_{osc} (Eq. 2.3) at a given laser intensity, resonant plasma waves can no longer be sustained around the critical density and the resonance absorption contribution drops considerably giving way to the vacuum heating mechanism.

2.3.3 Vacuum heating

This mechanism is also referred to as the Brunel effect [25]. In its standard picture it involves a p-polarized laser beam obliquely incident on a steep-density-profile plasma. As in the resonance absorption model, the plasma electrons are driven by the **E** field in an oscillatory motion across the interface with an oscillation amplitude $A_{osc} = eE_L/m_e\omega_L^2$. However if the scale-length L is smaller than the oscillation amplitude $L < A_{osc}$, the plasma cannot support the formation of resonant waves as in the resonance absorption case, and the electrons are accelerated away from the interface into the vacuum. As the polarity of the laser field inverts, the electrons are slowed down then accelerated backwards toward the plasma. While the laser is reflected at the surface with density $n_{cr}\cos^2\theta$, the electrons penetrate the overdense plasma with a considerable net energy.

For laser intensity of the order of 10^{18} W/cm^2, the electron quiver amplitude from Eq. 2.5 is $\sim 0.1\lambda$. Thus, vacuum heating would be most significant in plasmas with scale length range $L/\lambda \lesssim 0.1$.

Bonnaud *et al.* [26] have demonstrated using a 1-dimensional code that, in the case of an infinitely steep gradient, the hot electron temperature scales with the square of the quiver velocity, or simply the laser intensity. In practical units this scaling can be written:

$$T_h^B \simeq 3.6 \times \frac{I}{10^{16}}\lambda_\mu^2 \quad [\text{keV}]. \tag{2.27}$$

However, more realistic simulations [27, 28] showed that the vacuum heating mechanism saturates at higher intensities ($I\lambda^2 > 10^{17}$ W/cm^2) due to the deflection of electrons by the $\mathbf{v} \times \mathbf{B}$ component of the Lorentz force. An analytical model [29] that takes the saturation behavior into account yields a weaker scaling:

$$T_h^B = 8 \left(\frac{I}{10^{16}} \lambda^2 \right)^{1/3} \quad \text{[keV]}. \tag{2.28}$$

2.3.4 $\boldsymbol{j} \times \boldsymbol{B}$ heating

The $\boldsymbol{j} \times \boldsymbol{B}$ mechanism was first suggested by Kruer and Estabrook [30] to describe the absorption at very high intensities due to the oscillating component of the ponderomotive force exerted on the plasma electrons.

To understand the physical picture behind this mechanism, it is useful to introduce the ponderomotive force. Consider a linearly polarized plane wave $\mathbf{E} = \mathbf{E_x}(z) \sin(\omega t)$, incident on a homogeneous plasma ($n_e(z) = n_e$). The force equation – ignoring the electron pressure – can then be written:

$$n_e \frac{\partial \mathbf{v}}{\partial t} + n_e \mathbf{v} \frac{\partial \mathbf{v}}{\partial x} = -\frac{n_e e}{m_e} (\mathbf{E} + \mathbf{v} \times \mathbf{B}). \tag{2.29}$$

Neglecting second-order terms in the above equation, and solving for $\mathbf{v}$:

$$\begin{aligned} \frac{\partial \mathbf{v}}{\partial t} &= -\frac{e}{m_e} \mathbf{E_x}(z) \sin(\omega t) \\ v &= \frac{eE_x}{m_e \omega} \cos(\omega t); \end{aligned}$$

Substituting back into Eq. 2.29 we obtain:

$$f_{nl} = -\frac{m_e}{4} \frac{\partial v^2}{\partial z} [1 - \cos(2\omega t)]. \tag{2.30}$$

Averaging over many cycles, the first term in Eq. 2.30 yields the usual ponderomotive

force. The second term however, oscillating with a frequency 2ω, corresponds to a field E_d given by:

$$E_d = -\frac{m_e}{4e}\,\frac{\partial v^2}{\partial x}\,\cos(2\omega t). \tag{2.31}$$

This field directly accelerates electrons across the interface, and significantly contributes to the heating at relativistic laser intensities ($I\lambda^2 \geq 10^{18}$ W/cm^2).

Wilks *et al.* [31] have demonstrated using 2-dimensional PIC simulations that the temperature of electrons heated by the $\mathbf{j} \times \mathbf{B}$ mechanism scale according to the following formula:

$$T_h^W = m_e\,c^2\left[\left(1+\frac{p_{osc}^2}{m_e^2\,c^2}\right)^{1/2}-1\right] \tag{2.32}$$

$$\simeq 511\left[\left(1+0.73\,\frac{I}{10^{18}}\lambda^2\right)^{1/2}-1\right] \quad [\text{keV}]. \tag{2.33}$$

2.4 X-ray generation by energetic electrons

From the previous section we have seen that an intense laser can heat electrons to temperatures as high as few hundred keV. At these energies, the mean free path between electron-ion collisions (Eq. 2.20) can be much larger than the laser spot size ($\sim$ 1 μm in the λ^3 regime). Thus, the electrons heated in the plasma are launched deep into the cold target. Eventually, they will scatter off the cold target atoms producing bremsstrahlung and characteristic line radiation. In this section we will briefly review these two processes and comment on the method of electron temperature extraction from the bremsstrahlung spectrum.

2.4.1 Bremsstrahlung continuum generation

In the classical picture, bremsstrahlung radiation is emitted when an electron is scattered by the Coulombic field of a nucleus of charge Ze (see Fig. 2.2). The

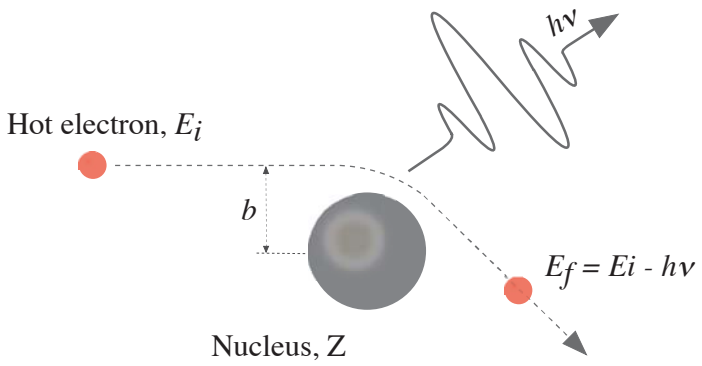

Figure 2.2: Bremsstrahlung radiation generated when an electron (with energy E_i) scatters off the Coulombic field of a nucleus of charge Z. The impact parameter b describes the strength of the interaction.

radiated power is related to the initial energy of the electron E, the nucleus charge Z, and the impact parameter b which can be thought of as the distance separating the nucleus and the electron trajectory had there been no interaction between them. Due to the wide range of values that the impact parameter can have, the bremsstrahlung spectrum is characterized by a broad continuum that extends, theoretically, up to the scattering electron initial energy $h\nu_{\max} = E$

For non-relativistic electron energies, the bremsstrahlung cross-section per unit frequency interval $d\omega$ can be derived quantum mechanically [32] by considering the energy conservation and integrating over momentum transfer.

$$\frac{d\sigma}{d\omega} \simeq \frac{16}{3}\frac{Z^2e^2}{c}\left(\frac{e^2}{m_oc^2}\right)^2\frac{1}{\beta^2}\ln\left[\frac{Q_{max}}{Q_{min}}\right]. \tag{2.34}$$

Here Q_{max} and Q_{min} are the maximum and minimum momentum transfer given by:

$$\frac{Q_{\max}}{Q_{\min}} = \frac{p+p'}{p-p'} = \frac{(\sqrt{E}+\sqrt{E-h\,\nu})^2}{h\,\nu}. \tag{2.35}$$

Both experimental results and simulations have shown that the hot electrons generated from the interaction of an intense laser with a solid density plasma have a Maxwellian-like energy distribution with a temperature T_h:

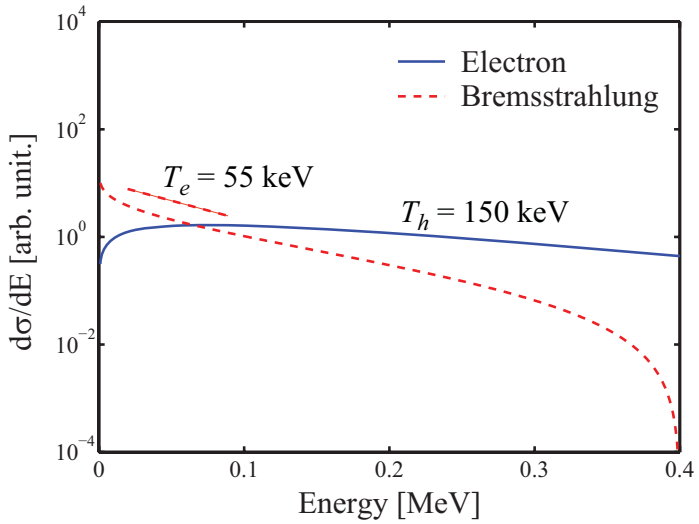

Figure 2.3: Maxwellian electron distribution with temperature $T_h = 150$ keV and maximum electron energy $E_{\max} = 500$ keV (solid) and simulated bremsstrahlung spectrum (dashed), based on Eq. 2.34, for an optically thin converter. The slope of the bremsstrahlung, measured between 10 and 100 keV corresponds to an effective temperature $T_e = 55$ keV.

$$f_E(E) = \frac{2}{\sqrt{\pi}}\, T_h^{-3/2}\, \sqrt{E}\, \exp\left[-\frac{E}{KT}\right]. \tag{2.36}$$

The corresponding bremsstrahlung spectrum can be predicted by convolving the electron energy distribution with the radiation cross-section in Eq. 2.34. As an example, Fig. 2.3 shows a normalized spectrum produced by a Maxwellian electron distribution with temperature $T_h = 150$ keV, and endpoint $E_{\max} = 500$ keV, assuming an optically thin converter (no x-ray re-absorption in the target). At intermediate photon energies (10 to 200 keV), the bremsstrahlung spectrum can be fit to a Maxwellian distribution with an effective temperature $T_e = 55$ keV.

Since it is more straightforward to measure x-ray spectra rather than electron energy distributions, several studies infer the hot electron temperature from the bremsstrahlung spectrum by fitting the photon energy distribution to a Maxwellian. The drawback is, however, that the obtained bremsstrahlung temperature underestimates the actual electron temperature. Moreover, the x-ray reabsorption in the target could substantially alter the spectrum, especially in the vicinity

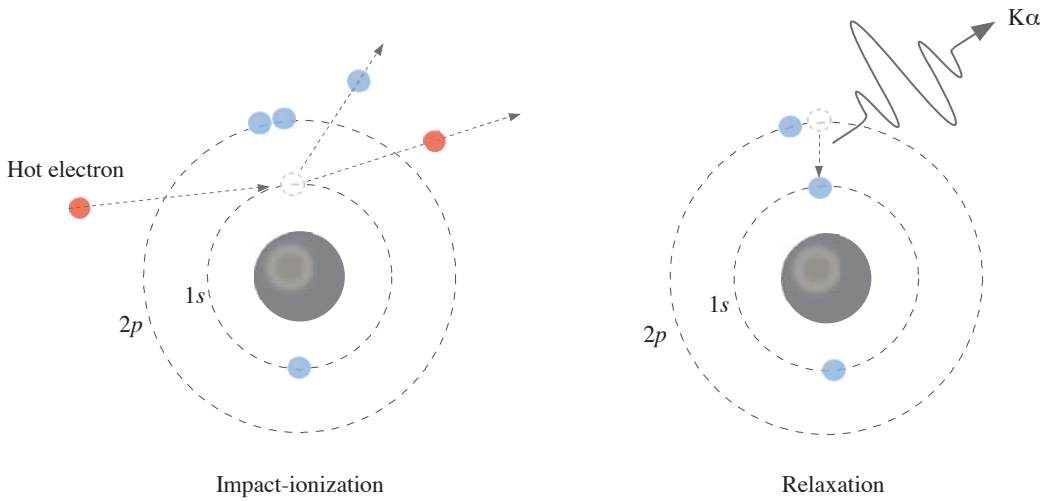

Figure 2.4: Kα line emission process.

of an absorption edge. For these reasons, care must be taken when extracting electron temperatures from bremsstrahlung spectra, and ideally one should resort to numerical simulations (Monte Carlo) for more reliable figures.

By virtue of their broad spectra, bremsstrahlung sources are useful for applications such as x-ray absorption spectroscopy [33].

2.4.2 Characteristic line emission

If the incident electron has an initial energy E greater than the K-shell binding energy E_K, it could ionize the atom by knocking off an electron from its lowest energy level ($1s$). Subsequently, the excited ion will relax through an electronic transition from a higher energy level down to the vacant $1s$ level (See Fig. 2.4). This relaxation is accompanied by the emission of either a photon or an Auger electron with a characteristic energy equal to the difference between the transitioning electron initial and final states. For radiative transitions occurring between the $2p \longrightarrow 1s$ states, the emitted photons are labelled Kα. The K-line emission for elements used throughout this dissertation are listed in table 2.4.2.

For electron energies up to 10 times the binding energy of the K-shell, the number of Kα photons produced by an electron of energy E can be expressed by the

Element	Z	Binding energy	Kα_1	Kα_2	Kβ_1
Al	13	1,559	1,486.70	1,486.27	1,557.45
Si	14	1,839	1,739.98	1,739.38	1,835.94
Ni	28	8,333	7,478.15	7,460.89	8,264.66
Cu	29	8,979	8,047.78	8,027.83	8,905.29
Ge	32	11,103	9,886.42	9,855.32	10,982.1
Mo	42	20,000	17,479.3	17,374.3	19,608.3
Ag	47	25,514	22,162.9	21,990.3	24,942.4
Au	79	80,725	68,803.7	66,989.5	77,984.0

Table 2.1: K-shell binding and emission line energies (in eV) for various target materials [34].

following empirical expresion [35, 36]:

$$N_{K\alpha}(E) = \mathcal{N}(E - E_K)^{1.63}, \tag{2.37}$$

where $\mathcal{N}$ is an empirically determined function of the target material (Z). Given a hot electron distribution $f_h(E)$, the total number of Kα photons emitted from a laser-produced plasma can be calculated as follows:

$$N_{K\alpha} = \int f_h(E)\, N_{K\alpha}(E)\, \eta_\alpha(E)\, dE. \tag{2.38}$$

Here η_α is the fraction of photons that escape the target. Evidently, as the photon energy increases, both the depth of ionization event (related to λ_{ei} in Eq. 2.20) and the reabsorption fraction increases, and therefore η_α decreases.

CHAPTER III

X-RAY SOURCE DRIVEN BY A RELATIVISTIC-INTENSITY λ^3 LASER

3.1 Introduction

X-ray bursts produced by sub-100 fs laser pulses can have a temporal duration of few hundred femtoseconds [37, 38]. Additionally, by using proper crystals and x-ray optics, one can filter for characteristic line emission to obtain an ultrafast quasi-monochromatic source. This makes laser-produced x-rays a potentially attractive probe for dynamic diffraction studies ranging from solid state physics , [39, 40, 41] to chemistry and biology [42, 37, 43].

Although relativistic intensities are not necessary for the efficient production of Kα, there has been interest in characterizing the x-ray source for a laser intensity higher than 10^{18} W/cm^2 [44, 45, 46]. This chapter discusses the properties of the hard x-ray source driven by a relativistic-intensity laser in the λ^3 regime. In earlier work, Hou *et al.* [12] studied the source spectroscopy and measured the conversion efficiency scaling with the laser pulse energy and duration. More recently, we have measured the source size for various target materials using the knife-edge technique. We have also investigated the spatial coherence properties of x rays generated in a Si plasma and inferred the source size from the straight-edge diffraction pattern.

3.2 The λ^3 laser

The relativistic intensity experiments discussed throughout this dissertation were carried out on the λ^3 laser facility at CUOS, University of Michigan. The 500 Hz Ti:sapphire system is built in the standard chirped-pulse amplification (CPA) configuration [1] and produces $\sim$ 30 fs pulses with up to 1.5 mJ energy. The last amplification stage, which was originally built as a multi-pass, has been recently upgraded to a regenerative amplifier. However, all x-ray experiments discussed in the present chapter were performed with the pre-upgrade version.

Figure 3.1 shows a block-diagram of the pre-upgrade λ^3 CPA system. It is seeded by a Ti:sapphire Kerr-lens mode-locked oscillator (Femtolaser GmbH) producing nanojoule-level, sub-12 fs pulses at a repetition rate of 72 MHz. These pulses are next selected at the rate of 500 Hz using a Pockels cell (Lasermetrics Inc.). The oscillator is protected against amplified back-reflected pulses by a Faraday isolator (Electro-optic Tech, Inc.). In order to achieve a high intensity contrast ratio at the output of the system, it is necessary to improve the contrast of the seed pulses injected in the power amplification stages. To this end, the oscillator pulses are pre-amplified to the microjoule level using a 6-pass stage and focused on a pulse cleaner based on a saturable absorber (Hoya, IR85) [47]. Subsequently, the pulses are positively chirped to $\sim$ 30 ps in a diffraction grating stretcher and injected into the power amplification stages.

The pre-upgrade system incorporates two amplifier stages. The first is a six-pass stage with a water-cooled Ti:sapphire crystal pumped by a frequency-doubled Nd:YLF laser (Evolution X). The second stage is a three-pass amplifier that outputs up to 7.5 mJ of infra-red from 22 mJ of pump energy (Evolution 30). The Ti:sapphire crystal in this last stage is cryogenically cooled (130 K) inside a vacuum compartment to reduce the effects of thermal lensing. At the output of the amplifiers is installed another Pockels cell set-up that serves two functions: it

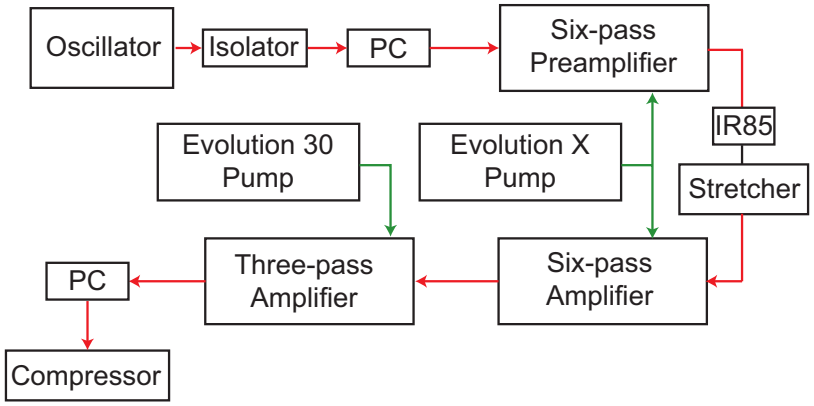

Figure 3.1: Block diagram of the pre-upgrade λ^3 laser system. PC stands for Pockels cell.

suppresses the leakage prepulses and protects the system from back-reflected pulses during solid-target experiments. Finally, the pulses are compressed to $\sim$ 32 fs in a diffraction-grating compressor. To reduce the accumulated nonlinearities due to propagation in air, the beam is expanded to $\sim$ 47 mm diameter using an all-reflective telescope. At maximum pump current, the system can produce up to 2.5 mJ pulses on target, in a 35 nm bandwidth centered at 790 nm.

3.3 Experimental set-up and detectors

3.3.1 Experimental set-up

All experiments described in this chapter are conducted in a vacuum chamber at or below 10^{-3} Torr pressure. The laser pulses, with up to 1.5 mJ of energy in 32 fs, are focused on a thick disk target using a high numerical aperture ($\sim f/1$), gold-coated paraboloidal mirror. Intensities as high as $\sim 2.5 \times 10^{18}$ W/cm^2 are obtained by using a computer-controlled deformable mirror (Xinetics Inc.) that corrects for the abberations induced by the 60° off-axis focusing optic, in order to minimize the focal spot diameter [48]. This optimization procedure is routinely done before target alignment, and consists of imaging the laser focal spot onto a second harmonic generation crystal (BBO) using a 60×, 0.8 N.A. microscope objective. The intensity of the up-converted blue light is inversely proportional to the spot area on

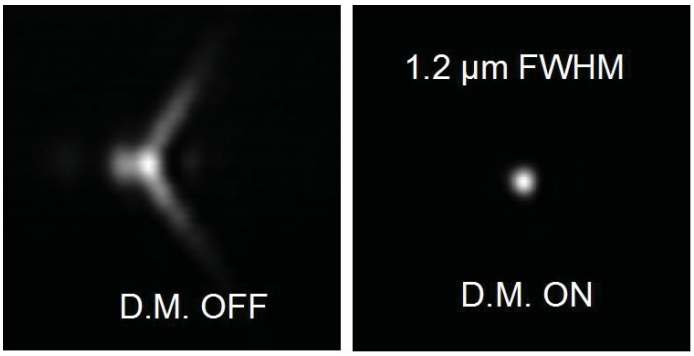

Figure 3.2: Focal spot before and after the deformable mirror optimization.

the BBO crystal. Thus, the deformable mirror actuators are optimized by means of a genetic algorithm that maximizes the second harmonic generated as measured by a photodiode. To avoid damaging the microscope objective the pulse energy is attenuated by a factor of ~ 10 using a half-waveplate and polarizer combination, and by an additional 3-4 orders of magnitude using neutral density filters.

Given the short Raleigh range associated with the micron-sized focal diameter ($2\,z_r \approx 12\ \mu$m for 1.5 μm FWHM spot size, at $\lambda_0 = 800$ nm), the targets are mounted such that their surface flatness is about $\pm 2\ \mu$m for most cases. Additionally, they are rotated and translated by a computer controlled motion stage to ensure that each laser shot interacts with a fresh target area. A 2 μm-thick nitrocellulose pellicle is usually placed between the plasma and paraboloidal mirror, to protect the latter from debris. X-ray detectors – such as photographic film and photodiodes – were mostly used outside of vacuum, and therefore, Be windows that are transparent to x-rays above 4 keV were used.

3.3.2 DEF x-ray film

Kodak Direct Exposure Film (DEF) is a high-sensitivity, low-fog film suitable for the $1 - 10$ keV spectral window [49]. We have used it to infer the x-ray source size from the shadowgraph of a knife-edge as described in section 3.5, as well as for small animal imaging experiments. The nonlinearity in the film response was corrected for,

by following the sensitometer/densitometer calibration method. In this procedure, a sensitometer (from X-rite Inc.) exposes a film sample with preset graduated density steps in the visible spectral region. After developing the film following the standard method, the optical density at each of the exposed steps is measured (typically with a scanner) to obtain the calibration curve expressing the irradiance as a function of optical density (or gray-scale values). Since the DEF spatial resolution is of the order of ~ 75 μm (measured at the titanium Kα wavelength [50]), we made sure that the magnification factor of the projection imaging was sufficiently large to resolve micron-size features.

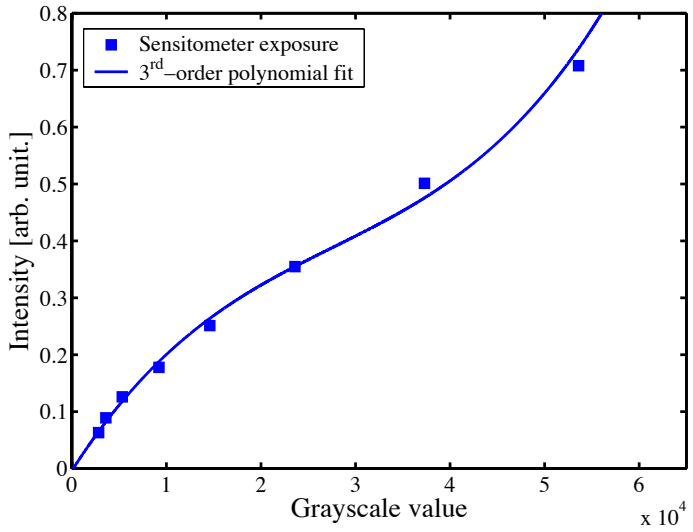

Figure 3.3: Calibration curve for the DEF as obtained with the sensitometer-densitometer procedure (squares) along with its fit into a 3$^{\text{rd}}$-order polynomial.

3.4 Background: x-ray source characterization in the λ^3 regime

3.4.1 X-ray spectra

The physics of x-ray generation from a laser-produced-plasma source is briefly discussed in section 2.4. In summary, the laser-heated electrons scatter off the target atoms to produce characteristic line emission and continuous bremsstrahlung

Target (Z)	η_{Total} $\times 10^{-5}$	$\eta_{\text{K}\alpha}$ $\times 10^{-5}$	T_e keV	Source size (FWHM) vert. $\times$ horiz. μm^2
Cu(29)	4.5	1.7	18.6	$(13.7 \pm 1.6) \times (15.1 \pm 1.2)$
Ge(32)	4.6	1.8	17.0	
Mo(42)	21.2	4.1	19.9	$(12.2 \pm 1.7) \times (13.3 \pm 3.1)$
Ag(47)	20.8	3.1	34.0	$(7.7 \pm 1.0) \times (10.8 \pm 1.3)$
Sn(50)	9.4	1.3	47.9	$(13.6 \pm 1.7) \times (17.6 \pm 1.9)$
Au(79)	82.0	~ 0	47.5	

Table 3.1: X-ray conversion efficiencies (total and Kα), electron temperature and source spot size for various target materials measured at $\sim 10^{18}$ W/cm^2. From [12, 15].

radiation. Hou *et al.* [12, 15] have characterized the x-ray spectra generated from various target materials (Cu, Ge, Mo, Ag, Sn and Au) in the relativistic λ^3 regime. The electron characteristic temperature and conversion efficiencies into the Kα line and total x-rays were obtained from the spectra measured with a cadmium-zinc-telluride detector (Amptek Inc., XR-100T). At the intensity of $\sim 10^{18}$ W/cm^2, the characteristic electron temperature T_e – defined as the slope of the bremsstrahlung energy spectral density in the 20 to 100 keV range – varied between 17 keV for Ge (Z=32) to about 48 keV for Sn (Z=50) and Au (Z=79). The Kα conversion efficiency varied between $\sim 1 - 4 \times 10^{-5}$ for all targets except for the case of Au, where the K-lines were not observed at all. This was attributed to the fact that the electron temperature in the case of Au is lower than the K-shell binding energy ($\mathcal{E}_K = 80.7$ keV [51]).

The x-ray conversion efficiencies reported in table 3.4.1 assume an isotropic emission into the half space. A detailed analysis of the spatial distribution, for both p- and s-polarization, is reported in [52].

3.4.2 Scaling of x-ray conversion efficiency

The x-ray conversion efficiency scaling with laser intensity (or the $I\lambda^2$ parameter) has been extensively studied [53, 54, 45, 35, 55], using laser facilities providing

greater than 100 mJ pulses with duration ranging from a picosecond to few tens of femtoseconds. In order to extend the understanding of x-ray generation to the λ^3 regime, Hou and coworkers [12] investigated the x-ray conversion efficiency scaling with the pulse energy and duration for a Mo target.

The findings in [12] are summarized in Fig. 3.4. For the fixed pulse duration of 22 fs, the Kα conversion efficiency was found to have a power-law dependence on the pulse energy:

$$\eta \propto E^{\gamma}, \tag{3.1}$$

with $\gamma_{\alpha} \sim 1.6$. Also, the characteristic electron temperature was found to follow a similar scaling with $\gamma_{Te} \simeq 0.5$.

The Kα conversion efficiency scaling with pulse duration was also investigated [12] for a fixed pulse energy ($\sim$ 1 mJ). Between 22 and 560 fs, the conversion efficiency into the Kα was found to follow a single exponential decay model:

$$\eta(\tau) \propto \exp\left(-\tau/\beta_{\alpha}\right) \tag{3.2}$$

with $\beta_{\alpha} = 650$ fs. This indicates a weak dependence of the x-ray yield on the driving pulse duration, in the sub-picosecond range. In fact, for a factor of 25 increase in pulse duration (decrease in intensity), the conversion efficiency only decreased by a factor of ~ 2.

This finding implies that sub-100 fs pulses are not necessary to drive high-efficiency x-ray sources. In Chapter V we discuss a novel approach to high-brightness x-ray sources driven by ultrafast fiber lasers that have recently demonstrated millijoule, $\sim$ 300 fs pulses [56, 57].

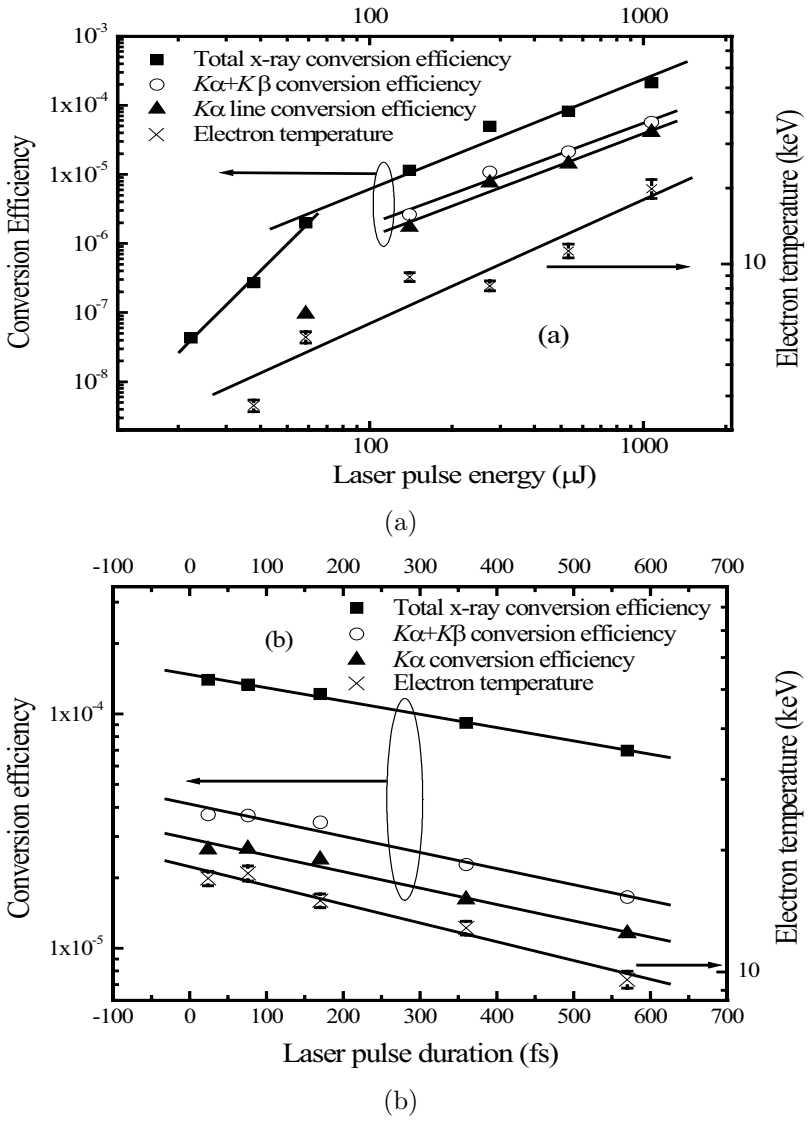

Figure 3.4: The Mo x-ray conversion efficiency and characteristic electron temperature scaling with the laser pulse energy (a) and duration (b) (from [12]).

3.5 X-ray source size measurements

By definition, the λ^3 regime involves focusing the laser pulses down to a focal spot of a similar dimension to the laser wavelength. Therefore, one expects that the x-ray source produced in this regime would have a comparably small size (a few micrometers). Such a property is advantageous for x-ray imaging applications since the resolution of a projection imaging system increases with a decreasing source size.

In this section we experimentally investigate the x-ray source size at near-relativistic intensities ($\sim 10^{18}$ W/cm^2) using the knife-edge technique.

3.5.1 The knife-edge technique

In the ideal case, the point spread function of a point source is nothing but the *delta* function $\delta(X, Y)$ in the image plane. For a real x-ray source with an intensity distribution $f(x, y)$ in the source plane, the point spread function can be calculated by convolving, in the image plane, the intensity distribution of the source with the point spread function, which yields a function identical to the source intensity distribution (within a magnification factor determined by the geometry). Thus, if the point spread function of a projection system could be experimentally recorded, the source intensity distribution (and hence its size) could be inferred. In practice, however, it is difficult to directly measure an ideal point- (or even line-) spread function. An alternate method consists of measuring the spread function of a straight edge by recording, on an x-ray film, the shadowgraph of the edge magnified by factor M. After calibrating the opacity of the film for linearity in the visible range using a standard sensitometer/densitometer procedure, the edge-spread function is fitted to the Fermi function:

$$\mathcal{F}(X) = A + \frac{B}{1 + \exp\left[(X - \mu)/\sigma\right]} \tag{3.3}$$

Noting that the *delta* function (or point object) is in fact the first derivative of the idealized edge function (or step function), then the line spread function can be calculated, by virtue of linearity, differentiating the edge spread function in Eq. 3.3. This yields a Gaussian-like function, whose full width at half-maximum is equal to that of the source multiplied by the magnification factor M. It must be noted here that the preceding analysis is valid only in the case of incoherent illumination, and therefore the edge should be placed close enough to the source so that spatial

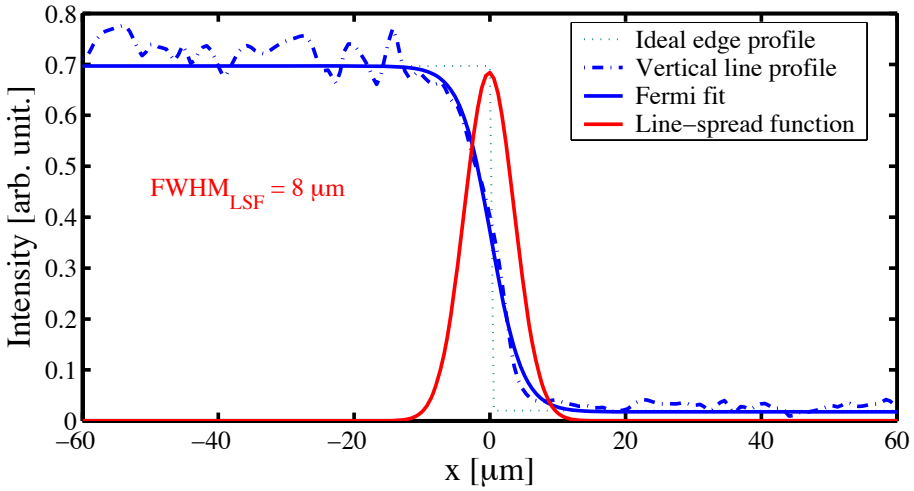

Figure 3.5: The vertical line profile of a horizontal knife edge, imaged using Ag target is shown (blue dot-dash). The line spread function (red), which also corresponds to the intensity distribution at the source, is calculated by differentiating the fit of edge profile (blue solid). For comparison, the ideal edge profile casted by a point source is plotted (dotted). The laser intensity is around $1 - 2 \times 10^{18}$ W/cm^2.

coherence effects are reduced (see Eq. 3.10). Another source measurement technique relying on the spatial coherence of the x-ray source is described at length in section 3.6.

3.5.2 Measurements

The x-ray source size measurement with the knife edge technique was carried out for Cu, Mo, Ag and Sn at near-relativistic intensities ($1 - 2 \times 10^{18}$ W/cm^2). The knife edge and the DEF film were mounted along the 40° direction with respect to the normal with a magnification factor $\sim 30 - 40$. The averaged vertical line-plot (dash-dotted) of a horizontal edge imaged using x rays from a Ag target is shown in Fig. 3.5. Also shown are the Fermi fit of the edge profile (blue) and the line-spread function (red), whose full width at half-maximum corresponds to that of the vertical dimension of the source (7.7 μm). The vertical and horizontal diameters for all targets used are recorded in table 3.4.1. The FWHM in the vertical dimension ranged from 7.7 μm for Ag (Z=47) target to 13.7 μm for Cu (Z=29). The horizontal dimension was consistently larger and ranged from 10.8 μm for Mo (Z=42) to

17.6 μm for Sn (Z=50).

The above measurements show that, in the λ^3 regime, the ratio of the x-ray source size to the driving laser spot size varies between $\sim 7-12$. Comparable ratios were obtained experimentally at similar intensities albeit with an initial laser spot of ~ 10 μm and a pulse energy of ~ 1 J [58, 59]. In both regimes, the size of the x-ray source can be explained by the spreading of the hot electrons outside of the laser spot. In fact, an order of magnitude estimate of the collisional electron-ion mean free path (Eq. 2.20) for $T_e = 20$ keV, $Z = 20$ and $n_e \simeq 10^{23}$ cm^{-3} yields $\lambda_{ei} \simeq 3$ μm, which is larger than the laser spot size. For an even hotter electron temperature, as the direct measurements of electron spectra reveal (see section 4.3), λ_{ei} could easily be an order of magnitude larger than estimated here. Although these hot electrons are primarily accelerated along the laser axis into the target rather than radially across its surface, several mechanisms could contribute to the extended x-ray source area. According to one explanation, the electro-static sheath created at the plasma interface reflects a fraction of the forward propagating electrons toward the vacuum then into the target again, spreading the source footprint beyond the laser focus.

The ellipticity of the source could be attributed to the strong horizontal component of the **E** field for the p-polarized pulses, but also to the asymmetry in the laser focal spot (1.2×1.4 μm^2 for this experiment). The projection factor of the obliquely incident laser on the target surface is expected to be compensated for by viewing the source along the 40° direction, and thus it does not contribute to the observed ellipticity.

3.6 Spatial coherence properties of the x-ray source

In this section we investigate the spatial coherence properties of an incoherent x-ray source produced by a near-relativistic λ^3 laser. First, we introduce the formalism of

the mutual coherence function and use the Van Cittert-Zernike theorem to relate the transverse coherence length at a point P in space to the source radius a. Next, we will show that, for a sub-10 μm laser spot, the x-ray diffraction pattern off a straight edge could be used to infer the source size in a geometry compatible with laboratory dimensions. Experimentally, we report on the diffraction pattern measurements using x-rays produced from a Si target. At the laser intensity of 2.5×10^{17} W/cm^2, these measurements yield a source diameter of 6 μm . Finally, we will comment on the usefulness of a micron-size source for certain applications such as phase-contrast imaging.

3.6.1 Spatial coherence and source size

The electromagnetic field disturbance at points P_1, $\mathbf{u}(P_1, t_1)$ and P_2, $\mathbf{u}(P_2, t_2)$ are said to be mutually coherent if there exists a well define phase correlation between them. When the waves are merely time-delayed versions of each other — $\mathbf{u}(P, t)$ and $\mathbf{u}(P, t + \tau)$ — the phenomenon is referred to by temporal (longitudinal) coherence as in the case of a Michelson interferometer. Alternately, when the waves are two spatially-shifted versions of a primary wave — $\mathbf{u}(P_1, t)$ and $\mathbf{u}(P_2, t)$ — it is considered a case of spatial (transverse) coherence as in a Young's two-slit experiment. In both cases, fringes can be observed either in the time-domain for temporal coherence or in the space-domain for spatial coherence. The fringe visibility $\mathcal{V}$, defined as

$$\mathcal{V} = \frac{I_{max} - I_{min}}{I_{max} + I_{min}}, \tag{3.4}$$

is equal to the magnitude of the mutual degree of coherence $\boldsymbol{\gamma}_{12}(\tau)$ for interfering beams with equal intensities [60]

$$\mathcal{V} = |\boldsymbol{\gamma}_{12}(\tau)| = |\frac{\boldsymbol{\Gamma}_{12}(\tau)}{[\boldsymbol{\Gamma}_{11}(0)\boldsymbol{\Gamma}_{22}(0)]^{1/2}}|. \tag{3.5}$$

Here, $\boldsymbol{\Gamma}_{ij}(\tau)$ is the cross-correlation function of the field at P_i and P_j:

$$\mathbf{\Gamma}_{ij}(\tau) \triangleq < \boldsymbol{u}(P_i, t+\tau)\boldsymbol{u}^{*}(P_j, t) > . \tag{3.6}$$

Temporal coherence The temporal (longitudinal) coherence length l_c of a pulse, or the propagation delay over which an auto-correlation can exhibit visible fringes, can be related to the pulse's spectral bandwidth $\Delta\nu$ by:

$$l_c \approxeq \frac{c}{\Delta\nu} = \frac{\lambda_o^2}{\Delta\lambda} \tag{3.7}$$

In the case of an ultrafast Si $K\alpha$ x-ray pulse ($\lambda_o \approx 0.7$ nm) with a typical linewidth $\Delta\lambda/\lambda$ of 10^{-4}, l_c is around $7\mu m$. This implies that for interference fringes to be observed, the difference in the optical path length between the interfering waves has to be smaller than 7 μm.

Spatial coherence The spatial (transverse) coherence area A_c at an arbitrary point P_1 in space is the area comprising all points P_2 which are illuminated almost coherently ($\boldsymbol{\gamma}_{12}(0) > 0$) by an extended quasi-monochromatic incoherent source. The coherence area can be calculated using the Van Cittert-Zernike theorem [60, 61]. This theorem states that the amplitude of the equal-time degree of coherence $\boldsymbol{\gamma}_{12}(0)$ is proportional to the normalized complex amplitude at point P_2 of the diffraction pattern diffracted from an aperture at the source, of the same size, shape and intensity distribution as the source and illuminated by a spherical wave converging toward P_1 [62, 61]. Thus, for a uniformly bright, quasi-monochromatic (centered at λ_o) circular source S with radius a, at a distance z from the observation plane containing P_1 and P_2, the magnitude of the degree of mutual coherence is found by considering the Fraunhofer diffraction pattern centered at P_1 from a coherently illuminated aperture at S. From Fourier optics, the (normalized) diffracted intensity distribution from a circular aperture — and hence the mutual coherence function — is given by:

$$I(\nu_x, \nu_y) = \frac{2J_1(\sqrt{\nu_x^2 + \nu_y^2})}{\sqrt{\nu_x^2 + \nu_y^2}} \propto \gamma_{12}(0) \tag{3.8}$$

where

$$\nu_x = 2\pi \frac{a}{\lambda_o z}(x_2 - x_1) \qquad\qquad \nu_y = 2\pi \frac{a}{\lambda_o z}(y_2 - y_1) \tag{3.9}$$

Here $J_1(\nu)$ is the Bessel function of the first kind of the first order and ν_x and ν_y are dimensionless spatial coordinates related to the separation between P_1 and P_2 . Fig 3.6(a) shows that the magnitude of the mutual coherence decreases from a value of 1 (completely coherent) when P_1 and P_2 are coincident ($\nu = 0$), to a value of zero (completely incoherent) for $\nu = 3.83$. When $\nu = 1$ the mutual coherence amplitude is equal to 0.88 and the loss in mutual coherence is not significant (12 %). The corresponding transverse coherence length d_c and area A_c at P_1 are then given by:

$$d_c = \frac{1}{2\pi} \frac{\lambda_o z}{a} \qquad\qquad A_c = 0.0625 \frac{\lambda_o^2 z^2}{S}, \tag{3.10}$$

where S is the area of the source πa^2.

3.6.2 Diffractive technique for x-ray source measurement

From the preceding section (Eqs. 3.5 and 3.10) it is evident that one can determine the size of an x-ray source by measuring the visibility of the fringes obtained from a Young's double-slit experiment with a certain geometry that allows these fringes to be observed. For a given separation between the slits, the measured fringe visibility – which is equal to the magnitude of the degree of mutual coherence – gives an accurate estimation of the source size. In recent years this technique has been applied for soft x ray sources [63, 64] and coherent high order harmonic sources [65].

Geometrical considerations If we assume that the Si $K\alpha$ source size is comparable to the exciting laser spot size (~ 1 μm), then the coherence length from

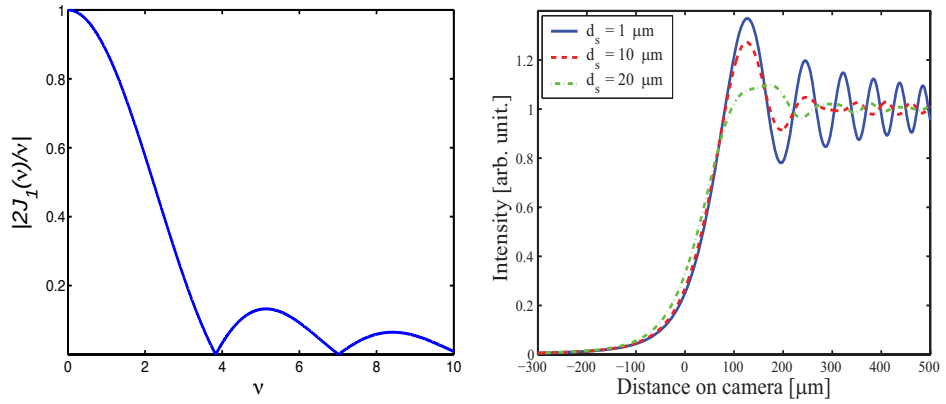

(a) (b)

Figure 3.6: (a) The normalized mutual coherence function. (b)The knife-edge diffraction pattern observed on the camera for an extended source for three different source diameters: 1μm, 10μm and 20μm.

Eq. 3.10 is equal to $10^{-4}z$. Thus, for a typical slit separation $d_{Young} = 50$ μm, the slit screen has to be placed at a distance of 50 cm or greater for the separation to be smaller to the transverse coherence length at that distance. In this geometry, it can be shown that the interfringe distance on the observation screen (camera) located at a distance L from the slit plane is equal to $\lambda_o L/d_{Young}$. Since the camera pixel size is about 20 μm, and at least four pixels are required to resolve one modulation period (interfringe distance), the camera has to be placed at a distance greater than 6 m from the slits which is cumbersome to implement physically in the laboratory and requires very long exposure times. For these reasons, we have concluded that a double slit experiment would be, at best, very hard to implement and opted for an alternative: measurement of the visibility of the fringes from the diffraction pattern off a knife-edge.

Knife edge diffraction pattern Assuming a point source, the intensity distribution of the Fresnel diffraction pattern off a straight edge can be determined by solving the Huygens-Fresnel integral and is given by [60]:

$$I = \frac{1}{2}\{[\frac{1}{2} + \mathcal{C}(w)]^2 + [\frac{1}{2} + \mathcal{S}(w)]^2\} I_o \tag{3.11}$$

where I_o is the uniform intensity in the absence of the diffracting edge and $\mathcal{C}(w)$, $\mathcal{S}(w)$ are Fresnel's integrals written as a function of the dimensionless variable w given by:

$$w = \sqrt{\frac{2}{\lambda_o}\left(\frac{1}{r'} + \frac{1}{s'}\right)}(x - x_o) \tag{3.12}$$

r' and s' are the distances from the point source to the edge plane and from the edge plane to the observation screen respectively.

For an extended uncorrelated source, the superposition principle dictates that the intensity distribution on the camera can be obtained by adding up the diffraction patterns due to each emitting point on the source. Assuming the extended source has a Gaussian intensity distribution with full width at half-maximum d_s and centered at $x = 0$, then it can be truncated by $2N + 1$ point sources at $x_i = i\frac{d_s}{N}$, with intensities $\propto \exp(-4 \ln 2\, x_i^2/d_s^2)$, for $i = 0, \ldots, \pm N$. For each point source i, the edge diffraction pattern is calculated using Eq. 3.11 with the appropriate r_i', s_i'. Finally, a summation over all i patterns in the camera coordinate plane yields the extended source knife-edge pattern. This task was performed in *Matlab* for different values of the source diameter d_s and the results are shown in Fig. 3.6(b). The source-to-edge and edge-to-camera distances were taken to be 60 cm and 4 m respectively. As expected, the fringe visibility drops as d_s increases. Thus, to measure the source size of the laser produced x-ray source, one can record the diffraction patterns from vertical and horizontal straight edges and fit those patterns to the simulation output to obtain vertical and horizontal estimates of the source size. The coherence area at a given distance from the source can then be calculated from Eq. 3.10.

3.6.3 Experimental setup

The experiment is depicted in Fig. 3.7. The Kα x-ray source was produced by focusing the pulses onto a Si target [66] using an f/1.2 off-axis paraboloidal mirror. The deformable mirror was used to optimize the spatial wavefront for a near diffraction limit focal spot of 1.2 μm diameter at half maximum (See Sect. 3.3.1).

To ensure efficient generation of isotropic K-shell line radiation, we used p-polarized pulses focused at an incidence angle of 45^o and a focal intensity on target up to 2×10^{18} W/cm^2. Also, the 500 μm-thick Si target (adhered to a flat SiO_2 substrate) was mounted on a rotating spindle attached to a translation stage that was automatically manipulated to ensure that each laser shot interacts with a fresh area of the surface.

From Eq. 3.10 it is evident that the transverse coherence length of the source at a certain distance is proportional to the wavelength. For this reason, we have chosen a low-Z target (Si, Z = 14) with a tabulated Kα peak wavelength at $\lambda_o =$ 7.13 Å corresponding to a photon energy of 1.7 keV. At such low photon energies, the x-rays are strongly absorbed in atmospheric air (transmission through 10 cm of air at 1 atmosphere $\sim 10^{-4}$), therefore the whole set-up including the x-ray CCD detector, was mounted in a vacuum environment of 10^{-3} mbar.

In order to enhance the signal to noise ratio, the laser light, as well as the low energy bremsstrahlung emission were filtered out using a Be filter. Also, a pair of permanent magnets were used to deflect the hot electrons and prevent them from generating secondary radiation in the Be filter.

We used two different knife-edges in order to study the coherence properties of the source: a set of tantalum blades forming an adjustable-size square aperture and a cleaved GaAs crystal cut along the (110) direction. The GaAs has a very smooth edge which provides a better contrast between the diffraction fringes. The knife-edge was typically mounted 60 cm away from the plasma source along the

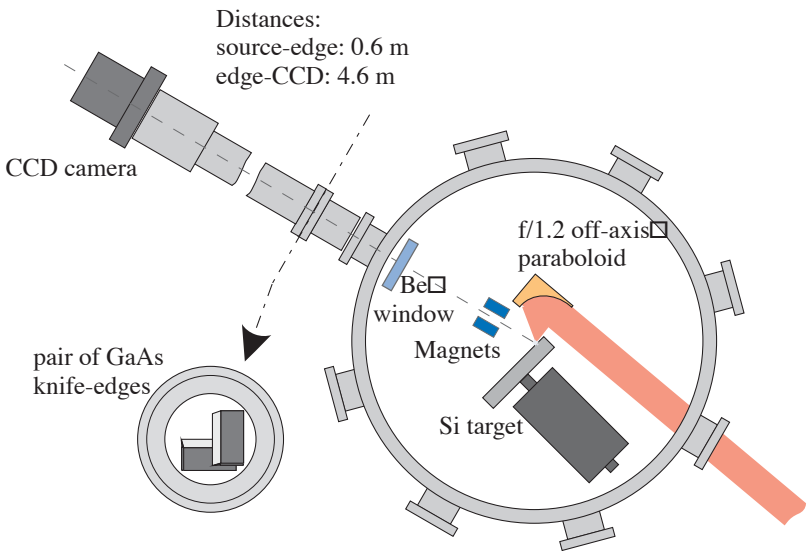

Figure 3.7: Experimental set-up used to measure the spatial coherence properties of the Si Kα source. Two orthogonal GaAs knife-edges at 60 cm from the plasma were imaged onto a cooled CCD camera at 5.2 m from the source.

target normal direction. For a micron-size source, this provides an expected spatial coherence length of several tens of microns in the plane of the knife-edge. It is worth mentioning here that the effective x-ray source size strongly depends on the laser pointing stability since integration of the x-ray signal at high repetition rate was required. We verified that the laser shot-to-shot stability is adequate by imaging the focal spot and accumulating the images over several thousands shots.

We used a 16-bit direct-detection Si CCD camera (Roper Scientific) to record the x-ray diffraction pattern. The CCD active area is 2.5×2 cm^2 with a pixel size of 19 μm. The camera was thermo-electrically cooled to -40° C where it has a quantum efficiency of about 50% at the Si Kα. X-ray patterns were recorded at a distance of 4.6 m from the edge (5.2 m from the source). At such a large distance, the x-ray flux on the detector is weak which requires an exposure time of one minute at the repetition rate of 0.5 kHz. Furthermore, to enhance the signal to noise ratio, we summed over several frames before analyzing the edges to extract the diffraction patterns. In the present setup, the optical path difference for the interfering waves forming the first few oscillations is much shorter than the longitudinal coherence

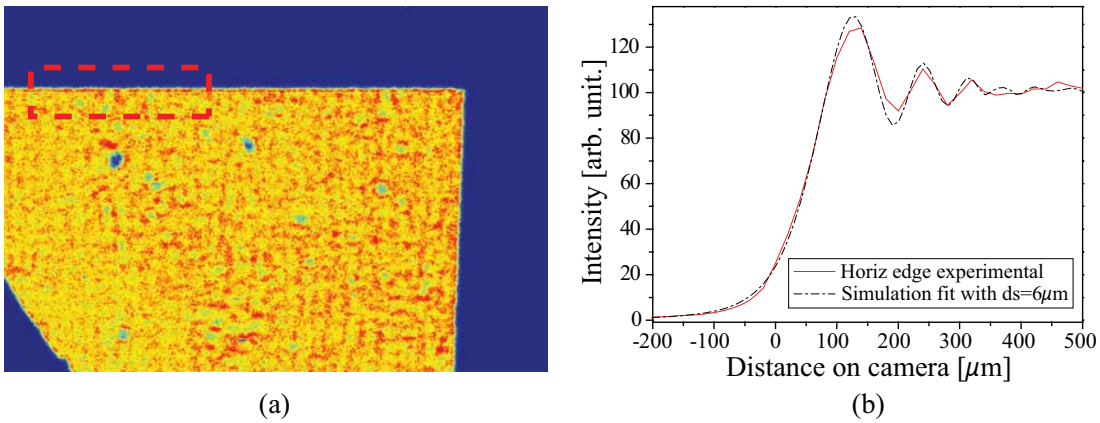

Figure 3.8: (a) X-ray image of a vertical and horizontal edges formed by GaAs wafers cleaved along the (110) direction (b) Integrated vertical line profile (solid) of the x-ray image taken along the horizontal edge (dashed inset in (a)) compared to the theoretical pattern (dashed) with a fitted source diameter $d_s = 6\mu m$.

length. For this reason temporal effects were neglected in the analysis of the fringes so that the only fitting parameter was the source size.

3.6.4 Source size measurement with GaAs edge

Typically, the diffraction patterns are obtained by integrating the horizontal and vertical line plots, to get the averaged vertical and horizontal edge profiles, respectively. In turn, the horizontal (vertical) edge profile is fitted in the above-described algorithm in order to obtain the vertical (horizontal) extent of the x-ray source. The averaged diffraction pattern over the GaAs horizontal knife-edge is shown in Fig. 3.6.3. The pulse energy and intensity in this case were 0.6 mJ and 2.5×10^{17} W/cm^2, respectively. Three fringes can clearly be observed. The best fit (convolution of the Fresnel diffraction pattern along the source spatial extent) is achieved for a source diameter of 6.0 $\pm$ 0.5μm in vertical, and of 9.0 $\pm$ 0.5 μm in horizontal due to the 45° projection of the laser pulse onto the surface of the target.

For a fringe visibility $\mathcal{V} = 0.88$, the measured x-ray source size (radius $a = 3$ μm) yields a transverse coherence length $l_c \cong 20$ μm at a distance $z = 60$ cm (Eq. 3.10). This transverse coherence length is of the same order of magnitude as the

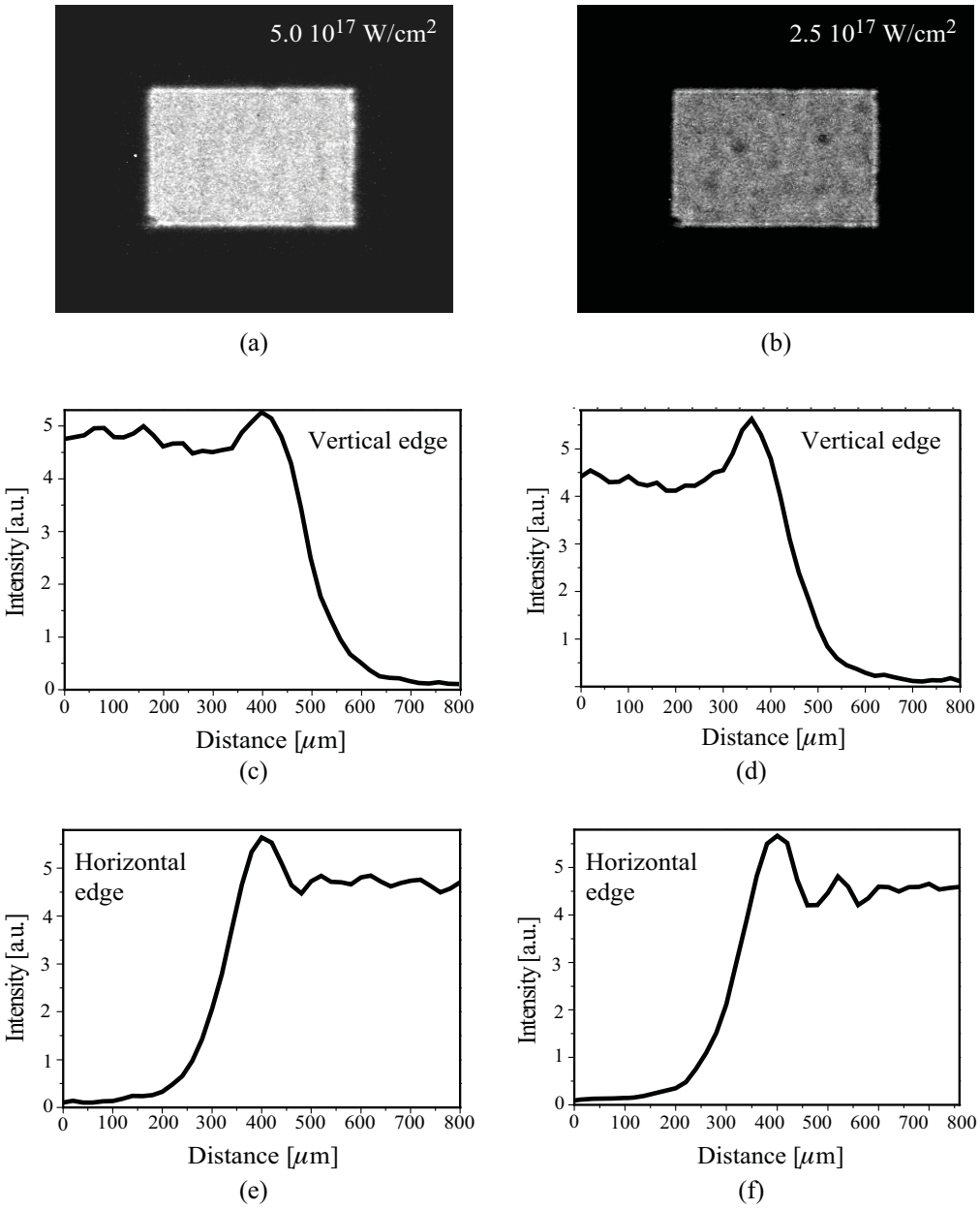

Figure 3.9: X-ray images (a, b) and integrated line plots along the vertical (c, d) and horizontal (e, f) edges of tantalum edges at a laser intensity of $5 \times 10^{17}\mathrm{W/cm}^2$ (a, c, e) and $2.5 \times 10^{17}\mathrm{W/cm}^2$ (b, d, f).

x-rays from synchrotron radiation facilities. Furthermore, this coherence area can be significantly increased in the horizontal dimension by looking at the x-ray source from a grazing angle. In this geometry the effective horizontal source size is reduced by the projection factor while the x-ray flux remains unchanged due to the isotropic nature of the Kα emission [52]. As an example, a transverse coherence length l_c of 77 μm can be obtained for a knife-edge positioned at an angle of 75° with respect to the target's normal (an effective source size $a_{eff} \cong a.\cos(75°) = 0.7$ μm). Although the coherence length could be increased considerably up to several hundred microns at smaller grazing angle, the x-ray flux however is expected to drop [52] reducing the number of coherent photons.

3.6.5 Spatial coherence dependence on laser intensity

The effects of laser intensity on the spatial coherence properties were investigated in the same geometry as the above experiment. Without changing the laser spot size, the laser output power was varied by means of a waveplate and polarizer between the full power (1300 mW) corresponding to an intensity of $I = 5 \times 10^{17}$ W/cm^2 and 670 mW corresponding to an intensity of $I = 2.5 \times 10^{17}$ W/cm^2. Figures 3.9(c) and (d) show averaged line-plots of the horizontal and vertical edges for the tantalum aperture at a laser intensity of $I = 5 \times 10^{17}$W/cm^2 and 2.5×10^{17} W/cm^{2}respectively. Note that the visibility of the fringes for the tantalum knife-edge is lower than for the GaAs edge, as it can be clearly seen comparing the figures 3.9(f) and 3.6.3(b) recorded at the same laser power and along the same direction. This is due to a lower edge sharpness in the case of the tantalum compared to the GaAs. At the lower laser intensity, a high contrast diffraction peak without any visible fringes is observed across the vertical edge (Fig. 3.9(d)) whereas two maxima and two minima are clearly distinguished across the horizontal edge (Fig. 3.9(f)). This indicates, as expected, that the horizontal dimension of the x-ray source is larger

than the vertical dimension due, in part, to the projection factor of the beam onto the target surface. Also, for both edges, the visibility and contrast of the fringes seems to decrease with increasing intensity, suggesting an increase in the x-ray source size. Therefore, increasing the laser power reduces the transverse coherence length, although it increases the total number of photons. This is rather intuitive if one considers a simplified x-ray production picture. Higher intensities drive hotter electron distributions. These can then penetrate deeper into the target material, increasing the volume throughout which the Kα photons are generated which result in the reduction of the transverse coherence area in a given geometry.

3.6.6 Applications

Ever since the first x-ray shadowgraph was recorded by Roentgen in 1896, x-ray imaging has proven to be of utmost usefulness for a plethora of applications ranging from clinical and medical diagnostics, to industrial testing and inspections. All these techniques, be it 2-dimensional projection imaging or tomographic 3-D reconstructions, rely on the contrast in absorption that the x-rays experience as they penetrate through different structures of the imaged object. Thus, resolution limitations become significant if the object of interest contains structures with very similar composition (and hence absorption coefficient) as it is the case in early-detection mammography for example. However, if an x-ray source with a high degree of spatial coherence was used, diffraction effects could be observed at the interfaces separating different structures within the object. Thus, under certain geometrical considerations, both intensity (due to absorption) and phase information could be recorded on the image plane. This technique, commonly referred to by phase-contrast imaging has been demonstrated in the mid-nineties using x-rays from synchrotron sources [67, 68, 69].

More recently, Toth *et al.* [70] investigated the feasibility of a phase-contrast

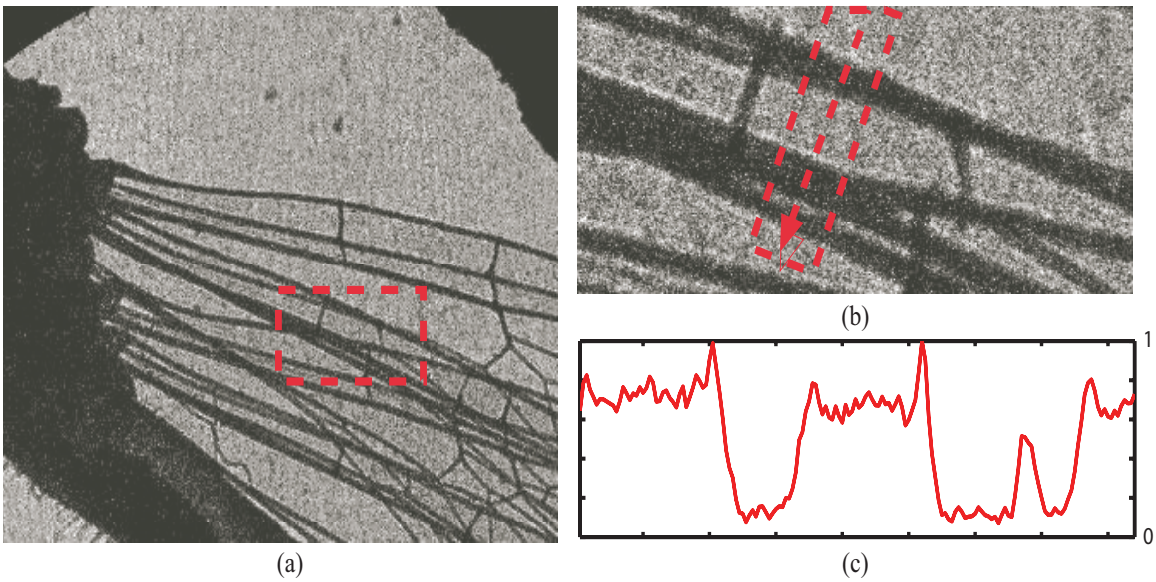

Figure 3.10: Background-subtracted x-ray image of a Damsel fly (a) taken with at a laser intensity of 2.5×10^{17} W/cm^2. The insect and the imaging CCD were mounted at 60 cm and 5.2 m away from the plasma, respectively. The exposure time was 5 minutes at the repetition rate of 0.5 kHz. A detailed view of the wing structures (b) shows phase contrast effects along the edges characteristic of a high degree of spatial coherence in this geometry. The integrated line profile in (c) was drawn along the arrow direction in (b).

imaging system, at the Mo Kα, driven by 600 mJ, 60 fs laser pulses. In this study, images taken with a large object-to-detector distance, showed a qualitative enhancement of the edge contrast compared to images taken with the detector mounted close to the object.

A similar result was obtained in the λ^3 regime with a Si Kα source. Here the distances from the x-ray source to the object – a damselfly – and the CCD were 0.6 and 5.2 m respectively. The laser peak intensity was kept around 2.5×10^{17} W/cm^2 to ensure a small x-ray source size, and consequently large transverse coherence length. Fig. 3.10(a) shows a background-subtracted image taken with an exposure time of 5 minutes at 500 Hz repetition rate. Integrated line plots 3.10(b,c) clearly show high-contrast modulations along various interfaces suggesting the compatibility of the λ^3 system with potential phase contrast imaging techniques. This could have a positive impact on clinical radiography, since these techniques offer a much needed increase in resolution, unattainable with conventional x-ray tubes.

CHAPTER IV

RELATIVISTIC ELECTRON GENERATION AND CHARACTERIZATION

More than twenty years since laser-plasma experiments at relativistic intensity were first undertaken, the mechanisms of energy transfer from the intense electromagnetic wave to the plasma are yet to be fully understood. This is partially due to the large number of parameters that define such interactions, namely the laser intensity temporal and spatial profiles, the target composition and the plasma density scale-length during the interaction. The characterization of the hot electrons generated from a relativistic laser-plasma interaction is doubly important: First it offers a direct plasma diagnostic that could further the understanding of the underlying physics. Second, the production and control of relativistic electron beams could be of great importance to the fast ignitor scheme for inertial confinement fusion (ICF) [71, 72], as well as with regard to many other applications such as time-resolved electron diffraction [73] and laser-driven positron [74, 75] and ion sources.

To date, all relativistic intensity experiments have been carried out using large laser facilities producing at least several hundred millijoule pulses at a repetition rate of 10 Hz or lower. Therefore, studies concerned with the scaling of hot electron temperature in this regime were often plagued with insufficient statistics and laser pulse-to-pulse stability problems. In contrast, the λ^3 laser system described in section 3.2 makes accessible, for the first time, relativistic intensities with high-contrast

millijoule pulses delivered at the kilohertz rate.

Throughout this chapter, we describe a series of experiments aimed at characterizing the spatial and energy distribution of hot electrons emitted from the interaction of a λ^3 relativistic laser with both metal (Al) and dielectric (SiO_2) targets. These experiments were conducted over a range of laser intensities ($10^{17} - 2 \times 10^{18}$ W/cm^2) and incidence angles (oblique and grazing). Additionally, a pre-pulse with a controllable delay was introduced to study the effects of the plasma scale-length. The energy distribution measurements were obtained by accumulating hundreds of laser shots on a magnetic-field electron spectrometer that uses an absolutely calibrated imaging plate as a detector.

4.1 The electron spectrometer

Time of flight measurements are effective for measuring the energy distribution of low kinetic energy electrons ($<$ 100eV). However, at relativistic energies, the electron velocity becomes comparable with the speed of light ($v/c = 0.86$ for $E = m_o c^2$), making it extremely difficult to resolve the high-energy end of the spectrum with nanosecond electronics. For this reason, we have opted to use a dispersive magnetic field spectrometer with a detection range that spans from 50 keV to $\sim$ 3 MeV.

The spectrometer (Fig 4.1) uses a pair of 9×11 cm permanent magnets separated by a 2.5 cm gap. The magnetic field in the median plane is nominally 1.1 kG. An 8 cm long nylon tube with an aperture diameter of 0.8 mm is used to collimate the electron beam entering the spectrometer. For a typical distance of $\sim$ 5 cm from the plasma, this collimator limits the input electron beam to a divergence of $\sim$ 30 μsr. Due to the close proximity of the spectrometer to the interaction, the electromagnetic pulse (EMP) noise could easily damage any electronic detectors or CCDs. For this reason we have chosen to use imaging plates (FUJI BAS-SR 2025) to record the dispersed electron signal.

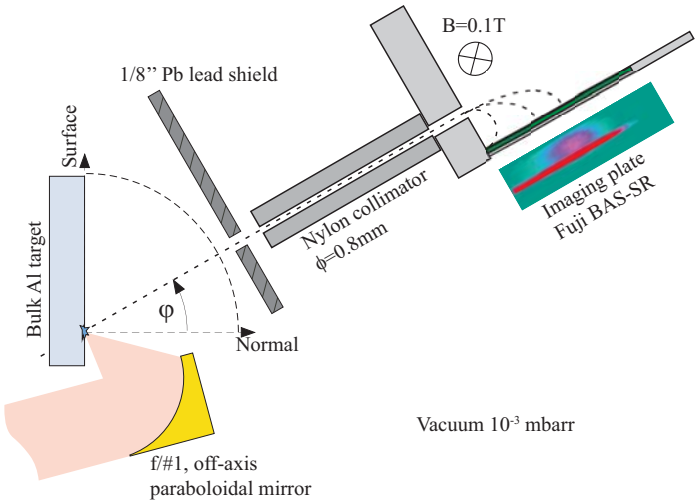

Figure 4.1: Experimental set-up used to measure the electron energy distribution showing the electron spectrometer.

Imaging plates (IP) are re-usable x-ray films that were primarily developed for clinical medical use. They use photo-stimulated luminescence (PSL) in crystals, such as $BaFBr : Eu^{2+}$, to store a signal that is related to the deposited energy. This signal is subsequently read by stimulating the fluorescence centers using a laser at visible wavelength. In the absence of read-out light, the stored signal spontaneously decays with a characteristic time of the order of several hours. The spatial resolution of imaging plates is limited by the resolution of the scanner used for the read-out. In our case we use a Fuji BAS-100 II series scanner with a maximum resolution of 50μm. Although this resolution is coarser than what can be achieved with direct exposure film (DEF), IPs have many advantages that make them attractive when high resolution is not of utmost importance. In fact, IPs are > 100 times more sensitive to hard x-rays (and electrons) than DEF [76] and possess a dynamic range of 5 orders of magnitude (compared to ~ 2 for DEF). Additionally, they are insensitive to the laser and visible wavelengths and do not require chemical development processes.

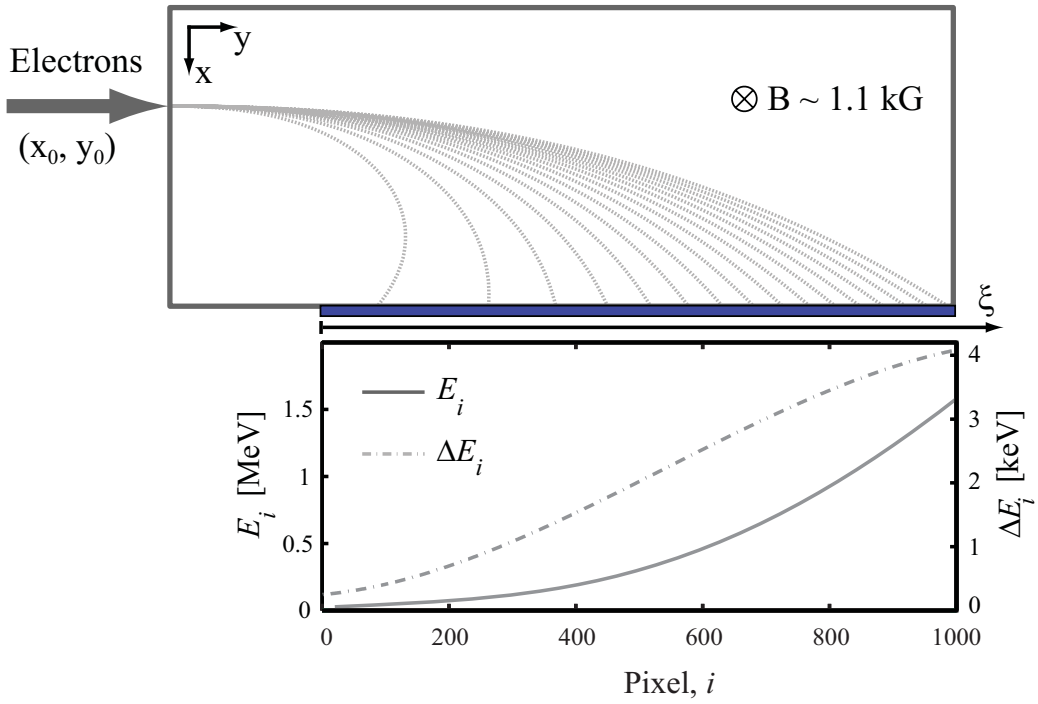

Figure 4.2: The top figure shows the calculated electron trajectories in the non-uniform magnetic field of the spectrometer. The position where the trajectories intersect the imaging plate (in blue) is used to map the pixel index i to its corresponding electron energy E_i in MeV (bottom, solid line). Also shown (bottom, dashed line) is the channel width ΔE_i, that describes the energy resolution, in keV, at pixel i for a point-like spectrometer slit. The pixel size is 50 μm.

4.1.1 Spectrometer calibration

The calibration of the spectrometer involved two separate steps: (i) Mapping position along the IP to electron energy to obtain the energy distribution of the PSL signal. (ii) Calibrating the electron response to obtain the absolute electron energy distribution function dN/dE.

The first task was carried out numerically by tracing the trajectories, within the spectrometer, for a set of electron energies E_i in our range of interest (see top Fig. 4.2). To this end, the magnetic field was measured along a Cartesian grid and interpolated to produce $B\,(x, y)$, the field strength at coordinates (x, y). Next, the electron position (x, y), and velocity (v_x, v_y) were incrementally updated by locally

solving the relativistic Lorentz equation (with $\mathbf{E} = 0$):

$$\gamma m_0 \frac{d\mathbf{v}}{dt} = -e\,[\mathbf{v} \times \mathbf{B}\,(\mathbf{x}, \mathbf{y})]\,. \tag{4.1}$$

The time increment was made sufficiently small so that, for a uniform magnetic field B_0, the electrons follow circular trajectories with the expected relativistic *Larmor radius*:

$$\begin{aligned} R_L &= \gamma\,\frac{m_0\,v}{e\,B_0} \\ &= \frac{m_0\,c}{e\,B_0}\,\sqrt{\left(\frac{E_i + m_0\,c^2}{m_0\,c^2}\right)^2 - 1}. \end{aligned} \tag{4.2}$$

From the geometry and the computed trajectories, the mapping that relates the electron energy E_i to its exit coordinates (or position ξ along the IP) was deduced and fitted to a fourth-degree polynomial in ξ:

$$E_i = \sum_{i=0}^{4} a_i\,\xi^i \tag{4.3}$$

Figure 4.2 (bottom) shows the function described in Eq. 4.3 plotted (solid line) in terms of the scanned IP pixel number, assuming a pixel size of 50 μm. Also plotted (dash-dotted line) is the pixel *bandwidth* ΔE_i which describes the width of energy-distribution slice at pixel i, assuming an infinitely narrow input aperture. For a 0.8 mm wide collimator, this translates into an energy resolution that varies between 10 keV (for $\sim$ 100 keV electrons) and 60 keV (for 1.7 MeV electrons).

To test the validity of this calibration procedure, we measured the electron energy distribution from a radioactive isotope, Cs^{137}, which emits both β- and γ-radiation. The γ rays, with 663 keV photon energy, undergo an internal conversion to produce a narrow electron distribution peaked at 625 keV [78]. Due to the low activity of the source we used (< 0.1 μCi), the spectrometer collimator was shortened to about 1 cm in order to increase the signal on the IP at the expense of energy resolution. Figure

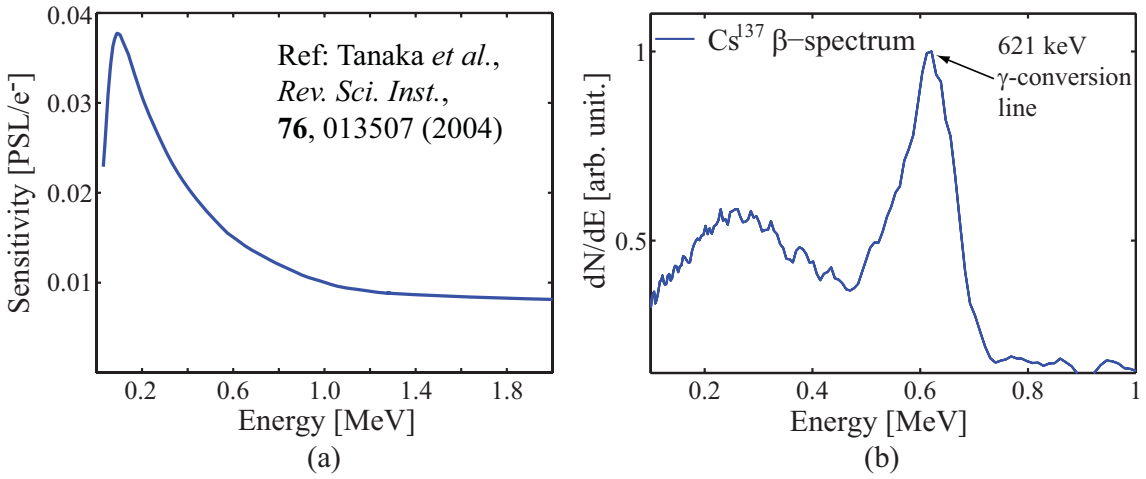

Figure 4.3: (a) Sensitivity curve giving the PSL value per electron as a function of the electron energy from [77]. The spectrometer calibration was verified by measuring the β-spectrum of Cs^{137} isotope (b) with a tabulated internal-conversion line at 625 keV.

4.1.1(b) shows the calibrated spectrum from Cs^{137} for an exposure time of 8 hours. The internal conversion peak occurred at 621 keV, albeit its linewidth is strongly broadened because of the large admittance angle of 5 msr in this measurement. This showed that the calibration of the energy axis has an accuracy better that 1 % around 620 keV.

The second step of the spectrometer calibration consisted of transforming the raw IP signal to absolute electron distribution function, dN/dE, in units of electrons per 0.01 MeV bandwidth, emitted in a unit solid angle, from a single laser pulse. Starting from a scanned IP image, we normalized the data for the scanning parameters using a manufacturer-provided formula that relates Q_i, the gray-scale value at a pixel i, to its corresponding PSL signal PSL_i:

$$PSL_i = \left(\frac{R}{100}\right)^2 \times \frac{4000}{s} \times 10^{L\times\left[\frac{Q_i}{G}-\frac{1}{2}\right]} \tag{4.4}$$

Here, R is the pixel size in μm, s and L are the scanner sensitivity and latitude set to 4000 and 5, respectively, and G is the gradation equal to 65,535 for 16-bit images. Next, the PSL data was integrated across the dispersion direction to obtain F_i^{PSL},

the total PSL distribution as a function of pixel position i along the IP. From the energy axis calibration (Eq. 4.3), this is subsequently transformed to $F^{PSL}(E_i)$, the PSL distribution in terms of electron energy E_i.

In order to transform from PSL to electron number distribution, we relied on the sensitivity curve from Tanaka *et al.* [77] (reproduced for our range of interest in Fig. 4.1.1(a)) and obtained $f(E_i)$ such that $f(E_i)\,\Delta E_i$ is the total number of detected electrons with energy between E_i and $E_i + \Delta E_i$. The total number of electrons with energy higher than some arbitrary E_{min} is then given by:

$$N_{E>E_{min}} = \sum_{E_i>E_{min}} f_i(E_i)\,\Delta E_i$$

Since ΔE_i depends on the pixel position i, it was convenient to normalize the distribution function for a constant $dE = 0.01$MeV. Thus, we obtained the energy distribution function, $f_N(E_i)$ which describes the number of electrons at energy E_i, within a bandwidth of dE, emitted per second, per unit solid-angle.

$$f_N(E_i) = \frac{dN}{dE}(E_i) = f_i(E_i)\,\Delta E_i \times \frac{1}{\Delta E_i}.$$

Figure 4.4: IP raw image of the dispersed electron signal (b) juxtaposed next to the signal recorded by a witness plate (a) placed opposite the collimator aperture that measures the x-ray signal.

In order to assess the contribution of the x-rays on the electron signal a witness IP (Fig. 4.4 (a))was placed opposite the collimator aperture, far enough behind the magnetic field, where all electrons with energies up to 5 MeV are expected to be fully deflected. Thus, the signal recorded on the witness IP was due to primary x-rays that travel through the collimator as well as secondary x-rays and electrons

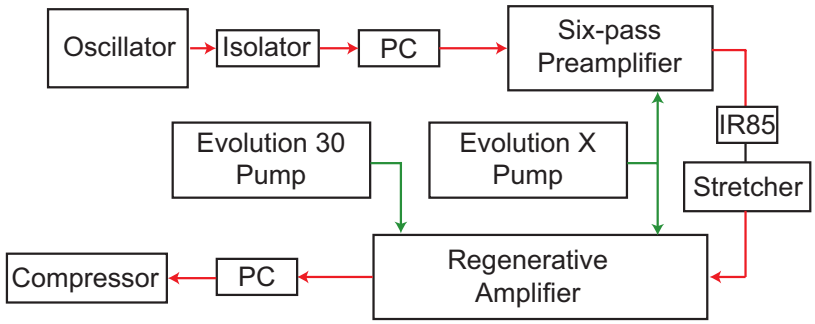

Figure 4.5: Block diagram of the post-upgrade λ^3 laser system

scattering within the spectrometer. The relative sensitivity of the IP to the x-rays can be estimated by taking the ratio of the integrated x-ray signal (a) to the integrated electron signal shielded from the primary x-rays (b). This ratio was found to be of the order of ~ 0.004, therefore it was acceptable to neglect the contribution of x-rays and secondary radiation in the preceding analysis.

4.2 Experimental set-up

4.2.1 Laser contrast

Concerns over the beam pointing stability and mode quality at the output of the system described in section 3.2 prompted a redesign of the last two multi-pass stages into a single regenerative amplifier (Fig. 4.5). All experiments discussed in the present chapter were performed using the upgraded system..

The regenerative stage amplified the 100 nJ stretched seed pulses to 8 mJ in 11 round-trips with two passes on the Ti:Sapphire crystal for each round trip. The crystal was pumped from both ends with up to 30 mJ from two frequency-doubled, diode-pumped Nd:YLF lasers (Spectra Physics, Evolution X and Evolution 30). At the maximum pump level, the system produced up to 2.5 mJ pulses on target. Focused to a spot of 1.5 μm diameter (FWHM), peak intensities as high as 2.4×10^{18} W/cm^2 were attained.

Relativistic intensities are many orders of magnitude higher than the damage

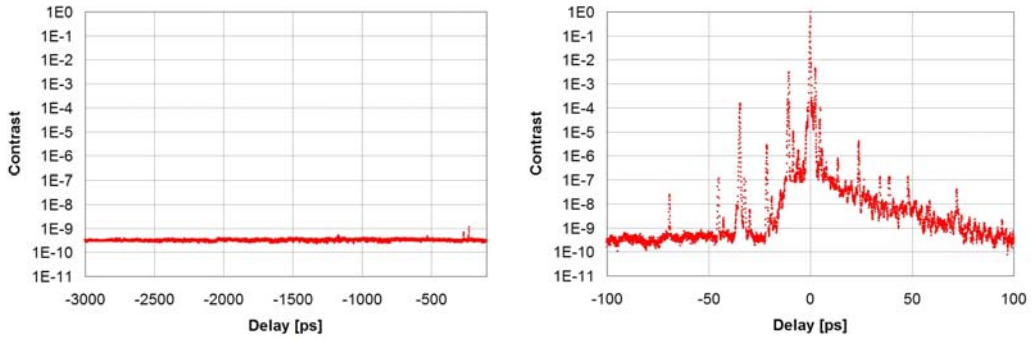

Figure 4.6: Third order correlator traces showing a contrast better than 10^{-9}, 50 ps prior to the main pulse. All spikes preceding the main pulse in the ps scale (b) are identified as artifacts of the measurement.

threshold for all materials ($10^9 - 10^{11}$ W/cm^2 for nanosecond pulses). Therefore, if the contrast in intensity between the peak of the femtosecond pulse and the preceding amplified spontaneous emission (ASE) pedestal is not sufficiently high, a pre-plasma will form and alter the electron density profile. Since the physics of laser absorption in the plasma strongly depends on the density scale length, it is very important to understand and control the pre-plasma formation. In term of laser design, this justifies the need for highest levels of ASE and pre-pulse suppression which is achieved by incorporating pulse cleaning devices such as the saturable absorber and the Pockels cell set-up at the output [79].

A third-order autocorrelator set-up was built to measure the contrast of the compressed laser pulses [80]. The traces are shown in Fig. 4.6. At 50 ps prior to the main pulse, the contrast was found to be better than 5×10^{-9}. The contrast decreases to $\sim 10^{-4}$ during the last few ps preceding the femtosecond pulse. All of the femtosecond prepulses showing in the Fig. 4.6 are attributed to artifacts from the correlator setup.

4.2.2 Set-up

The electron spatial distribution measurements were carried out in the single-shot regime using a variation of the set-up shown in Fig. 4.7. Energy distribution

measurements required the integration of 200-500 shots with the electron spectrometer from Fig. 4.1 installed at some angle ϕ from the target normal. Throughout these experiments, the laser delivered 32 fs pulses with up to 1.5 mJ on target. As in the case of x-ray experiments described in section 3.3.1, we used an f/1.2 off-axis paraboloidal mirror along with the deformable mirror in order to reach relativistic intensities in a focal spot of 1.5 μm FWHM.

Both dielectric (SiO_2) and metallic (Al) targets were used throughout this set of experiments. The targets had optical quality surfaces and were translated to ensure that each laser pulse interacts with a fresh target area. Since we expected the plasma scale-length to strongly affect electron emission characteristics, we installed a prepulse beam with a controllable delay (up to $\sim$ 100 ps prior to the arrival of the main pulse). The prepulse was extracted from the Fresnel reflection off a 3 mm-thick plate mounted before the compressor. The prepulse was then compressed in a dedicated grating compressor to a duration of 30-40 fs. After going through a

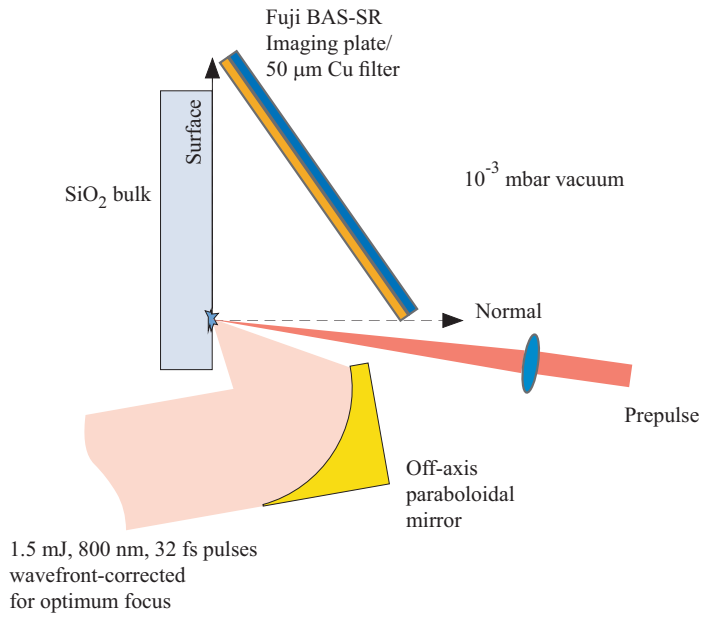

Figure 4.7: The set-up used to measure the spatial distribution of the hot electrons. A prepulse with controllable pre-delay was introduced to control the plasma scale-length. The electron signal was recorded on a Fuji BAS-SR imaging plate covered with a 50μm Cu filter that cuts off lower energy electrons $<$ 200keV.

delay stage, it was focused with 7.5 cm focal length doublet, yielding a focal spot with $\sim 30\mu$m diameter. The prepulse energy on target was $\sim 50\mu$J and its peak focal intensity was $1 - 2 \times 10^{14}$ W/cm^2.

4.3 Scaling of hot electron temperature with laser intensity

The scaling of hot electron temperature with the laser intensity has been extensively studied both experimentally [81, 82] and using particle-in-cell (PIC) simulations [28, 31, 27]. Throughout most published results – obtained over a wide range of laser wavelengths – it was found that the electron temperature scales with the product parameter $I\,\lambda^2$ rather than the proper intensity I. This is attributable to the fact that electron quiver energy is related to the ponderomotive potential (Eq. 2.7), which, in turn, can be expressed in terms of the vector potential $a_0 \sim (I\,\lambda^2)^{1/2}$.

In this section we report on the scaling of electron temperature from a bulk Al target in the relativistic λ^3 regime. The temperatures were extracted from directly measured energy distribution functions and fitted – in the $10^{17} - 2 \times 10^{18}$ W/cm^2 intensity range – to an expression of the form:

$$T_h = \alpha \left(I\,\lambda^2\right)^{\gamma}. \tag{4.5}$$

Additionally, a simple theoretical model based on energy conservation is proposed to explain the measured temperatures.

4.3.1 Al plasma scale-length: HYADES simulation

As previously stated, the physics of laser energy coupling to the plasma electrons depends critically on the electron density profile (or scale-length L_n as defined in Eq. 2.18) at the instant of the interaction. Since autocorrelation measurements (section 4.2.1) showed that the nanosecond pedestal could exceed the Al damage

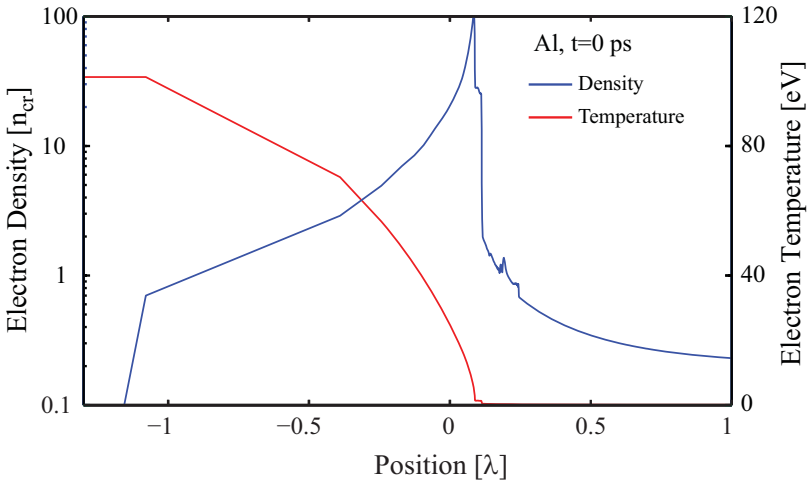

Figure 4.8: HYADES simulation showing the electron density (blue) and temperature (red) profiles at the time of arrival of the main pulse.

threshold within the last 100 ps preceding the intense femtosecond pulse, it was important to model the time evolution of the plasma electron temperature and density profile during that temporal window. This task was done using HYADES, a one-dimensional lagrangian hydrodynamic code [83].

In the simulation, the target was modelled by a 1 μm-thick mesh and described using the Al equations of state derived from the Sesame library (table 44). We chose the average atom model to determine the degree of ionization. The energy source was a time-dependent, p-polarized laser source, incident at 45°, with an intensity profile that matches the third-order correlator measurements described in section 4.2.1. Fig. 4.8 shows that, at the time the peak of the femtosecond pulse reaches the target, the critical surface would have shifted by about a wavelength toward the vacuum, from its initial position ($x = 0$). Furthermore, the slope of the electron density, measured at that same instant around the critical surface, indicates that the scale-length of the Al plasma is about $\lambda/3$. The corresponding electron temperature is ~ 90 eV.

4.3.2 Spatial distribution

The particular heating mechanism that dominates a laser-plasma interaction, not only affects the temperature of the hot electrons produced, but also their spatial distribution. For instance, resonance absorption accelerates the electrons along the **k**-vector direction of the excited plasma waves (typically along the target normal direction). $\boldsymbol{j} \times \boldsymbol{B}$ heating, in contrast, is known to produce a hot electron jet along the laser direction (both forward and specular directions). For this reason, it is important to characterize the spatial distribution of the electrons produced from the λ^3 focus and correlate this measurement to the energy distribution measurement.

The distribution of the hot electrons generated in the Al plasma was measured in a set-up similar to the one depicted in Fig. 4.7. In this set of results, the intentional pre-pulse was not used, and therefore, the preplasma was only due to the laser pedestal. According to the HYADES simulation, the 1.5 mJ femtosecond pulse interacted with a plasma scale-length of the order of $\lambda/3$. 50 and 100 μm-thick Cu filters were used to cut-off electrons with an energy lower than 150 and 240 keV, respectively (continuous slowing down range approximation, CSDA). Additionally, a second imaging plate layer was stacked behind the primary strip to record the distribution of electrons sufficiently energetic ($\gtrsim$ 450 keV) to go through the Cu filter and the first imaging plate layer.

Figure 4.9 shows electron spatial distribution for p-polarized pulses, incident at 45°, with an intensity of $\sim 2 \times 10^{18}\mathrm{W/cm}^2$. The filters used are: 50 μm Cu (a), 100 μm Cu (b), and a second imaging plate layer (c). The vertical lines mark the surface, specular and target normal directions, from left to right, respectively. The middle horizontal line in (a) and (b) lies in the laser incident plane and the peripheral horizontal lines delimit ±10° altitude measured with respect to the incidence plane.

Most of the hot electrons ($T_h > 150$ keV) are primarily emitted within two broad jets: a *specular* jet that lies between the reflected laser direction and the target

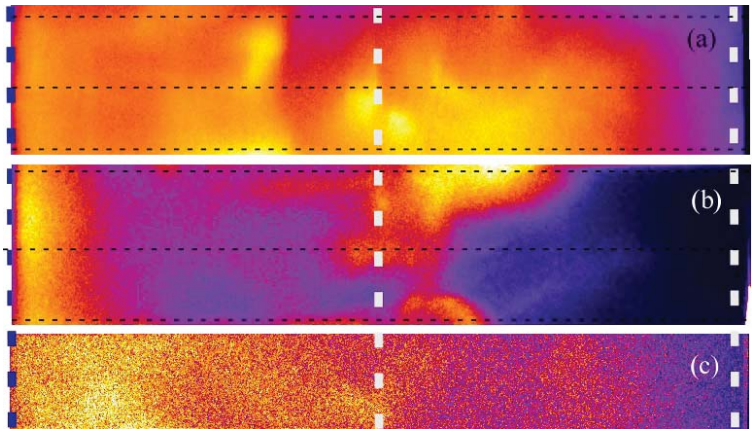

Figure 4.9: Electron spatial distribution from Al target for p-polarized pulses at 2×10^{18} W/cm^2 incident at 45° for a 50 μm Cu filter (a), 100 μm Cu filter (b), and a back IP layer with another 50 μm Cu filter (c). The vertical lines from left to right mark the surface, specular and normal directions.

normal, and a surface jet (Fig. 4.9(a)). Higher energy electrons ($T_h > 240$ keV) are confined in narrower beams, still along the specular and surface directions (Fig. 4.9(b)), with the most energetic ones emitted toward the target surface direction (Fig. 4.9(c)).

The Al plasma jets are characterized by the presence of a number hot spots or *beamlets* that did not reproduce well from shot to shot. This suggests that the electron heating mechanisms are prone to instabilities forming in the long-scale-length plasma such as the filamentation of the laser or the electron beam.

4.3.3 Energy distribution: Experimental

The energy distribution of hot electrons from the Al plasma was studied in the intensity range between 10^{17} W/cm^2 and 2×10^{18} W/cm^2. The spectra were measured along the laser specular direction (45° off the target normal), by accumulating the signal from $\sim 500 - 5000$ shots. This averaging reduces the uncertainties due to the poor shot-to-shot reproducibility of the hot spots within the electron jet.

The spectra, expressed in electron number per 10 keV bandwidth emitted in a unit solid angle per laser shot (dN/dE), are plotted in Fig. 4.10. As it is the case

in other solid density experiments, the hot electron spectra can be fitted into a Maxwellian distribution with a temperature T_h:

$$\frac{dN(E)}{dE} \sim \sqrt{E}\,\exp\left(-E/T_h\right). \tag{4.6}$$

At intensities higher than 10^{18} W/cm^2, however, a single-temperature Maxwellian is not sufficient to describe the energy distribution. Therefore, in addition to a first temperature T_{h1} describing the lower-energy part of the distribution, a second temperature T_{h2} is used to model the high-energy tail. This two-temperature behavior has been previously reported from both simulations [84] and experiments [85] and is thought to be caused by competing heating mechanisms acting on different electron groups. At the maximum intensity of 2.6×10^{18} W/cm^2, the hot electrons reach energies as high as 1 MeV, and the two-temperature-Maxwellian fit yields $T_{h1} \sim 153$ keV, $T_{h2} \sim 270$ keV. In contrast, at $\sim 10^{17}$ W/cm^2 (~ 70 μJ), the energy distribution can be described with a single temperature Maxwellian ($T_h = 21$ keV) with a maximum electron energy of ~ 200 keV.

Although imaging plates are specified by the manufacturer to have a dynamic range of about 5 orders of magnitude, intensity-dependent background – possibly due to electron scattering inside the spectrometer assembly and secondary radiation – limited the useable signal to $2-3$ orders only.

4.3.4 Energy distribution: PIC simulations

In addition to the experimental measurements, the hot electron energy distribution was studied using 2-D and 3-D Particle-In-Cell (PIC) simulations. The model assumes a 30 fs, p-polarized laser, focused to a 1 μm spot on an initially cold plasma with an electron density profile that drops exponentially from 7 n_{cr} to 0.03 n_{cr} over a distance of 1μm. This corresponds to a scale-length of $L_n \simeq \lambda/2$. The number of particles in each cell was 60 for the 2-D case and 30 for the 3-D case.

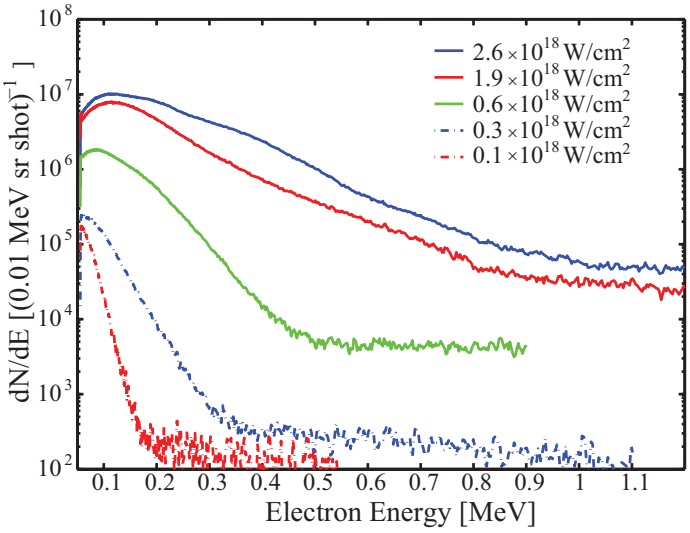

Figure 4.10: Electron energy distribution functions from an Al plasma for different laser intensities. The spectra were taken along the laser specular direction for an incidence angle of 45°.

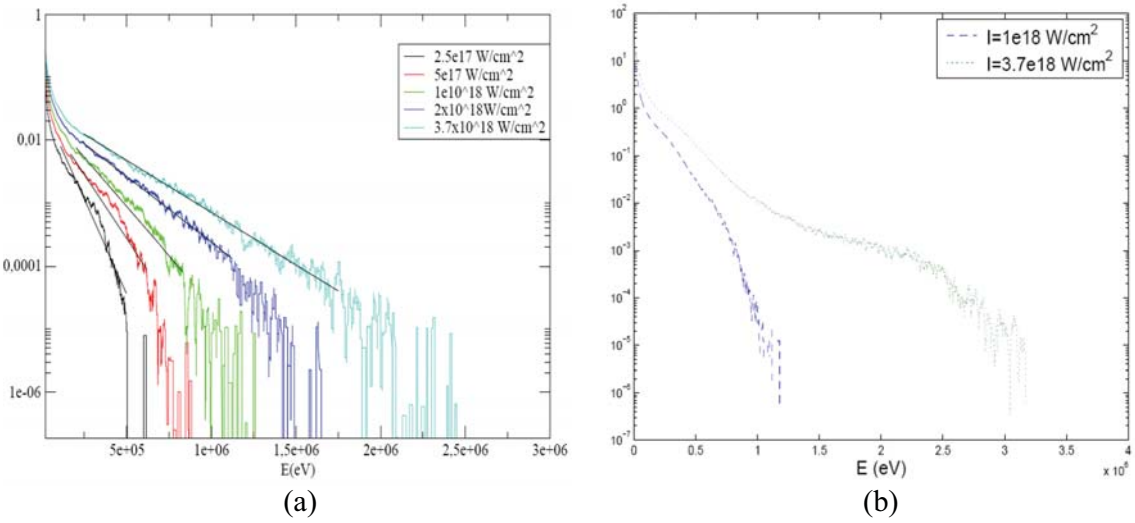

Figure 4.11: Electron energy distributions obtained from 2-D (a), and 3-D simulations (b). Note that the 3-D results reveal a two-temperature distribution for an intensity of 3.7×10^{18} W/cm^2.

The energy distributions obtained from 2-D simulations are shown in Fig. 4.11(a). Even at relativistic intensities, the spectra do not show a higher temperature component in the distribution tail, as observed in the experiments. Moreover, the temperatures obtained from the 2-D runs overestimate the experimental results by as much as $\sim 50\%$ throughout the intensity range. On the other hand, the hot-temperature results from the 3-D simulations agree well with the measurements.

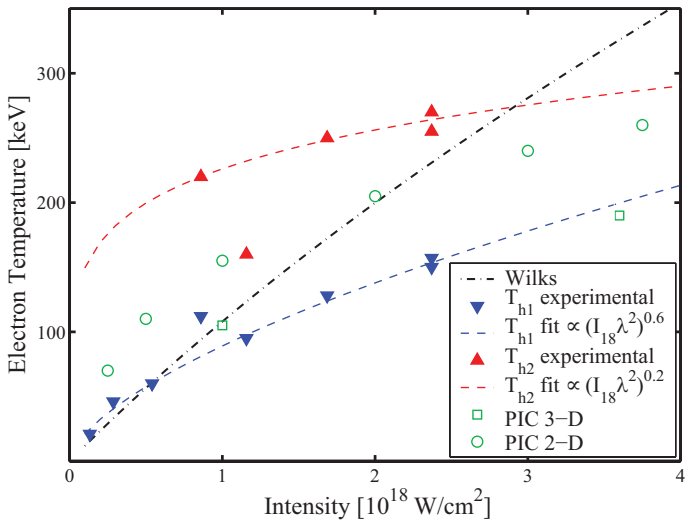

Figure 4.12: The hot electron temperature scaling with laser intensity. The experimental energy distributions were fitted to two-temperature Maxwellians with two 'hot' components T_{h1} (blue) and T_{h2} (red triangles). Both T_{h1} and T_{h2} were fitted to power laws $\propto \left(I_{18}\lambda^2\right)^{\gamma}$, with $\gamma = 0.6$ and 0.2, respectively. The Wilks scaling (dashed line) as well as 2-dimensional (circles) and 3-dimensional (squares) PIC simulation results are also shown.

In this case, a hotter-temperature component in high-energy tail of the spectra is observed at a laser intensity of 3.7×10^{18} W/cm^2(Fig. 4.11(b)).

4.3.5 Scaling laws

After the spectra are fitted to Maxwellian distributions, the hot electron temperatures are extracted and plotted as function of the laser intensity (Fig. 4.12). The experimental results from the lower-energy component of the distribution (T_{h1}) are plotted in downward triangles, and those from the high energy tail (T_{h2}) in upward triangles. 2-D and 3-D simulations are represented on the same graph using open circles and squares, respectively. For reference, the Wilks scaling in Eq. 2.32 [31], which expected to be dominant at relativistic intensities, is also plotted in a dot-dashed line.

It is evident from Fig. 4.12 that the Wilks formula fails to describe the scaling of either T_{h1} or T_{h2} at intensities higher than $\sim 10^{18}$ W/cm^2. The 2-D simulations, however, yield a scaling that follows that of T_{h1}, but overestimate them by roughly

50% which is somewhat expected from the dimensionality if the problem. On the other hand, the 3-D simulations are in excellent agreement either with the experimental results ($I = 10^{18}$ W/cm^2) as well as with the extrapolation of the data ($I = 3.7 \times 10^{18}$ W/cm^2).

Fitted into power laws of the parameter $I_{18}\,\lambda^2$ (I_{18} is the intensity in units of 10^{18} W/cm^2, and λ in μm), one can draw the following scalings for T_{h1} and T_{h2}:

$$T_{h1} \simeq 120\left(I_{18}\lambda^2\right)^{0.6} \quad \text{[keV]} \tag{4.7}$$

$$T_{h2} \simeq 300\left(I_{18}\lambda^2\right)^{0.2} \quad \text{[keV]} \tag{4.8}$$

Note that these scalings are relevant to the hot electrons that escaped the plasma within the *specularly* emitted jet.

In an earlier λ^3 experiment [12], Hou *et al.* inferred an effective electron temperature T_e from the slope of the bremsstrahlung spectrum (sampled between 20 and 100 keV), emitted from a Mo target. In the $10^{17} - 10^{18}$ W/cm^2 range, the effective temperatures scaled with the pulse energy E according to the following power law: $T_e \sim E^{\gamma}$ with $\gamma = 0.51 \pm 0.08$. Using the corresponding pulse duration and focal spot size, Hou's scaling can be translated into:

$$T_e \sim 18\,\left(I_{18}\,\lambda^2\right)^{0.5} \quad \text{[keV]}. \tag{4.9}$$

Although this scaling yields electron temperatures that are 5-6 times colder than those obtained through direct energy distribution measurements (this work) – a discrepancy expected from the bremsstrahlung cross-section (Eq. 2.34) – its dependence on intensity (power of 0.51 ± 0.08) agrees reasonably well the scaling in Eq. 4.7.

The scalings in Eqs. 4.7 and 4.8 suggest that the heating mechanisms dominant in the relativistic λ^3 regime cannot be described by the standard ponderomotive

potential acceleration proposed by Wilks [31]. Furthermore, these scalings are in disagreement with previous experimental results [81] obtained above the relativistic threshold. However, this disagreement is not all that surprising since the laser and plasma parameters in [81] are quite different than those in the λ^3 experiment. In order to explain our scalings, we resort to a simple theoretical model that examines the energy balance between in deposited laser intensity and the energy flux carried away by the hot electrons.

4.3.6 Electron heating model

One approach to analyze the dependence of electron temperature on laser intensity is to consider the power balance under the assumption that the absorbed fraction of incident intensity $\eta\, I$ equals the energy flux carried away by the hot electrons. In the case of a relativistic intensity laser and sub-relativistic hot electrons, this can be written as:

$$\eta\, I = \frac{1}{2}\, n_h\, m_e\, v_h^3. \tag{4.10}$$

Here the absorption coefficient η is assumed to be independent of the laser intensity in the range of interest (i.e. $10^{17} - 10^{18}$ W/cm^2). This is a reasonable assumption for oblique incidence laser and intermediate scale-length plasma [27].

Since the electrons are most likely to be heated around the critical surface, their density is assumed to be related to the relativistic critical density (Eq. 2.17):

$$n_h = \gamma\, n_{cr}. \tag{4.11}$$

Rewriting the intensity and n_{cr} in terms of the normalized vector potential a_0 (Eq. 2.10), Eq. 4.10 becomes:

$$\eta \, \frac{m_e^2 \, c \, \omega_L^2}{2 \, \mu_0 \, e^2} \, a_0^2 = \frac{1}{2} \left(1 + \frac{a_0^2}{2}\right)^{1/2} \frac{m_e \, \epsilon_0 \, \omega_L^2}{e^2} \, m_e \, v_h^3$$

$$\eta \, a_0^2 = \left(1 + \frac{a_0^2}{2}\right)^{1/2} \left(\frac{v_h}{c}\right)^3. \tag{4.12}$$

The sub-relativistic electron temperature T_h is related to the velocity v_h by the classical kinetic energy equation:

$$T_h = \frac{1}{2} \, m_e \, v_h^2. \tag{4.13}$$

Substituting v_h in Eq. 4.12 by its expression from Eq. 4.13, and solving for the temperature, one obtains:

$$T_h = \frac{1}{2} \, m_e \, c^2 \, \eta^{2/3} \left[\frac{a_0^2}{(1 + a_0^2/2)^{1/2}}\right]^{2/3} \tag{4.14}$$

$$= 255 \, \eta^{2/3} \left[\frac{a_0^2}{(1 + a_0^2/2)^{1/2}}\right]^{2/3} \quad \text{[in keV]},$$

or in terms of the $I \, \lambda^2$ parameter (in units of 10^{18} W/cm$^2 \mu$m^2):

$$T_h \simeq 207 \, \eta^{3/2} \left[\frac{I_{18} \, \lambda^2}{(1 + 0.36 \times I_{18} \, \lambda^2)^{1/2}}\right]^{2/3}. \tag{4.15}$$

The above equation predicts the hot electron temperature for a relativistic laser intensity and sub-relativistic electrons, as it is the case in the experiment described in section 4.3.3. Therefore, the temperatures T_{h1} can be fitted to Eq. 4.15 with the only free parameter being the absorption coefficient η. The fit is shown in Fig. 4.13 with $\eta = 0.52$. In fact, such an absorption fraction is in agreement with both simulations [27] and experiments having somewhat comparable parameters [29, 86, 87].

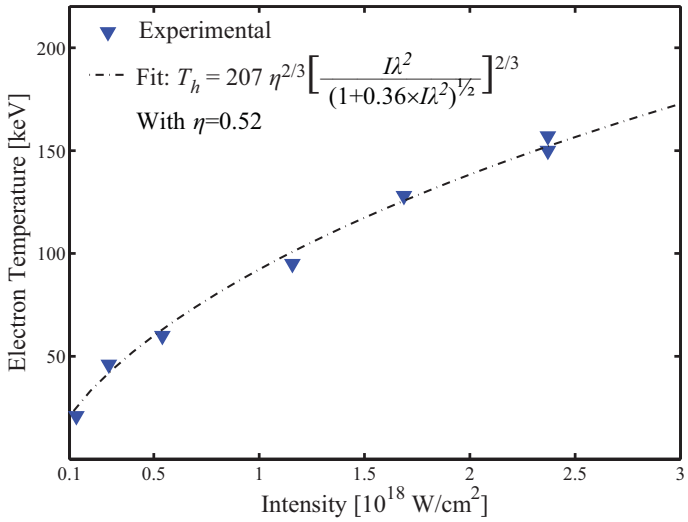

Figure 4.13: Hot electron temperature scaling with intensity fitted to the Eq. 4.15. The agreement between the experimental results and the model described in section 4.3.6 suggests that the absorption coefficient $\eta \simeq 0.52$

At the limit where the laser intensity is strongly relativistic ($a_0 \gg 1$), Eq. 4.14 is reduced to:

$$\begin{aligned} T_h &\simeq \frac{1}{2}\, m_e\, c^2\, \eta^{2/3}\, 2^{1/3}\, a_0^{2/3} \\ &\simeq 290\, \eta^{2/3}\, \left(I_{18}\, \lambda^2\right)^{1/3} \quad \text{[in keV]}. \end{aligned} \tag{4.16}$$

Incidently, this yields the same scaling obtained experimentally by Beg *et al.* [81] for an absorption fraction close to 65 %. This high absorption could be justified since in [81] both the pulse duration and the scale-length were longer than in the present experiment.

For sub-relativistic laser ($a_0^2 \ll 1$), Eq. 4.14 yields a yet different scaling:

$$\begin{aligned} T_h &\simeq \frac{1}{2}\, m_e\, c^2\, \eta^{2/3} a_0^{4/3} \\ &\simeq 207\, \eta^{2/3}\, \left(I_{18}\, \lambda^2\right)^{2/3} \quad \text{[in keV]}. \end{aligned} \tag{4.17}$$

A very similar scaling, $T_h \sim \left(I\,\lambda^2\right)^{0.7\pm0.1}$ with $T_h = 11$ keV at 2×10^{16} W/cm^2,

was experimentally obtained by Zhavoronkov *et al.* [82] in the intensity range $10^{16} - 10^{17}$ W/cm^2. In these experiments, the inferred electron temperatures constitute a good fit for Eq. 4.17 albeit with an absorption coefficient $\eta = 0.93$. Such an unphysically high absorption fraction suggests that the simple scaling argument derived from Eq. 4.10, under the assumption that η is independent of the laser intensity I, does not hold for subrelativistic intensities. This is not surprising since simulations [27] show that, while the absorption fraction depends weakly on intensities for $I > 10^{17}$ W/cm^2, this dependence becomes far more pronounced in the $10^{16} - 10^{17}$ W/cm^2 range.

4.4 Discussion

Studying the scaling of the electron temperature could be useful to infer the nature of the absorption mechanisms that dominate the interaction. As previously discussed in section 2.3, most standard heating models yield a scaling of the form:

$$T_h = \alpha \left(I\,\lambda^2\right)^{\gamma}, \tag{4.18}$$

where $\gamma = 1/3$ in the case of resonance absorption, $\gamma = 1/2$ for $\boldsymbol{j} \times \boldsymbol{B}$ heating, and $\gamma = 1$ for the Brunel mechanism. Experimentally, Beg *et al.* [81] measured the following scaling:

$$T_h = 100 \left(\frac{I\,\lambda^2}{10^{17}}\right)^{1/3} \quad \text{[keV]}, \tag{4.19}$$

in the intensity range of $10^{18} - 10^{19}$ W/cm^2. As expected, this indicates a strong contribution from resonance absorption due to the relatively long duration (1 ps) and low contrast (10^{-6}) of the p-polarized obliquely incident pulses. More recently, Zhavoronkov *et al.* obtained the scaling $T_h \sim (I\,\lambda^2)^{0.7}$ between $10^{16} - 10^{17}$ W/cm^2 for 45 fs pulses and a prepulse contrast of 10^7. This scaling is somewhat similar to

the scaling of T_{h1} as the laser pulse duration and contrast ratio were comparable.

Such scalings ($\gamma = 0.6 - 0.7$) are not characteristic of any of the standard heating mechanisms (section 2.3). More physical models should include the interaction of the electron beam with the quasi-static fields that modulate the plasma corona at high intensities. Indeed, this picture is reinforced by the spatial distribution measurements that show the presence of one electron group emitted close to the specular direction and a separate group closer to the target surface. The first group, whose temperature is studied in the present section, may be influenced by a quasi-static magnetic channel along a direction close to the laser specular direction [88]. The second group is likely to be confined to a surface layer by a self-sustained surface field structure [89].

4.5 Effects of plasma scale-length on spatial and energy distribution of hot electrons

In this section we investigate the effect of plasma scale length on the emission characteristics of hot electrons from an SiO_2 target.

4.5.1 Variable-delay prepulse and scale-length control

A configurable femtosecond prepulse with an intensity of 2×10^{14} W/cm^2 was installed to control the SiO_2 plasma scale-length at the arrival time of the main pulse (see Fig. 4.7). Again, we ran a one-dimensional HYADES simulation to relate the prepulse delay in ps to scale-length in μm. Since the ASE pedestal, as measured by the third-order autocorrelation (section 4.2.1), was below the SiO_2 damage threshold up until the last 10 ps preceding the main pulse, it was safe to neglect its contribution and only consider the intentional femtosecond prepulse.

Given the large prepulse focal spot (30 μm FWHM), a one-dimensional simulation was adequate to describe the interaction. We used the equations of state (Sesame

table 24) to describe the SiO_2 target and the average-atom model to simulate its ionization. The energy was deposited by a p-polarized, 30 fs *laser* source with a 45° incidence angle. At 100 fs after the prepulse, the plasma reached a temperature of ~ 20 eV with an effective charge state $Z^* \simeq 3$.

Assuming a free isothermal plasma expansion, the critical surface will launch at the ion sound velocity given by:

$$c_s = \sqrt{\frac{Z^* k T_e}{m_i}} \tag{4.20}$$

$$= 9.79 \times 10^5 \sqrt{\frac{Z^* T_e}{\mu}} \quad [\text{cm/sec}]. \tag{4.21}$$

Thus, the scale-length at the time of arrival of the main pulse can be inferred from the time delay t_d:

$$L_n = c_s t_d$$

$$= 1.6 \times 10^{-2} t_d \quad [\mu\text{m}]. \tag{4.22}$$

4.5.2 Spatial distribution and scale-length

The spatial distribution of the hot electrons from SiO_2 was studied as a function of a prepulse delay for a laser incident at 45° with an intensity of $\sim 2 \times 10^{18}$ W/cm^2. The pre-delay δt was varied between 0 and 100 ps, corresponding to a scale-length shorter than 0.1λ when no prepulse is present and 2λ at the maximum delay. The electron jet was imaged on a Lanex phosphor screen mounted in a configuration similar to the one in Fig. 4.7. A 50 μm-thick Cu foil was used to block the laser light from reaching the Lanex and filter out electrons with lower than 150 keV energy. The back surface of the phosphore was imaged onto a CCD camera through a Schott Glass BG-39 glass filter to suppress the scattered laser light.

Figure 4.14(a) shows a set of single-shot-exposure Lanex images taken at different

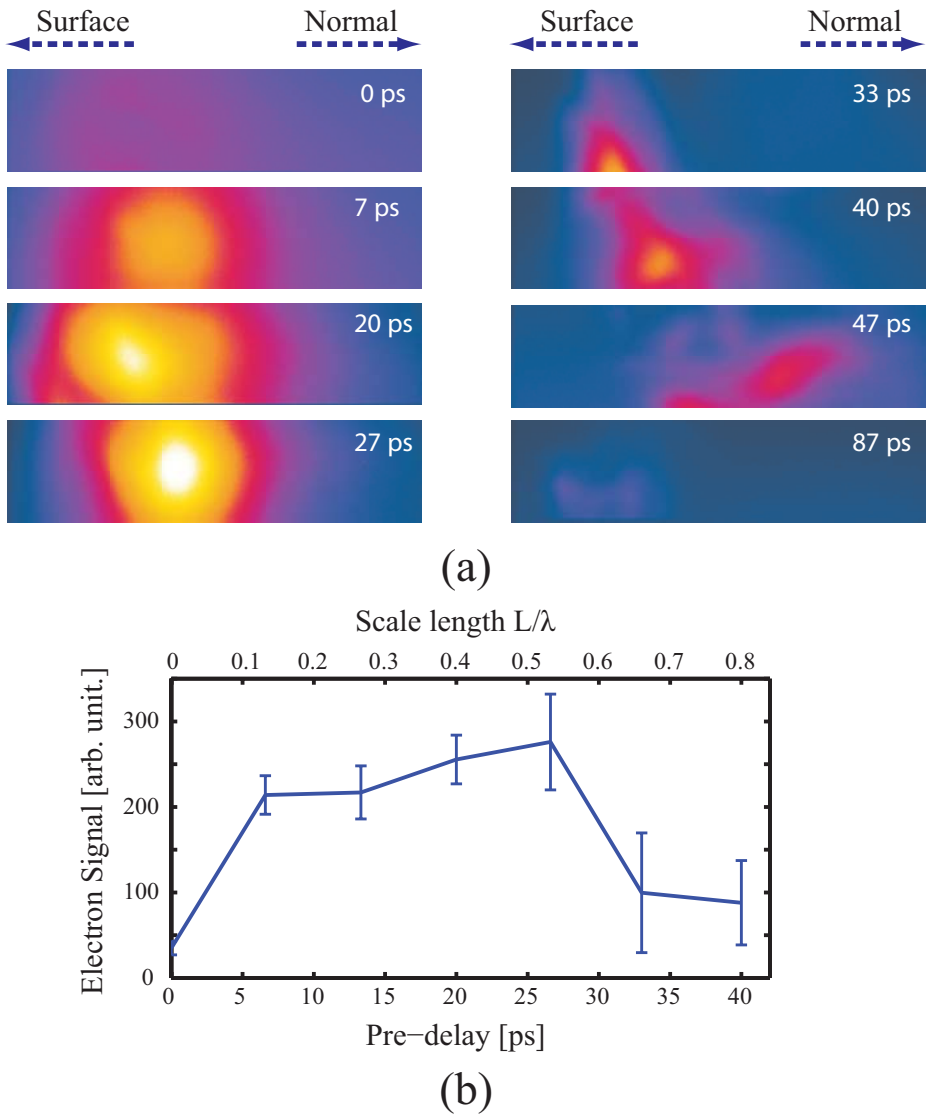

Figure 4.14: Single-shot spatial distribution of the electron jet recorded on a LANEX screen for various prepulse delays (a). The integrated electron signal for electrons exceeding 150 keV (50 μm Cu filter) plotted as a function of the prepulse delay and preplasma scale-length.

prepulse delays. All images are displayed using the same colormap and normalized to the peak of the most intense beam (for $\delta t = 27$ ps). Each Lanex slide covers an angle of approximately 45° in the incidence plane, between the target surface (left edge) and normal (right edge). For short scale-lengths ($L_n \leqslant \lambda/2$), the electrons are emitted in a narrow Gaussian-like beam between the specular and the normal directions. On the other hand, for $L_n \geqslant \lambda/2$, the electron jet loses its beam-like behavior and is emitted within a broader cone as it was the case for the Al-plasma

electrons (section 4.3.2).

The integrated electron signal on the Lanex screen is plotted as a function of the prepulse delay (or plasma scale-length) in Fig. 4.14(b). As L_n increases, the total electron signal increases and reaches a peak around $L_n = \lambda/2$. However, when L_n exceeds $\lambda/2$, the signal drops considerably and becomes less reproducible. This is evident from the relative size of the statistical error bars, obtained by averaging 3-4 images at each pre-delay.

4.5.3 Energy distribution and scale-length

In order to understand the effect of plasma scale-length on the hot electron temperature we measured the energy distribution for two different preplasma conditions: In the first case, the intentional prepulse was blocked yielding an expected scale-length – due solely to the ASE pedestal – shorter than 0.1λ. In the second case, the prepulse delay was set to 27 ps resulting in $\sim 0.5\lambda$ scale-length. Both measurements were taken by accumulating 250 p-polarized pulses, incident at 45°, with a peak intensity of $1.9 \times\ 10^{18}$ W/cm^2. Additionally, single-shot spatial distribution measurements, similar to those described in section 4.5.2, were recorded on imaging plates for improved sensitivity and dynamic range. These results are compiled in Fig. 4.15.

The single-shot spatial distributions recorded on imaging plates showed identical characteristics to those recorded on Lanex screens. The imaging plates were shielded with Cu and Al foils with respective thicknesses of 50 and 25 μm which stops electrons with lower than $\sim$ 300 keV energy. For a prepulse delay $\delta t \leqslant 30$ ps (or when no prepulse is present) the hot electrons were emitted in a well defined beam with a divergence of 22° at the half maximum isocontour.

The electron beam emission angle varied between 35° for the no-prepulse case to 32° for a delay of $\delta t = 30$ ps. This corresponds to a deviation from the laser specular

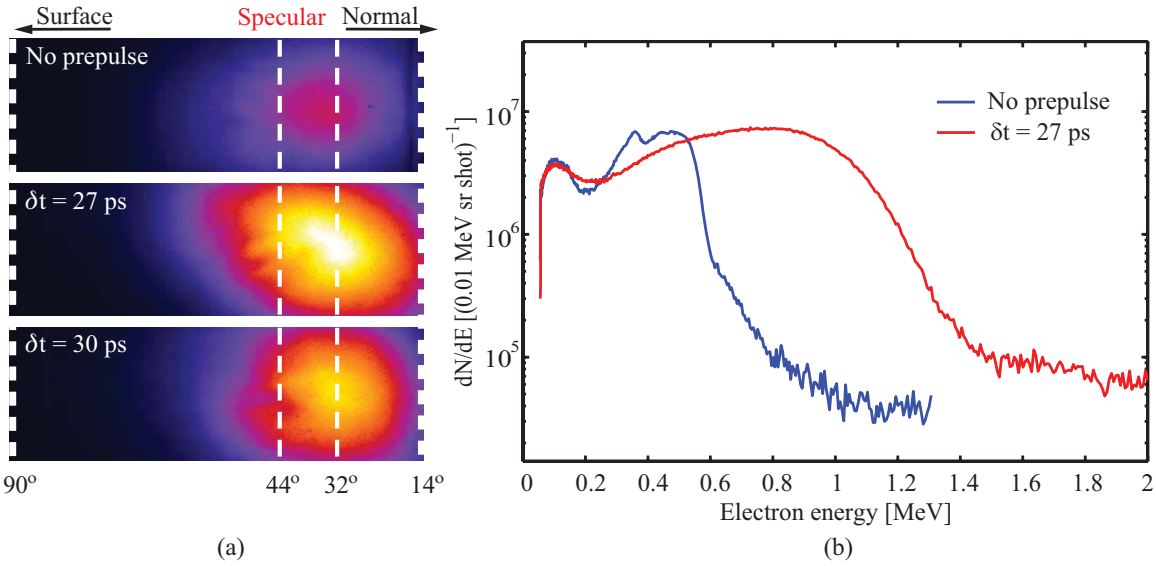

Figure 4.15: (a) Hot electron spatial distributions from an SiO_2 plasma, for a laser incident at 44° with an intensity of 2×10^{18}W/cm^2, measured for three different prepulse delays: No intentional pre-pulse, 27 ps and 30 ps pre-delay (from top to bottom). (b) Electron energy distributions measured along the $\phi = 36°$ direction for the no prepulse case (blue) and the $\delta t = 27$ ps (red).

direction by up to 12° toward the target normal. Such a deviation in emission angle has been observed in both simulations and experiments [90, 91].

The integrated electron beam signal at $\delta t = 27$ ps increased by a factor of 5-6 folds compared to the case when no intentional prepulse was introduced, in agreement to the results obtained with the Lanex screen (see Fig. 4.14(b)).

The energy distributions for the no-prepulse case (blue) and $\delta t = 27$ ps (red) are shown in Fig. 4.15(b). Both measurements were 250-shot averages collected along the $\phi = 36°$ from the normal (4° off the measured electron beam peak toward the specular direction). Two important observations were made. First, unlike the case of Al plasma, the energy distribution cannot be explained with Maxwellian-like distributions. In fact, for both pre-plasma conditions, the energy spectra showed the presence of a high-energy peak, somewhat reminiscent of a quasi-monoenergetic distribution overlaying the usual Maxwellian-like distribution (as in the case with Al target). In a second observation, the peak of the *quasi-monoenergetic* component substantially shifted toward higher energies when the prepulse delay was $\delta t = 26$ ps,

whereas the low energy component of the distribution ($50-200$ keV) was unaffected.

Quantitatively, the peak of the high-energy structure occurred around 450 keV when no intentional prepulse was present, and 780 keV for the optimum delay of 26 ps. A consequence of non-Maxwellian distributions was that the electron temperature T_h, as defined in Eq. 2.36, was no longer applicable. Alternately, the distributions were characterized by the average electron energy:

$$\langle E \rangle = \frac{\sum_i E_i \, f_i(E_i) \, \Delta E_i}{\sum_i f_i(E_i) \, \Delta E_i}, \tag{4.23}$$

where the summations are carried out for all i such that $E_i > 50$ keV. For the no-prepulse case we obtained $\langle E_0 \rangle = 370$ keV, while for the 27-ps prepulse case $\langle E_p \rangle = 675$ keV. Moreover, the energy conversion efficiency η_e of the 800 nm laser to the hot electron beam escaping the plasma was calculated assuming the above described spectra reflects the energy distribution within a cone divergence of $\pm 10^\circ$ around the beam center. We obtained $\eta_e = 0.9 \times 10^{-3}$ when no prepulse was present, and $\eta_e = 3.9 \times 10^{-3}$ for the 27 ps prepulse. Note that η_e is the fraction of laser energy carried away by hot electrons escaping the plasma, not to be confused with the conversion efficiency into all hot electrons expected to be of the order of 10% [66].

4.5.4 Discussion

The observation of narrow hot electron beams produced by p-polarized intense laser pulses has been reported by several groups [87, 92, 91]. The emission direction and

	No prepulse	27 ps
Scale-length	$< \lambda/10$	$\lambda/2$
Peak energy	450 keV	780 keV
$\langle E \rangle$	370 keV	675 keV
η_e	0.9×10^{-3}	3.9×10^{-3}

Table 4.1: Summary of the electron measurements for 2 different plasma scale-lengths. $\langle E \rangle$ and η_h are the average electron energy and conversion efficiency into the escaped electrons, respectively.

temperature of these beams depends critically on the plasma scale-length [93]. For instance, at an optimum scale-length of $\lambda/2$, Bastiani *et al.* found that as much as 0.7 % of the laser energy – incident on an SiO_2 target – is carried away in the electron beam (compared to 0.4 % in our experiment). In most cases, and at near-relativistic intensities, these energetic beams are emitted at an angle between the laser specular and the normal direction [94, 95, 96, 97]. According to simulations [88], the hot electrons are pinched and guided by the quasi-static magnetic field, along a direction that could be estimated by considering the momentum conservation equations involving the laser and electron beam. For strongly relativistic laser intensity, the emission direction is closer to the specular. On the other hand, for sub-relativistic intensities, the jet is emitted closer to normal direction. Simulations suggests that a low density corona is crucial to the formation of static magnetic field and the formation of jets.

To the best of our knowledge, none of the referenced experimental results investigated the electron energy distribution within the collimated jet. This is primarily due to the fact that most experiments rely on the spectrum of the bremsstrahlung emission to extract the electron temperature of an assumed Maxwellian-like distribution. While this assumption may be justified for background electrons emitted over a broad angular spread, as it is the case with the Al target experiments (section 4.3.3), the results described in the present section show that, along the direction of the electron jet, the energy distribution exhibits a high-energy spectral structure and cannot be described by a multi-temperature Maxwellian distributions (Fig. 4.15). Moreover, the scale-length dependence of the peak energy of this *hot group* suggests that the jet electrons may be accelerated in the corona by the quasi-static fields. Additional experiments as well as simulations are still necessary to elucidate the nature of the mechanisms yielding the energetic beams.

Finally, it is worth noting that this is the first time relativistic electron jets are

produced at the kilohertz repetition rate from a laser-plasma interaction. Those electron beams could be useful for applications such as radiography or electron diffraction experiments.

4.6 Hot electrons from a grazing incidence laser

Recent publications [98, 89, 99, 97] have reported the observation of hot electron currents along the surface of a solid target when the laser incidence angle is larger than a certain critical value. According to this picture, forward-propagating hot electrons could be confined to a surface layer due to a self-sustained coupling between the quasi-static magnetic fields that draw the electrons back toward the vacuum, and the repelling sheath electrostatic fields [89]. This could be important to guide and focus hot electron beams for high-energy applications such as the fast ignition scheme (ICF) [71, 72].

It is believed that, in the λ^3 regime, the high numerical aperture focusing gives rise to steep transverse density gradients, which could alter the conditions necessary for the propagation of the surface beams. Therefore, we conducted a series of experiments aimed to investigate the spatial and energy distributions of hot electrons generated by a grazing incident laser in the λ^3 regime.

4.6.1 Al plasma

In a first experiment p-polarized pulses are focused on an Al target with an incidence angle of 65°. At the intensity of 2×10^{18} W/cm^2, the ASE pedestal generates a pre-plasma with an estimated scale-length of $\lambda/2$.

Figure 4.16 shows the spatial distribution recorded on a stack of 2 back-to-back imaging plates. For electrons higher than ~ 55 keV (25 μm Al filter, IP layer (a)) the electron signal peaked along the target surface. However, highly energetic electrons (> 400 keV on the back IP layer (b)) were emitted in *beamlets* scattered throughout

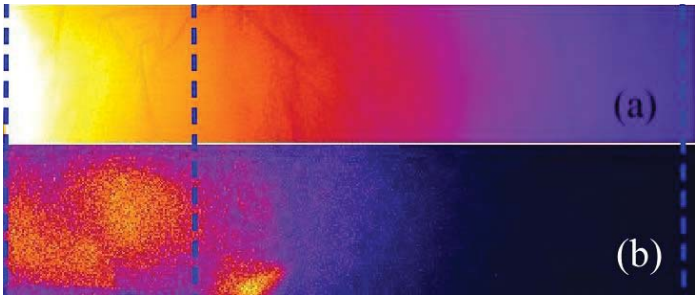

Figure 4.16: Electron spatial distribution from Al target for p-polarized pulses at 1×10^{18}W/cm^2 incident at 65° for a 25 μm Al filter (a), and a back IP layer (b). The vertical lines from left to right mark the surface, specular and normal directions.

the laser specular cone. Energy distribution measurements, taken by accumulating 500 laser shots along the 65° and the 85° directions, confirmed that the high-energy side of the spectrum ($E > 600$ keV) varies a little over a broad emission angle (Fig. 4.17). This suggests that the surface electron peak in Fig. 4.16(a) is mostly due to low energy electrons.

As in the case of 45° incidence, the energy distributions in Fig. 4.17 were fitted to two-temperature Maxwellians. For a laser intensity of 2.1×10^{18} W/cm^2 we obtained $T_{h1} = 164$ keV, $T_{h2} = 520$ keV along the specular direction, and $T_{h1} = 158$ keV, $T_{h2} = 533$ keV along the 85° direction. Although along both directions the T_{h1} component agreed reasonably well with the scaling in Eq. 4.7, the T_{h2} component was almost twice as hot compared to the scaling in Eq. 4.8, with maximum detected energies exceeding 1.4 MeV.

4.6.2 SiO_2 plasma

A similar experiment was repeated for an SiO_2 target mounted at an angle of 67° with respect to the laser axis. Due to the higher damage threshold for dielectric material, the ASE pedestal was expected to yield a steep electron density profile ($L_n < \lambda/10$).

The spatial distribution was recorded, in the single-shot mode, on a strip of imaging plate that was shielded with Al and Cu filters, with nominal thickness of 25

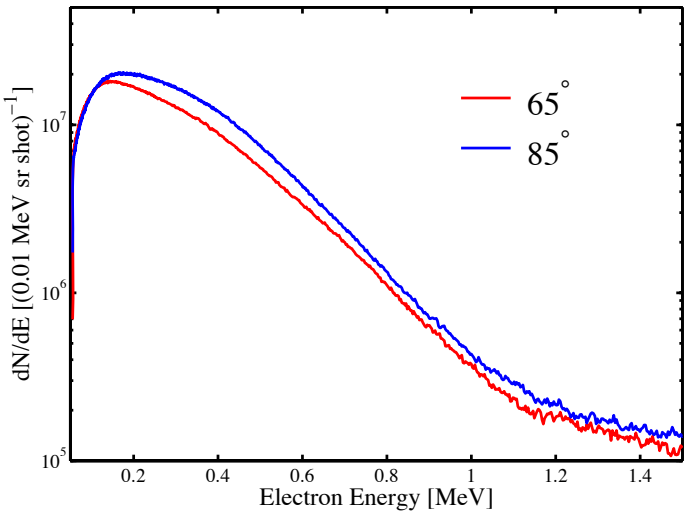

Figure 4.17: Electron energy distribution for a laser incident at 65° with an intensity of 2.1×10^{18}W/cm^2, observed along specular (red) and the surface (blue) directions.

μm and 50 μm, respectively. At the intensity of 1.9×10^{18}W/cm^2, electrons higher than 200 keV were emitted in a Gaussian-like beam along the $\phi = 48°$ with respect to the target normal (see Fig. 4.18(a)). The beam divergence at the half-intensity contour was calculated to be 26°. For reference, the hard edge of the laser specular cone is depicted in a dashed ellipsoid (red). This measurement suggests that, in the case of the SiO_2 target, and with a short plasma scale-length, there was no evidence of surface electron beams.

Additionally, the energy distribution (see Fig. 4.18(b)) was measured along the electron beam direction (solid line), and the laser specular direction (dashed line) by accumulating 250 laser shots. Both distributions exhibited two distinct spectral peaks as it was the case for 45° incidence laser on SiO_2. This double-peaked spectrum made it impossible to model the distribution by the usual Maxwellian and therefore, the spectra were characterized by their average energy $\langle E \rangle$. Along the beam direction we measured $\langle E^{48°} \rangle = 443$ keV whereas along the specular direction $\langle E^{67°} \rangle = 235$ keV.

Figure 4.19 shows the energy distribution measured along the electron beam direction for a laser intensity of 3.3×10^{17}W/cm^2 (blue curve). For comparison, the

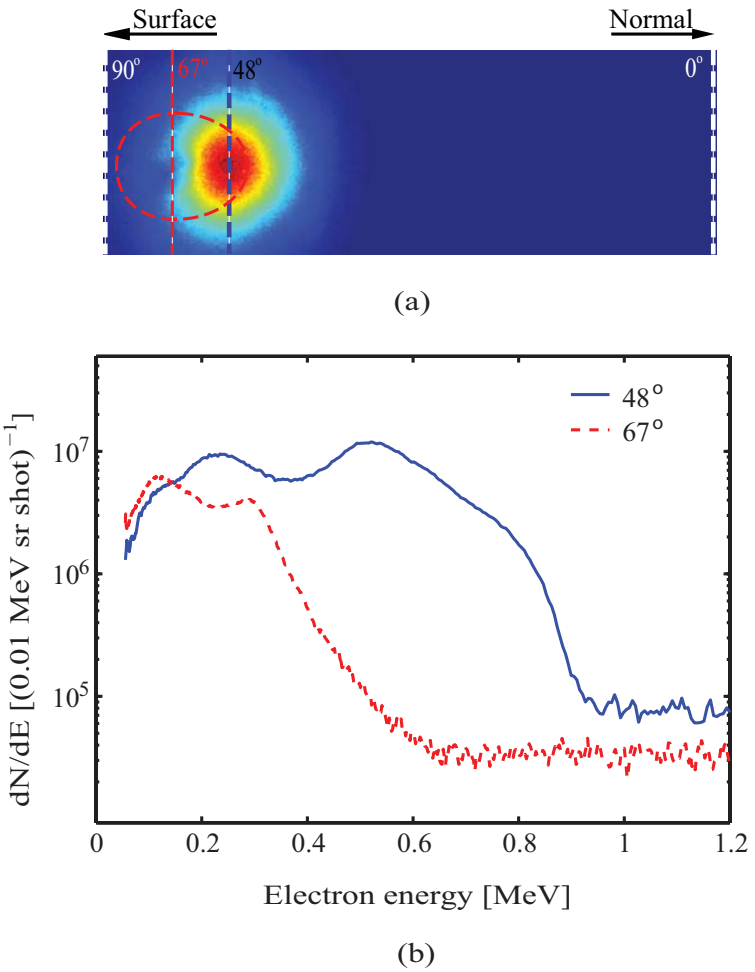

Figure 4.18: (a) Spatial distribution of electrons higher than 200 keV from an SiO_2 target for a laser incidence angle of 67° and an intensity of 2×10^{18}W/cm^2. The dashed vertical lines mark the target surface, the laser specular direction, the electron beam direction and the target normal, respectively from left to right. The laser specular cone, centered at 67° is marked with a dashed ellipse for reference. (b) Electron energy distribution measured along the electron beam direction (blue) and the laser specular direction (red).

relativistic intensity spectrum along the same direction (from Fig. 4.18(b)) is plotted on the same graph. Evidently, in the sub-relativistic case, the spectrum recovered a Maxwellian-like distribution with a temperature $T_h = 26$ keV. This suggests that the heating mechanisms responsible for the generation of the relativistic second peak, are predominant at relativistic intensities.

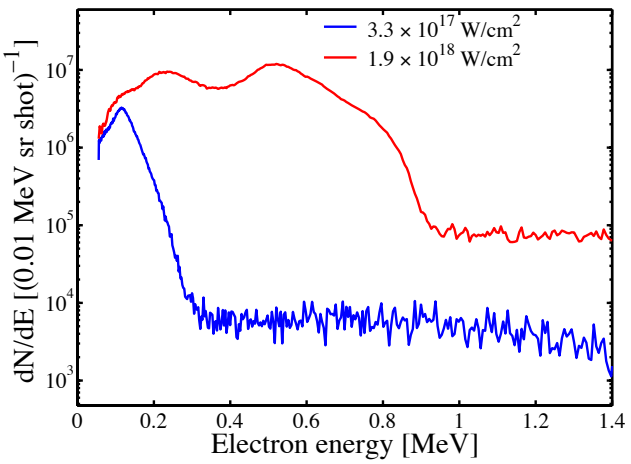

Figure 4.19: Electron energy distribution from a bulk SiO_2 target for a laser incident at 67° with a peak intensity $I_p = 3.3 \times 10^{17} W/cm^2$ (blue) and $1.9 \times 10^{18} W/cm^2$ (red). The spectra were measured along the direction of the electron beam emission.

4.7 Conclusion

We have studied the spatial and energy distribution of hot electrons generated from the interaction of a relativistic intensity laser with a solid density plasmas. In the case of an Al plasma with an estimated $\lambda/3$ scale-length, the spatial distribution had one peak close to the laser specular direction and another close to the target surface. This suggests the existence of multiple heating and guiding mechanisms driven by quasi-static electric and magnetic fields in the corona. The temperature of the specularly emitted hot electrons scaled like $(I\,\lambda)^{0.6}$, a scaling that had not been observed previously at relativistic intensities. However, it is important to note that this scaling was obtained by averaging $\sim 10^3$ laser shots, compared to previously published scalings that relied on single-shot measurements. Moreover, the experimental temperatures agree well with a scaling argument based on energy conservation – and thus independent of the absorption mechanisms – which relates the electron distribution to the momentum transferred by the laser pulse to the electrons. According to this simple model, about 52% of the laser energy is coupled to the hot electrons.

The interaction with the SiO_2 plasma yielded a qualitatively different energy

distribution functions. Unlike all published experimental and simulation results that we are aware of, the energy distribution showed a high-energy *quasi-monoenergetic* group that overlayed the usual Maxwellian-like distribution. The peak energy of this group was sensitive to the plasma scale-length and reached a maximum for $L_n \simeq \lambda/2$. This suggests that the underlying electron acceleration mechanism is driven by fields set by the laser in the underdense plasma. The relativistic energy jet emitted at this optimum scale-length carried about 0.4% of the incident laser energy and was well collimated which could be useful for applications such as electron diffraction and radiography.

CHAPTER V

HARD X-RAY GENERATION USING ULTRA-FAST FIBER LASERS

5.1 Introduction

5.1.1 Motivation

Ultrafast x-ray sources have enabled the study of atomic and molecular structural dynamics down to a spatial resolution comparable with the atomic dimensions and with a sub-picosecond temporal resolution. Although synchrotron-based sources have been prevalent due to their high brightness, laser-produced x-ray sources have proven their usefulness in a variety of applications ranging from solid-state physics [37] to the biological sciences [39]. Furthermore, due to their point-like nature, laser-produced sources could achieve imaging resolutions unattainable with conventional x-ray tubes, extending their usefulness to medical and industrial radiography and more recently phase contrast imaging [70].

The total x-ray yield from laser-driven sources, however, is limited by the power of the driving laser which is typically a titanium-sapphire system with under 10 watts of average power. This could be disadvantageous and even impractical especially for applications that require x-ray imaging in transmission through thick and dense objects. On the other hand, the emergence of high-power, pulsed fiber laser technology based on large mode area (LMA) fibers [100] has revealed a new path toward the realization of high brightness, practical laser-produced plasma

sources of short wavelength radiation.

5.1.2 Yb-doped fiber lasers

Rare-earth-doped fiber lasers were perceived as an alternative technology suitable for compact and monolithic architectures. However, the emergence of large mode area (LMA) fibers in recent years has distinguished them with unique properties, that enable high-energy, kilowatts-average-power output in diffraction-limited beams.

Inherently, fiber lasers possess superior thermal management properties compared to conventional bulk lasers. This is partially due to the large surface-to-volume ratio – prevalent in fiber geometries – which permits effective heat dissipation. Moreover, certain rare-earth dopants are characterized with a very high optical-to-optical efficiency (around 80% in Yb-doped fibers) which reduces the thermal load due to the residual pump light. Both these factors have enabled the demonstration of 3 kW in continuous-wave, near-diffraction-limited beams [14] with the potential to exceed 10 kW in the near future.

In pulsed mode, however, conventional single-mode fibers – typically with sub-10 μm core diameter – are strongly susceptible to damage and accumulated nonlinearities. For nanosecond pulses, this limits the pulse energy to a few microjoules in the case of fused silica fibers. In order to attain higher pulse energies, scaling of the mode area is necessary at the expense of the beam mode quality. However, it turned out that even highly multi-mode LMA fibers can produce an effectively single-mode output, either by coiling the fiber to filter out higher order modes [101] or by meticulously exciting the fundamental mode [102]. These LMA fibers are capable of supporting higher than MW peak-power pulses in diffraction-limited beams compatible with high average power and MHz repetition rate operation [103, 104].

5.1.3 From the λ^3 regime to fiber lasers

In chapter III we discussed the generation of hard x rays using a relativistic intensity laser, in the λ^3 regime. In this regime, compressed pulses with ~ 30 fs duration, 1 mJ energy are tightly focused to the diffraction-limit in order to attain intensities greater than 10^{18} W/cm^2. However, it was found [12] that, for sub-picosecond laser pulses, the x-ray yield is weakly dependent on the pulse duration (see section 3.4.2). Thus, it is possible to relax the pulse duration constraint to several hundred femtoseconds and still achieve a high x-ray conversion efficiency at intermediate intensities $\sim 10^{16}$ W/cm^2. Noting that state-of-the-art ultrafast fiber lasers can be pushed to deliver millijoule-level pulses [13, 57], the intermediate intensity regimes could be accessible if λ^3 focusing techniques were employed.

In the present chapter, we report on a pioneering demonstration of a hard x-ray source using a fiber chirped-pulse amplification (CPA) system. At the time of this experiment millijoule-level pulses were not available, and high conversion efficiencies into the K_α line ($10^{-5} - 10^{-4}$) were out of reach. However, sub-millijoule, 300 fs pulses were tightly focused close to the diffraction-limit on a Ni target. The x-ray conversion efficiency was comparable to those obtained with similar pulse-energy, conventional solid-state lasers.

5.2 Fiber CPA laser system

The x-ray source driving laser is a 1 μm fiber CPA (FCPA) system utilizing high-efficiency ytterbium- (Yb) doped fiber amplifiers. In order to extract up to millijoule energies with minimal nonlinear effects, namely self-phase modulation (SPM), the oscillator pulses were stretched to nanosecond duration and launched into a series of very-large-mode-area (VLMA) fiber amplifiers. This section provides a comprehensive description of the system (Fig. 5.1) also described in [17, 57].

At the front end of the system is a solid-state mode-locked commercial oscillator

(High Q Laser) providing 1.8 nJ, 100 fs transform-limited pulses centered at 1064 nm with a repetition rate of 72 MHz. The pulses are then stretched to a duration of ~ 1 ns using a high-dispersive grating (1800 line/mm) stretcher. The stretcher was not designed to transmit the total spectrum of the seed pulses (11 nm FWHM) but rather to clip a 10 nm bandwidth centered at 1064 nm. This eliminates the wings in the spectrum and yields, in the time domain, a pulse with a fast rising and falling edges, thus maximizing energy extraction in the amplifiers. Additionally, clipping the spectral width alleviates gain narrowing and frequency pulling effects due to the tilted gain profile at 1064 nm in the Yb amplifying chain. The repetition rate of the oscillator pulses was reduced to 1 kHz using a Pockels cell with 13 ns window and 10^5 extinction ratio, installed at the output of the stretcher.

The stretched pulses are then coupled into a four-stage fiber amplifying chain consisting of two single-mode (SM) fiber preamplifiers, a 30 μm-core large mode-area (LMA) fiber amplifier, and finally a 65 μm-core VLMA fiber amplifier. Both SM preamplifiers use 3 m single clad, core pumped, highly doped Yb fibers which are pumped at 974 nm. The first preamplifier uses a counter-propagating pumping scheme that increases the gain, while the second uses a co-propagating configuration in order to prevent energy damage to the wavelength-division-multiplexer (WDM) and eliminate unnecessary propagation in passive fiber after the gain fiber. This reduces the effective propagation length in the single-mode fiber, thus minimizing undesirable nonlinear effects. The two preamplifiers are separated by an inline isolator and an acousto-optic modulator (AOM) with a 70 ns rise time to prevent damaging feedback and crosstalk. After the second preamplifier, the pulse energy reaches 500 nJ .

Subsequently, the preamplified pulses are injected into a 30 μm-core, 250 μm-clad, Yb-doped, polarization maintaining (PM) fiber with core and cladding numerical apertures of 0.062 and 0.47, respectively. Due to its multimode nature, this fiber

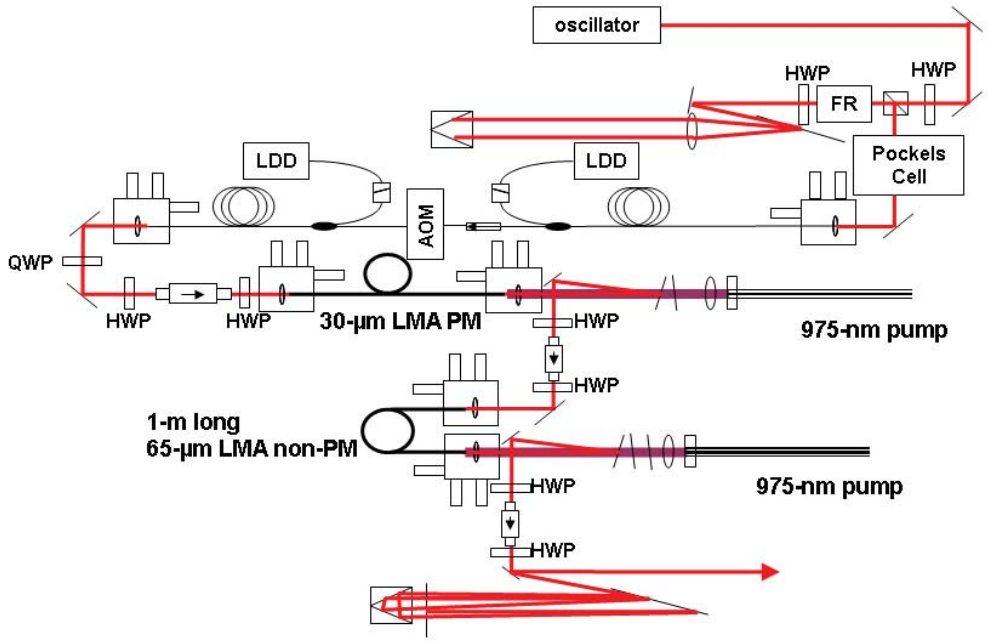

Figure 5.1: Schematic of the fiber CPA system used for x-ray generation. It consists of 2 single-mode preamplifiers, a 30 μm-core LMA stage, and a 65 μm-core VLMA amplifier. Fiber coiling and single mode excitation are used to achieve a diffraction limited beam at the output.

supports a large number of modes with different group velocities in the core. After compression, this could produces a pulse train instead of a single pulse. To avoid this, it is necessary to excite a single mode into all multimode fibers used in the system. The fundamental mode operation is achieved by coiling the 3 m long fiber along an 8 cm diameter disk to filter out unwanted higher order modes. At both ends of the fiber, 4 mm long coreless protective end-caps are used for two functions: first, they prevent surface damage at high energies. Second their 12° tilted surfaces help reduce feedback from Fresnel reflection. This fiber is also pumped at 975 nm in the counter-propagating configuration with free-space coupling arrangement. The pulse energy reaches 11 μJ at the output of this amplifier stage.

Finally, the last amplifier stage is a non-polarization-maintaining 30 μm-core, 250 μm-clad VLMA fiber with numerical apertures of 0.062 and 0.47 for the core and cladding, respectively. As in the case of the 30 μm-core fiber, the single mode excitation technique was used to obtain diffraction-limited beam at the output.

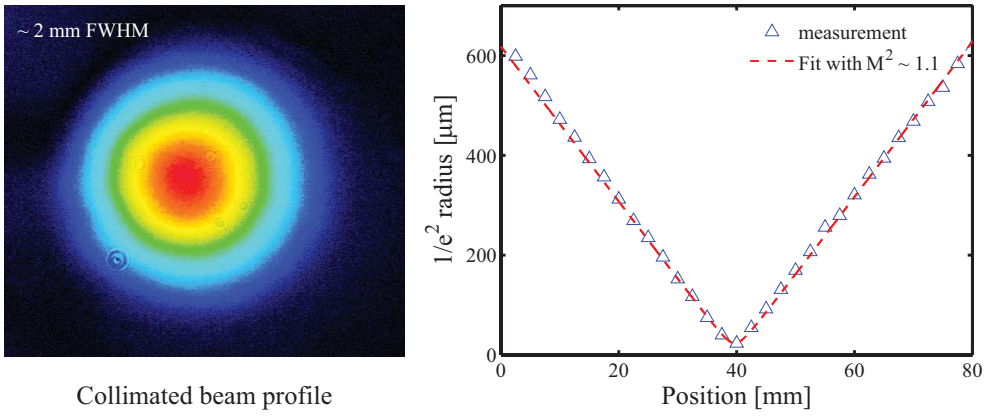

Collimated beam profile

(a) (b)

Figure 5.2: (a) Beam profile of the collimated output of the 65 μm-core VLMA fiber measured with a CCD camera. (b) The beam quality was characterized by measuring the spot diameter around the focus of a 75 mm lens using the knife-edge technique. The M^2 parameter was found to be ~ 1.1.

However, this excitation is achieved by precise mode matching between the 30 μm-core and 65 μm-core fibers using a lens telescope. Although the 65 μm-core fiber is highly multimode, fundamental LP_{01} mode operation is stable and robust once achieved (see Fig. 5.2(a)). Mechanically, care has to be taken to ensure that both ends of the fiber were mounted with minimal amount of stress and that there was no unnecessary fiber bending and twisting. The energy at the output of the amplifier is ~ 120 μJ and 65 μJ after the grating compressor.

The quality of the beam at the output of the system was quantified by measuring its diameter as it goes through the focus of a 75 mm lens, using the knife-edge technique (see Fig. 5.2(b)). The $1/e^2$ radius $\omega(z)$ was then calculated and fitted to the expanded-Gaussian beam radius given by:

$$\omega(z) = \omega_0 \left[1 + \left(\frac{(z - z_0)\ \lambda_0\, M^2}{\pi\, \omega_0^2} \right)^2 \right]^{1/2}, \tag{5.1}$$

where Z_0 is the coordinate of the minimum beam beam waist ω_0. The quality parameter M^2 was found to be ~ 1.1.

The temporal profile of the amplified pulses was characterized using the second

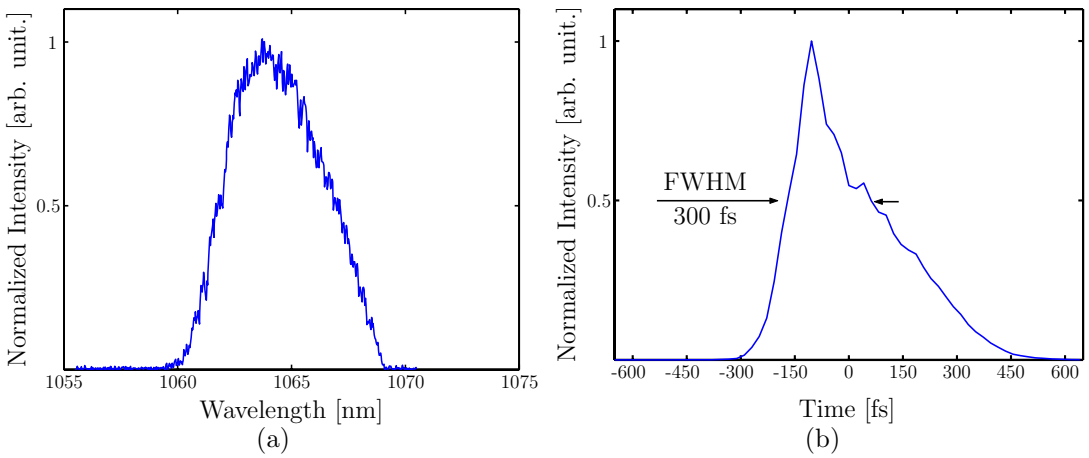

Figure 5.3: The FCPA compressed pulses, with a bandwidth of ~ 5 nm (a), were characterized using the FROG technique. The reconstructed pulse duration is about 300 fs (b).

harmonic frequency-resolved optical gating (FROG) technique according to which the duration was ~ 300 fs. Fig. 5.3 shows the measured spectral and reconstructed temporal profiles. Additionally, measurements using an InGaAs fast photodiode showed that the contrast ratio between the main pulse and the oscilaltor prepulses leaking throughout the rising edge of the electro-optic modulator (arriving at 13.8 ns intervals prior to the main pulse) is better than 3×10^{-5}.

5.3 Fiber CPA driven x-ray source

5.3.1 Experimental setup

The x-ray generation experimental set-up is depicted in Fig. 5.4. The compressed p-polarized pulses, incident at 45°, are focused on a Nickel (Ni) slab target using an $f/1.2$, 60° off-axis, paraboloidal mirror. The spot size obtained with such a large numerical aperture focusing is characterized with strong abberations spreading a substantial fraction of the pulse energy beyond the diffraction-limited diameter. These aberrations are reduced by using a 37-actuator deformable mirror controlled by a genetic learning algorithm. The genetic algorithm acquires the second harmonic green signal generated by imaging the focal spot on a BBO crystal with a 60×

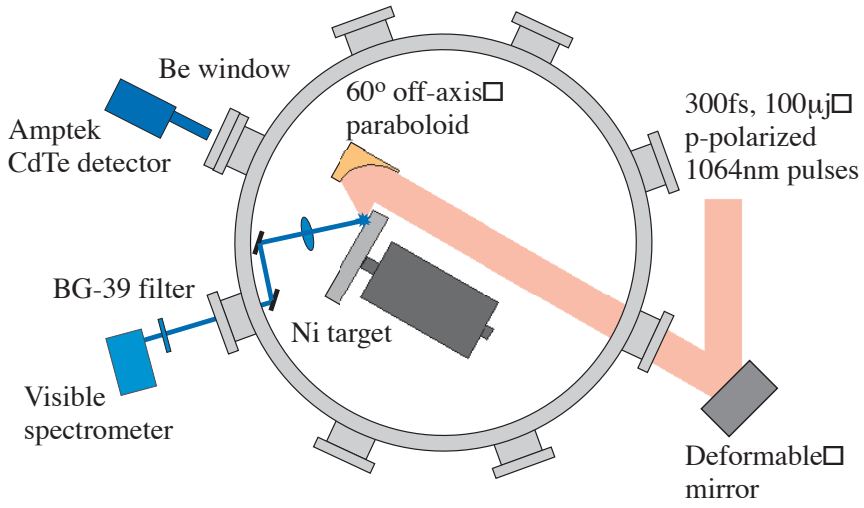

Figure 5.4: The fiber-laser-produced x-ray source experimental chamber. A deformable mirror is used to optimize the focus of an off-axis paraboloidal mirror. The visible spectrometer measures the second harmonic emitted along the specular direction to find the optimum target position. The x-rays are measured with a CdTe cooled detector (Amptek).

microscope objective and updates the configuration of the mirror's actuators to maximize the green signal (minimize the spot size). Once optimized, the actuators' position will be locked for the duration of the experiment. The stability of the laser wavefront was sufficient to maintain an optimum spot size for the duration of the experiment (several hours). The combination of small f-number focusing and adaptive wavefront correction yields a 2.3 μm full-width at half-maximum focal spot (Fig. 5.5). Thanks to such a small focal size, even the 50 μJ fiber CPA pulse energy can attain a focal intensity $I \simeq 2 \times 10^{15}$ W/cm^2

The Ni target is mounted inside the vacuum chamber (10^{-1} mbar) on a motorized stage and rotated to ensure that each laser shot interacts with a fresh area. The micro-plasma is imaged along the specular direction using an $f = 100$ mm lens onto the entrance slit of a visible spectrometer (Ocean Optics) through a BG39 filter that absorbs the 1064nm light and passes the second harmonic generated at the target-vacuum interface. The target position with respect the focal plane is optimized by maximizing the plasma second harmonic emission. A 2 μm-thick pellicle is used to protect the mirror from the debris emitted from the plasma.

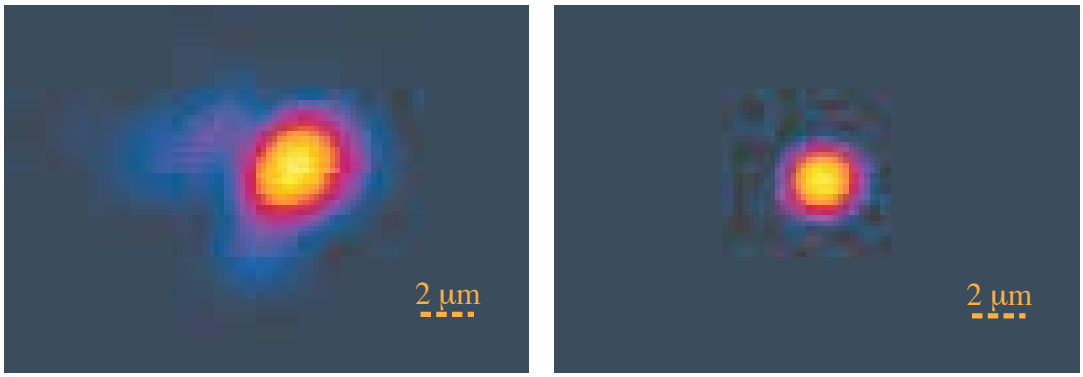

(a) (b)

Figure 5.5: The laser focal spot imaged by a 60× microscope objective before (a) and after (b) the deformable mirror optimization. The optimized spot full width at half maximum is 2.3 μm.

The x-ray spectrum is measured using a cadmium-telluride solid-state detector [105, 106] and a multi-channel analyzer from Amptek Inc. (XR-100T-CdTe and MCA-8000A). The diode, protected with a 75 μm-thick beryllium (Be) window, has an active area of 9 mm^2, a thickness of 1 mm and is thermo-electrically cooled down to $-30°C$. The detector is mounted along the direction of the target normal at 48 cm from the plasma through another Be window. It was calibrated using an Am^{241} radioactive source (13.95 keV and 17.74 keV lines).

5.3.2 Results and discussion

At intensities higher than 10^{14}W/cm^2 a laser pulse can deposit a sizeable fraction of its energy into the plasma electrons through a multitude of processes such as resonance absorbtion, vacuum and $\mathbf{J} \times \mathbf{B}$ heating (see section 2.3). The resulting hot electrons (with temperature T_e) acquire enough momentum to penetrate deep inside the solid-density target to produce continuum bremsstrahlung, as well as narrow-band Kα line radiation (typically $\delta\lambda/\lambda \simeq 10^{-4}$) at photon energies characteristic of the target material (see section 2.4).

The Ni ($Z = 28$) target was shot at a repetition rate of 1 kHz with 50 μJ pulse energy (on target) corresponding to $\sim 2 \times 10^{15}$ W/cm^2 peak intensity. The spectrum,

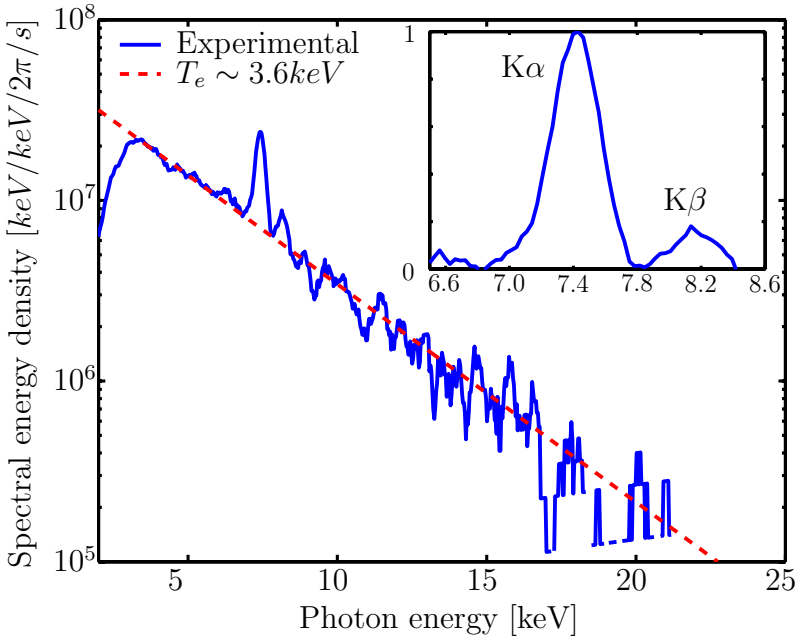

Figure 5.6: Hard x-ray spectrum from a Ni target obtained with 50 μJ pulses at $\sim 2 \times 10^{15}$ W/cm^2. The bremsstrahlung extends to photon energies higher than 20 keV with a characteristic electron temperature $T_e = 3.6$keV. The insert shows the bremsstrahlung-subtracted relative intensity plot of the Kα and Kβ lines on a linear scale.

shown in Fig. 5.6, was measured with the CdTe detector operating in single photon count mode (0.15 photon/pulse) for an exposure duration of 80 seconds. Both the bremsstrahlung and K-line emission are distinctly present.

The bremsstrahlung high energy tail extends to energies exceeding 20 keV. Its spectral energy density per unit bandwidth can be fitted to a single exponential decay (linear on a logarithmic scale) which is characteristic of a single-temperature Maxwellian electron energy distribution. The effective electron temperature is extracted from the fit $T_e \simeq 3.6$ keV. The low energy component (< 4 keV)is governed by the transmission of the Be filters which becomes almost fully transparent for photon energies > 4 keV.

Although the effective electron temperature is lower than the electron binding energy of the Ni K-shell (~ 8.3 keV), the Kα (at 7.48 keV) and Kβ (8.26 keV) lines are clearly observed (insert Fig. 5.6) with a relative intensity of 5-to-1, respectively. The Kα line measured linewidth is limited by the CdTe detector resolution to about

390 eV. It is expected however that this linewidth be of the order of a few eV [107].

The energy conversion efficiency into the Kα photons was 4.5×10^{-8} and the corresponding yield is 2×10^6 Kα photons per second into the half space. This conversion efficiency is calculated using the following formula:

$$\eta_{K\alpha} = T_{Be}\, \eta_D\, \frac{2\pi}{\Omega_D}\, \frac{N_{K\alpha}\, \hbar\, \omega_{K\alpha}}{P_{Laser}} \tag{5.2}$$

Here P_{Laser} is the laser average power on target and $N_{K\alpha}$ the number of $K\alpha$ photons – each with an energy of $\hbar\omega_{K\alpha}$ – detected per second by the CdTe detector. η_D, the Ni absorption probability in 1 mm-thick CdTe at the Kα photon energy, is taken equal to unity since the attenuation length is ~ 4.5 μm. T_{Be} is the transmission through both beryllium filters. Ω_D is the solid angle subtended by the detector surface seen from the plasma source and is used to estimate the total number of Kα photons emitted in the 2π assuming an isotropic emission.

The x-ray conversion efficiency is in agreement with previously published results obtained with sub-millijoule solid-state lasers (see table5.3.2). For a similar pulse energy Hou *et al.* [12] measured a conversion efficiency of 10^{-7} from a Molybdenum target (Z = 43) with a 22 fs laser. This agreement – in spite of a factor of ~ 20 difference in pulse duration τ – could be attributed to the weak dependence of the x-ray yield on τ as discussed in section 3.4.2. In fact, in a similar regime [12], the conversion efficiency scaled with $\propto \exp(-\tau/\beta)$, where $\beta \simeq 650$ fs.

In another experiment, Hagedorn et al. [108] focused 30 fs, 100 μJ pulses to a spot size of ~ 25 μm and obtained 5×10^{-9} conversion efficiency, one order of magnitude lower than the fiber laser experiment. This suggests that the x-ray yield has a stronger dependence on the laser energy fluence than it does on the pulse duration.

	Material Z	Duration fs	Energy μJ	Intensity W/cm^2	Efficiency η_{K_α}
Hagedorn et al. [108]	Ni(Z = 28)	30	100	2×10^{14}	5×10^{-9}
Fiber CPA	Ni (Z = 28)	350	50	2×10^{15}	4.5×10^{-8}
Hou et al. [15]	Mo(Z = 42)	22	58	1×10^{17}	10^{-7}
			120	2×10^{17}	2×10^{-6}

Table 5.1: K_α conversion efficiency comparison for various sub-millijoule x-ray sources.

5.4 Conclusion and future directions

In this chapter we presented seminal results on the use of femtosecond fiber lasers to produce hard x-ray radiation. 50 μJ, 300 fs pulses were tightly focused on a Ni target at the intensity of $\sim 2 \times 10^{15}$ W/cm^2, the highest intensity ever attained with a fiber system. The energy conversion efficiency into the Kα photons was comparable to results obtained using conventional solid-state systems (Ti:Sapphire) with similar pulse energy and a shorter duration.

The significance of this result lies in the fact that it extended, for the first time, fiber laser territories to the regime of high-intensity experiments. Crossing to the high-intensity regime could be instrumental in exporting over twenty years of laboratory laser-matter achievements – such as short-wavelength radiation and particle sources – to the realm of practical applications.

It should be noted, however, that the total x-ray yield produced in this experiment is too low to be useful for any practical application. For this reason, substantial improvements have to be achieved on three different thrusts: (i) pulse energy scaling to the millijoule range, (ii) average power (repetition rate) scaling to 10-100 watts, and (iii) developing beam combining schemes.

Both the thresholds of bulk damage and catastrophic self-focusing in fused silica limit the energy for ~ 1 ns stretched pulse to a few millijoules in an LMA fiber [13]. From [12] x-ray conversion efficiency scales with the pulse energy E as $\propto E^{1.5}$, for

$E > 100$ μJ (section 3.4.2). For E around 1 mJ, the conversion efficiency can be as high as 10^{-4}, i.e. 3-4 orders of magnitude improvement in the total x-ray yield compared with the current system. For this reason, it is important to improve the laser system in order to deliver mJ pulses in comparable pulse duration.

A complementary approach for higher x-ray yield dictates scaling the driving laser average power (or repetition rate). As mentioned before, fibers have a tremendous advantage over conventional solid-state lasers in term of thermal management properties. This enables high repetition rate systems that can deliver an average power exceeding one hundred watts [103, 109]. Conventional CPA components, such as metal-surface, grating-based compressors are not compatible with such high powers. For this reason, alternative stretcher and compressor technologies are needed. Recently, a compressor based on a large cross-section volume Bragg gratings [56] written in photo-thermal-refractive glass [110] was demonstrated with a 50 W system [111].

Additionally, the x-ray yield can be scaled considerably if one considers combining the outputs of a multitude of high average power, high energy fiber lasers. This approach is made practical thanks to the monolithic nature of fiber systems. To date, several high-power beam combining schemes have already been proposed [112, 113, 114, 115].

CHAPTER VI

EXTREME UV GENERATION USING FIBER LASERS

6.1 EUV Lithography and sources

EUV lithography Lithography is the process by which a pattern is transferred onto a photosensitive material for the purpose of manufacturing microelectronic or MEMS devices. In its most simple form, this process involves using a light source, such as a laser at wavelength λ, to project a patterned mask on a photoresist-coated semiconductor wafer. Diffraction limits the minimum feature half-pitch size F achievable by a lithographic system according to the formula:

$$F = k_1 . \frac{\lambda}{N_A}, \tag{6.1}$$

where k_1 is a process-dependent resolution factor typically $\sim 0.3 - 0.5$ for single patterning techniques, and N_A the numerical aperture of the projection system as seen from the wafer. Presently, deep ultraviolet (DUV) lithography systems use excimer lasers at a wavelength between $248 - 193$ nm. However, DUV lithography has been approaching its physical limits on the minimum attainable pattern size ($\sim$ 45 nm Intel, 2006). In order to keep up with Moore's law – a trend that has been valid since the 1970's according to which the number of transistors on an integrated circuit doubles every 24 months – the International Technology Roadmap for Semiconductors (ITRS) requires that printable patterns of 32 nm half-pitch be

adopted as industry standards by 2009.

EUV lithography is one technology that promises the required resolution for the 32 nm node and well beyond. It uses nanometer-wavelength radiation (in the extreme ultraviolet region of the spectrum) to imprint features of comparable scale. Taking advantage of existing high-reflectivity ($\sim$ 60 %), narrow-bandwidth (2 %) Molybdenum-Silicon multi-layer coated mirrors at $\lambda = 13.5$ nm, the semiconductor industry has chosen this wavelength for the light source of the next generation lithography instrument [116]. However, for EUV lithography to be cost effective, it has to be compatible with high volume manufacturing methods. This requires that EUV scanners be capable of exposing 120 wafers per minute. Taking into account the photo-resist sensitivity, the above requirement translates into a source that outputs 150 W of narrow band 13.5 nm radiation at the intermediate focus of the EUV collection optics. In addition to the brightness requirement, the EUV source has to produce very little debris. This is necessary to prolong the life-time of the expensive multi-layer optics and prevent frequent down-times.

EUV sources Two different technologies, namely gas discharge plasmas (DPP) and laser-produced plasmas (LPP), are competing to drive the source for the next generation EUV lithography scanner. As of 2007, neither technology has demonstrated a practical source that meets the industry requirements. The prevalence of one or the other source is subject to controversy and is discussed in a number of recent articles [117, 118, 119, 120].

Briefly, DPP sources work by discharging a strong electrical pulse (several joules) across two electrode in a chamber filled with low pressure Xe ($\sim 10 - 100$ Pa). The strong discharge ignites a plasma which in turn emits the EUV radiation. Since they directly converted electrical power into EUV radiation, DPP are more efficient and compact than LPP. However, they face very serious challenges: Firstly, they produce

a copious amount of debris which reduces the quality and lifetime of the optics as well as the electrode system. Secondly, they suffer a poor collection efficiency since the EUV is emitted through a capillary tube. And thirdly, DPP have poor thermal management properties which make them costly and difficult to scale to higher powers in order to meet the brightness requirement.

LPP sources are produced when an intense laser is focused on targets containing materials that have emission lines around 13.5 nm such as Li [121, 122], O [123], Xe [124, 125, 126] and Sn [127, 128, 129]. For efficient EUV generation, the plasma should be heated to a temperature of a few tens of eV ($\sim$ 30 eV) in order to drive the atoms to ionization levels responsible for EUV emission. This requires pump laser intensities around $10^{10} - 10^{11}$ W/cm^2 for nanosecond pulses. Since energy has to be converted from electrical to infra-red (or visible) and subsequently to EUV, LPP are inherently less efficient than DPP. On the other hand, they have a simpler architecture which makes them compatible with mass limited targets thus reducing the debris generated at the interaction. More importantly, LPP sources are scalable with the driving laser power and repetition, a very promising attribute necessary to meet the EUV lithography brightness requirements.

Sn-containing targets have proven to be the most efficient EUV emitters, with demonstrated efficiencies around 5% for bulk [130] and 2-3% for mass limited geometries [131, 132]. Therefore, to produce 150 W of in-band EUV at the intermediate focus of the collection optics ($\sim$ 60 % efficient), about 10 kW of laser power is needed.

Different schemes for multiplexing a number of high power lasers have been proposed based on CO_2 lasers [128, 133, 125] and diode-pumped solid-state lasers [132, 129]. However, state of the art sources were only able to achieve 10-25 W of EUV [128, 129], which justifies the need to search for a different approach to practically provide the laser power needed.

It is worth noting that the source is far from being the only challenge facing EUV lithography. In fact, there are other issues which impede the realization of this technology as a high-volume manufacturing process. Of these we mention the photo-resist sensitivity to EUV radiation, the optics reflectivity and lifetime, mask designs, etc.

6.2 EUV generation from solid Sn using a fiber laser

The EUV power produced by conventional lasers is still orders of magnitude short from meeting the industry specifications for a high volume, cost-effective lithographic process. We claim that multiplexing high average-power all-fiber systems, operating at MHz repetition rate, could offer an scalable solution for this challenge.

The enabling approach of reaching required high peak powers for hot-plasma generation with a fiber laser was to use very large core fibers in the last amplification stage. Despite the highly multimode nature of such fibers, the coiling of low numerical aperture (N.A.) fibers can be used to control mode quality at the system output. In this section we describe the fiber laser built to drive the EUV source and a proof of principle EUV generation experiment.

6.2.1 Ytterbium-doped nanosecond fiber laser

A ytterbium-doped all-fiber laser system providing multi-MW peak power [134] was built to drive the EUV plasma source (Fig. 6.1). The system was seeded with an electric-pulse-driven, single-longitudinal-mode diode laser with a bandwidth of 1 nm at $\lambda = 1064$ nm. This seeding scheme offers an exceptional versatility in choosing the pulse parameters (duration, shape, repetition rate) and conveniently allows for the introduction of prepulses with accurate control of contrast and relative delay.

The seed pulses are amplified in a 4-stage fiber amplifier. The first two stages are

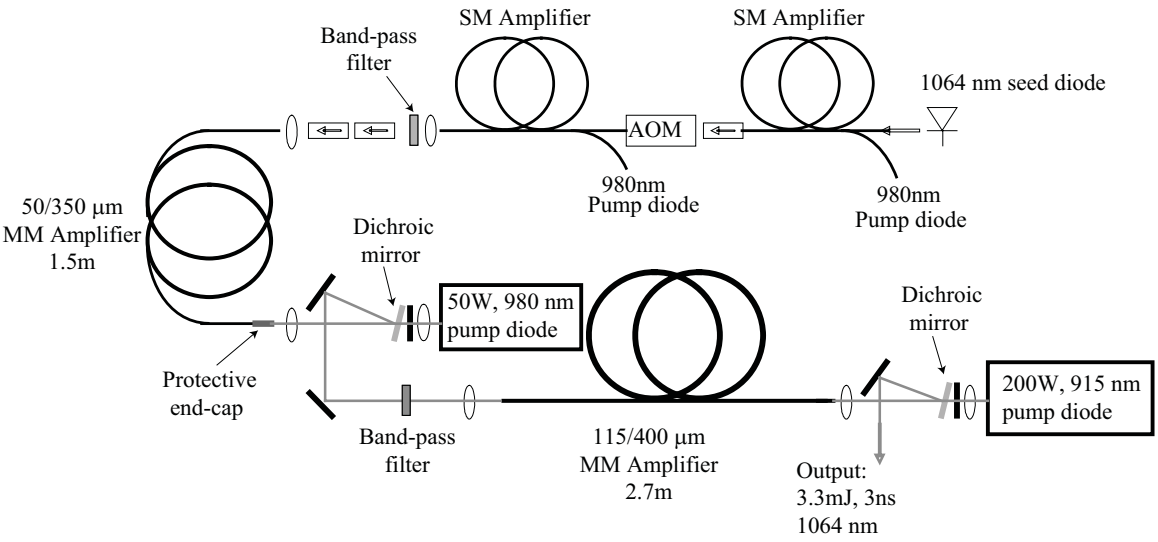

Figure 6.1: Schematic of the high peak-power fiber laser.

single-mode (SM) Yb-doped fiber pre-amplifiers, core-pumped with telecom-grade SM diodes at 980 nm. The third stage is a 1.4 m long, Yb-doped multimode (MM) fiber with a 50 μm core (N.A. 0.06) and 350 μm hexagon-shaped cladding (N.A. 0.45). This stage is cladding-pumped by 50 W at 980 nm. The last power amplifier stage uses a 2.7 m MM fiber with 115 μm core (N.A. 0.06) and 400 μm cladding (N.A. 0.47) end-pumped with up to 200 W from a diode laser emitting at $\lambda = 915$ nm. In order to suppress the amplified spontaneous emission (ASE) all stages were isolated either by an acousto-optic modulator (pre-amplifiers) or by 10-nm bandpass interference filters centered at 1064 nm (MM stages). Due to their large core size, the last two stages can support many higher order modes, inevitably leading to severe degradation in the beam quality. For this reason, the last two fibers were coiled to a radius of 12 cm to filter out the higher modes. This dramatically improves the beam quality at the expense of the amplifier gain.

This system is capable of producing nanosecond pulses of up to 2.4 MW peak power with a beam quality factor $M^2 \simeq 10$.

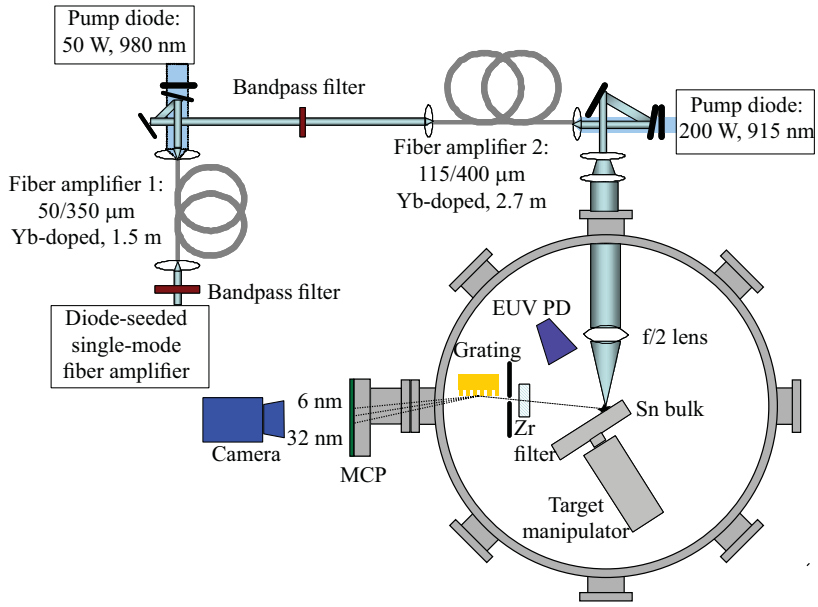

Figure 6.2: Experimental set-up used for the generation of EUV.

6.2.2 Experimental setup and diagnostics

The experimental set-up is shown in Fig. 6.2. The fiber laser pulses, obliquely incident at 45°, are focused with a 5 mm focal length lens on a 1 cm thick Sn disk target in a vacuum environment of 10^{-5} Torr. Although mass-limited Sn targets have proven to produce less debris - an important requirement to prolong the lifetime of expensive EUV optics, we still have opted to carry the proof of principle experiment with a bulk target since it doesn't require a special dispenser apparatus. The laser spot diameter on focus was measured to be between $50 - 70$ μm FWHM using the knife-edge technique. A computer-controlled motion stage rotates the target to expose fresh Sn material to every laser shot while maintaining the interaction region at the waist of the focused beam (± 7 μm surface wobble). A 2 μm-thick nitro-cellulose pellicle was mounted between the target and the lens to protect the latter from the debris emitted from the interaction. Although MHz repetition rate is attainable we have chosen to operate at 50Hz to minimize the debris sputtered in the experimental chamber. The radiation generated is characterized using two

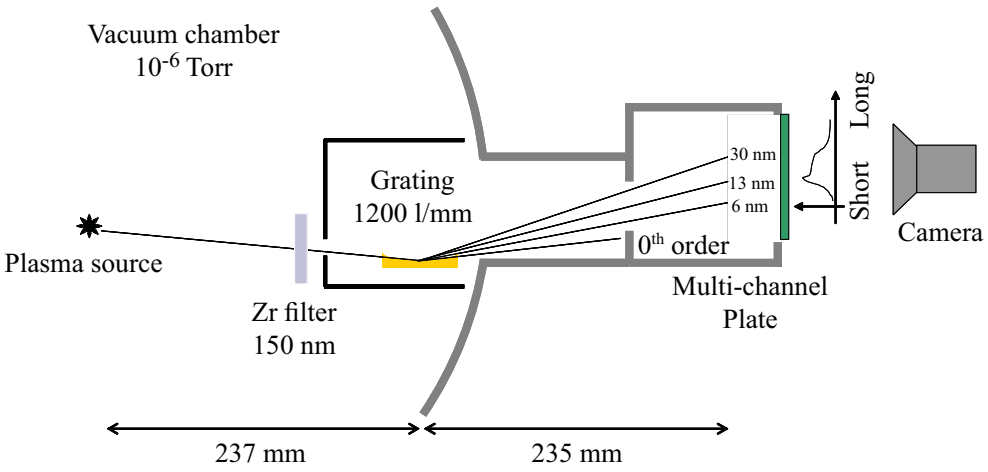

Figure 6.3: EUV Spectrometer.

diagnostics: an EUV spectrometer aligned along the 30° direction with respect to the target's normal, and a home-built EUV photodiode.

EUV spectrometer In order to spectrally characterize the radiation emitted from the laser-produced plasma in the EUV window, we have constructed a spectrometer based on the design proposed in [135, 136] (see Fig 6.3). Conventional grazing-incidence concave spectrometers focus a slit located on the Rowland circle – the imaginary circle whose radius equals that of the spectrometer's grating – along a curved segment of that same circle. Thus, not only such a spectrometer requires a curved (or flexible) detector, but it also induces a significant astigmatism which compromises the spectral resolution of the instrument. On the other hand, the grazing incidence grating in [135, 136] has carefully designed variable line-spacings that corrects for the aberrations and focus the dispersed spectrum along a flat surface (flat-field) making possible the use of planar MCPs or CCDs.

The grating we have used (manufactured by Hitachi Ltd.) has a nominal pitch $\sigma_0^{-1} = 1200$ grooves/mm and was designed for the $5 - 40$ nm spectral window. At the grazing incidence of 87° it disperses a slit located at 237 mm from its center onto a flat field at 235 mm from the center, opposite the slit, where a multi-channel

plate (MCP) is mounted. Since the Sn EUV spectrum consists of a broad unresolved transition-array (UTA) with no sharp (sub-nanometer) features, it was advantageous to align the spectrometer such that the plasma source acts as an entrance slit. This maximizes the collection efficiency without hurting the spectral resolution since the source is expected to be of comparable size to the 50 μm laser focal spot.

The MCP's phosphorescent screen is imaged with a 12-bit cooled CCD camera using a lens. In this configuration the spectral window between $6-32$ nm is resolved with ~ 320 pixels. In order to prevent the scattered laser light from contaminating the MCP signal, a 150 nm-thick zirconium filter (from Lebow Company) was placed between the plasma and the grating. The Zr filter provided an attenuation factor of the order of 10^{-5} or better for the laser light $\lambda = 1064$ nm while transmitting about 55% of the light around $\lambda = 13.5$ nm. Alternately an aluminum filter of the same thickness was used to mark the 17 nm Al L-absorption edge. This sharp edge was used to calibrate the spectrometer based on the geometry and the grating equation:

$$m\lambda = \sigma_0 \left(\sin\theta_i + \sin\theta_r\right). \tag{6.2}$$

Here the diffraction order m is equal to 1, θ_i and θ_r are the incident and diffracted angles, respectively.

EUV Photodiode In addition to the spectrometer, a custom-designed photodetector (Fig. 6.4) was used to measure the absolute power radiated at 13.5 nm within a narrow bandwidth of 2%. At the heart of the detector is a Hamamatsu G1127-02 GaAsP photodiode with an active area of 21 mm^2. Although it is designed for the blue-UV region, this diode is highly sensitive in the EUV [137] if its protective glass window is removed. Fig. 6.5 (b) shows the G1127-02 responsivity. At $\lambda = 13.5$ nm, it draws a current of 0.14 A per watt of incident radiation.

A combination of an ultra-thin Zr foil and Mo/Si multilayer mirror filters the

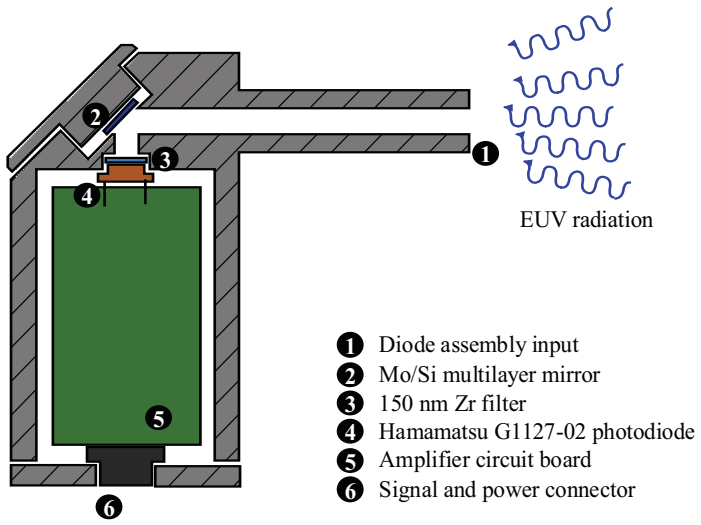

Figure 6.4: Calibrated EUV detector based on a Hamamatsu G1127-02 diode with the glass window removed. A combination of Zr filter and a narrow band Mo/Si multi-layer mirror ensures a high sensitivity to radiation at 13.5 nm with 2% bandwidth.

incident radiation for a narrow band (0.6 nm) around 13.5 nm. The Zr filter (from Lebow Company) is 150 nm thick, and is mounted on Ni mesh for support. Between $7 - 14$ nm its transmission is about 60% (Fig. 6.5 (a)), and its rejection to the driving laser wavelength is better than 10^{-5}. Further filtering of out-of-band radiation is achieved by using a Mo/Si multilayer mirror at 45° incidence. Typically these mirrors have a peak reflectivity of 60-70% at the design wavelength and a bandwidth of ~ 0.5 nm [138, 139].

The diode assembly also houses an imbedded low-noise transimpedance amplifier that makes it sensitive to micro-joule level EUV pulses. In order to reduce the noise due to the charged particles and EMP (electro-magnetic pulse) generated at the plasma, we used a 2 Tesla magnetic dipole to deflect the electrons away from the detector which was further protected with 1/8" lead shielding.

A cross-calibration of the EUV photo-detector was carried out at Cymer Inc. using a characterized Xe pinch gas discharge source. For 24 mJ pulses of in-band EUV emitted into the 2π sr, the detector produced an integrated signal of 61 nano-Volt-seconds at a distance of 127 cm from the plasma. The calibration factor ζ

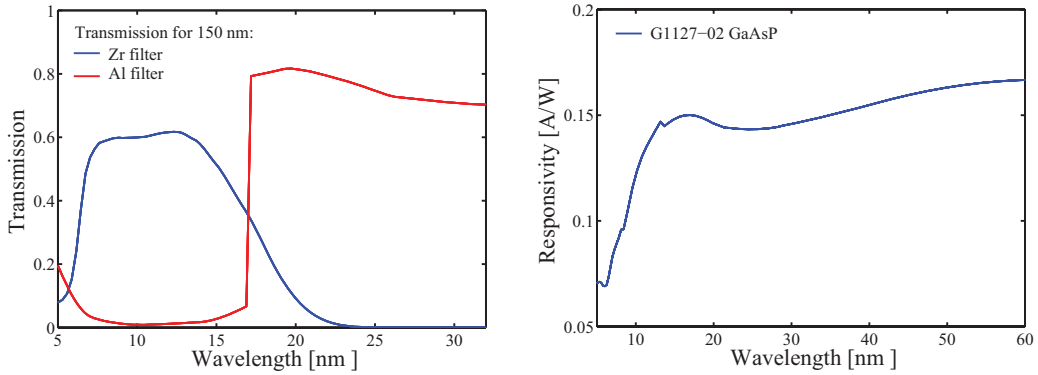

Figure 6.5: (a) Transmission curves for 150 nm Zr and Al filters. Around $\lambda = 13.5$ nm the Zr filter is ~ 60 % transparent while the Al filter is totally opaque because of the absorption edge at 17 nm. (b) Responsivity of the Hamamatsu G1127-02 in the EUV window. At $\lambda = 13.5$ nm the responsivity is 0.14 A/W.

can then be deduced from the geometry:

$$\zeta = 24 \text{ mJ} \times \frac{21 \text{ mm}^2}{2\pi 127^2 \text{ cm}^2} \times \frac{1}{61 \text{ nV} - \text{s}} \simeq 0.8 \text{ J/Vs} \tag{6.3}$$

Thus, the EUV energy (in Joules) emitted from the fiber laser-produced plasma into the half space within a 2% bandwidth, can be calculated using the following formula:

$$\mathcal{E}_{13.5} = \frac{2\pi d_0^2}{21} \cdot \zeta \int V(t)\, dt \tag{6.4}$$

where d_0 is the plasma-detector distance in mm, and $V(t)$ the diode voltage measured by an 50 Ω-terminated oscilloscope.

6.2.3 Results

Fig. 6.6 shows the EUV spectrum obtained from bulk Sn irradiated with an intensity of 1.3×10^{10} W/cm^2. It is characterized by a broad spectral feature around 13.5 nm albeit its intensity relative to the EUV background is low. Photodiode measurements under similar irradiation conditions (Fig. 6.7(a)) yielded an integrated voltage of 9.2×10^{-9} V-s for $d_0 = 77$ mm. Using Eq. 6.4, we calculate the in-band EUV energy to be 1.3×10^{-5} J. Finally, the conversion efficiency (C.E.) into 2π sr within 2%

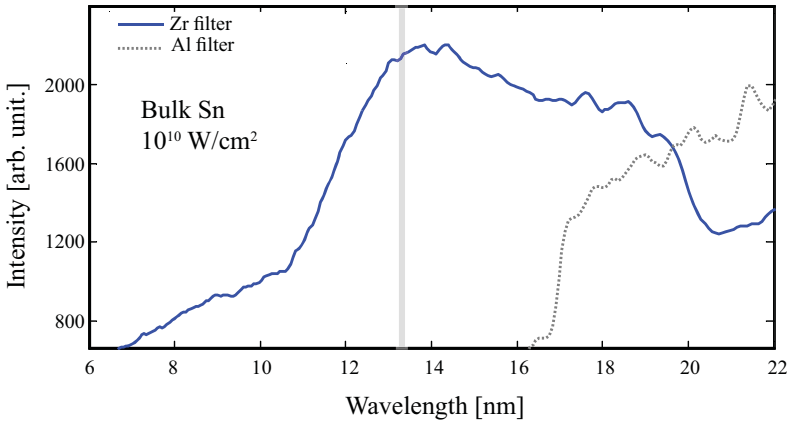

Figure 6.6: EUV spectra from bulk Sn measured through a 150-nm Zr filter (solid line) and 150-nm Al filter (dotted line) at an intensity of 1.3×10^{10} W/cm^2.

bandwidth is given by:

$$\text{C.E.} = \frac{\mathcal{E}_{13.5}}{\mathcal{E}_{1064}} = \frac{1.3 \times 10^{-5}}{2.3 \times 10^{-3}} \simeq 0.6\%. \tag{6.5}$$

The C.E. calculation is based on a measurement where the photodiode is aligned along the normal to the target surface and assumes an isotropic emission into the half space. This assumption was tested by taking a series of measurements between 5° and 85°, in the table plane, opposite the laser side. We found that the spatial distribution was rather isotropic (see Fig. 6.7(b)), within an average standard deviation $\overline{\sigma} = 13\%$. The weak apparent peak close to the normal could be attributed to a signal contamination due to electrons or ions which are found to be emitted primarily toward the normal direction.

These results are in agreement with previously published bulk Sn experiments [127] irradiated with solid state lasers at comparable intensities. It is expected that the C.E. increases as the intensity increases to the 10^{11} W/cm^2 level for nanosecond pulses. These higher intensities were not attainable at the time the experiment was conducted, which required a major laser upgrade [140]. The upgraded laser was capable of delivering more than 6 mJ in 5 ns and intensities exceeding 2×10^{11} W/cm^2.

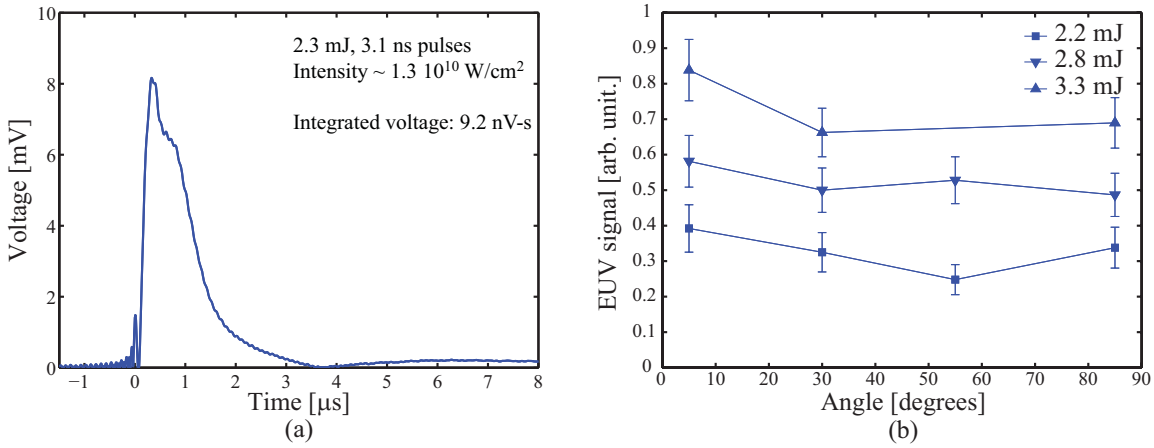

Figure 6.7: EUV photo-detector measurements. (a) shows the signal read by a 50 Ω-terminated oscilloscope for a laser pulse energy on target of 2.3 mJ. The corresponding conversion efficiency is 0.6%. The spatial distribution of the EUV signal as a function of the detector angle is plotted in (b) for 3 different pulse energies.

6.3 EUV generation from mass-limited Sn targets with a nanosecond fiber lasers

Sn-doped water droplet targets have demonstrated conversion efficiency in excess of 2% [131], with little or no debris emission. This is achieved by limiting to a minimum the amount of Sn atoms available for each laser pule, without reducing the 13.5 nm emission. However, the droplet target has been demonstrated with high-energy ($\sim$ 100 mJ) Q-switched solid state lasers focused to intensities around $1 - 2 \times 10^{11}$ W/cm^2. While these intensities are attainable by an upgraded version of the laser described in section 6.2.1, the pulse energies are about two orders of magnitude higher than what fiber lasers can achieve. Therefore, it became important to investigate the compatibility of fiber lasers with practical mass-limited targets, capable of meeting the brightness and low-debris requirements of EUV lithography. This section is intended to briefly discuss recent results achieved in collaboration with the laser plasma laboratory at CREOL, University of Central Florida [141].

The droplet target experimental set-up is shown in Fig. 6.8. The fiber laser pulses, up to 6 mJ in energy, were focused with a 60 mm focal length lens on the

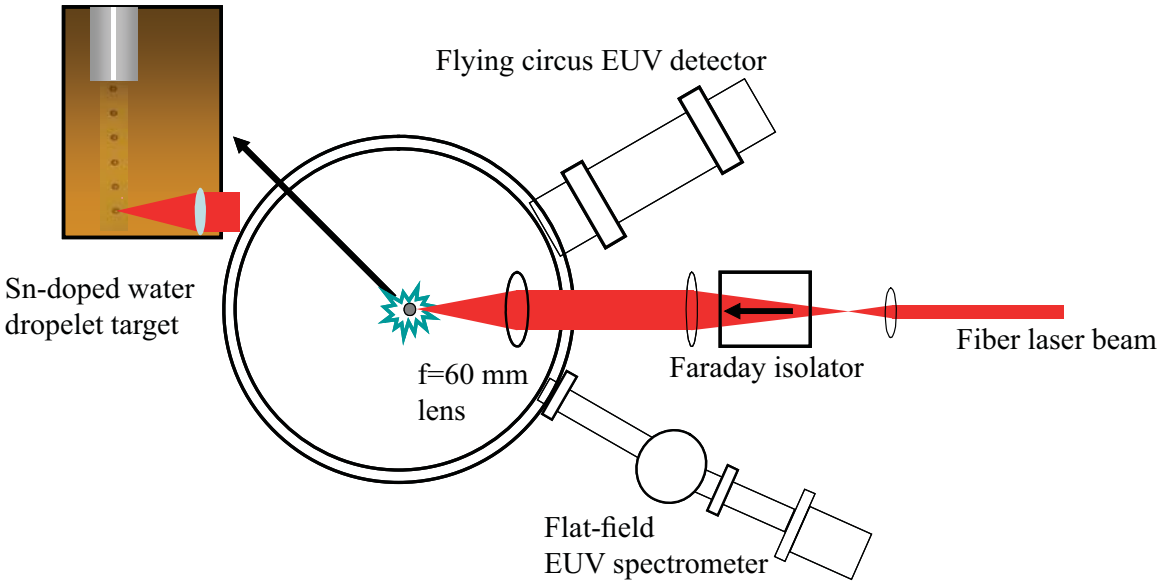

Figure 6.8: The experimental set-up showing the output of the fiber laser and the Sn-doped water droplet chamber. A flat-field spectrometer and calibrated EUV detector were used to characterize the radiation at 13.5 nm.

Sn solution droplets. The repetition rate of the laser was synchronized to that of the droplet piezoelectric driver ($\sim$ 30 kHz). In order to prevent back-reflection from the plasma from damaging the amplifiers, a high-power Faraday isolator (Electro-Optics Technologies, Inc) was used. Two complementary diagnostics were used to characterize the EUV radiation emitted from the plasma: A flat-field spectrometer similar to the one described in section 6.3 and a narrow-band detector based on AXUV-100G photodiode and a 45° Mo/Si multi-layer mirror.

Figure 6.9 shows the spectrum from Sn-doped water droplet at a laser intensity of 8×10^{10} W/cm^2. Unlike the spectrum obtained in Fig. 6.6, the droplet spectrum exhibits a very pronounced peak at around 13.6 mm due to a Sn unresolved transition array. Additionally, are present a number of oxygen lines from O V, O VI and possibly O VII. The conversion efficiency measured by the EUV detector was $\sim$ 2%, comparable to the efficiency from high energy lasers and similar targets [131].

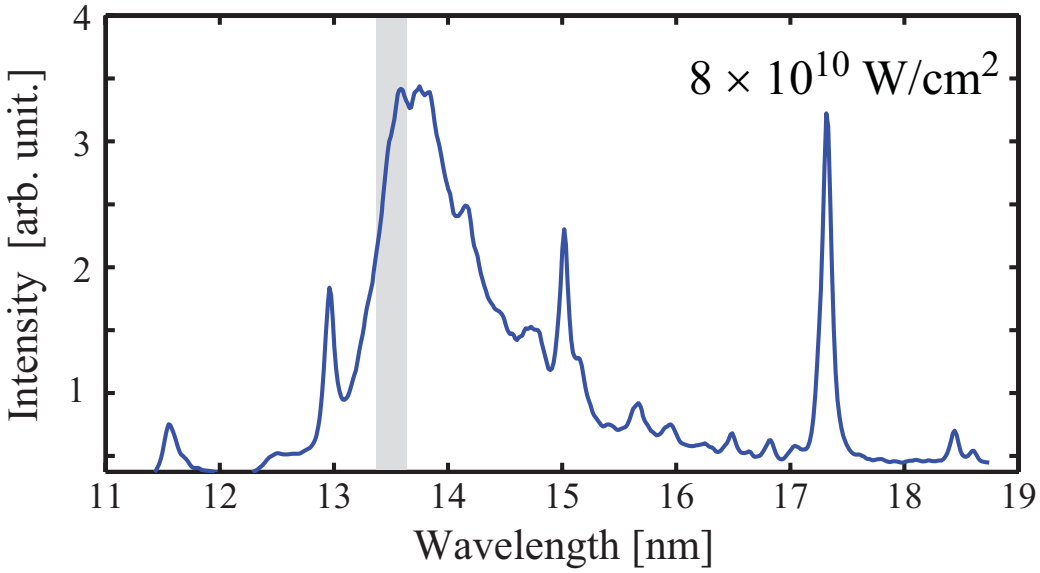

Figure 6.9: A spectrum from Sn-doped water droplets obtained at a laser intensity of 8×10^{10} W/cm^2 showing a Sn UTA peak around 13.5 nm as well as a number of Oxygen lines. Measurements using a calibrated EUV detector yielded a C.E. of 2.1% into 13.5 nm radiation within a 2% bandwidth (gray area).

6.4 Conclusion

We have demonstrated, and for the first time, the efficient generation of 13.5 nm radiation using an all-fiber laser system. Even though our conversion efficiency results were several times lower than what have been reported using Q-switched solid state lasers [131, 132], they establish the competence of fiber lasers in fields of laser-produced plasmas in general and EUV generation in particular. Additionally, these results pave the way to a new generation of laboratory high-power high-intensity experiments with applications in metrology, microscopy as well as lithography.

CHAPTER VII

CONCLUSION AND FUTURE DIRECTIONS

In part, this dissertation concerns the study of x-rays and hot electrons produced from a relativistic laser-solid interaction in the λ^3 regime. In this regime, millijoule-level femtosecond pulses from a standard Ti:sapphire CPA system are tightly focused to a spot comparable with the wavelength to yield intensities exceeding the relativistic threshold at kilohertz repetition rates.

Motivated by the potential usefulness of an ultrafast x-ray probe for time-resolved studies, the x-ray source produced by a λ^3 laser has been studied. In particular, knife-edge shadowgraphs revealed a source diameter in the vicinity of ~ 10 μm for most target materials. Although this was several times larger than the focal spot of the driving laser, such a minute source is advantageous for high-resolution x-ray imaging applications. Moreover, a small source also entails higher spatial coherence properties. These have been investigated by recording the x-ray diffraction pattern from a straight edge. It was found that, for a Si plasma, the transverse coherence length at 60 cm from the source is comparable to that typically expected in synchrotron facilities. This finding implies that the λ^3 x-ray source could be useful for phase-sensitive imaging techniques.

In addition, the energy distributions of hot electrons have been investigated in the $10^{17} - 2 \times 10^{18}$ W/cm^2 range. Taking advantage of the high repetition rate of the system, the electron spectra were measured by accumulating $\sim 10^3$ laser shots, in contrast to previous studies at similar intensities which are typically done

in the single shot regime. The electrons specularly escaping the Al plasma were found to have a Maxwellian-like distribution with a characteristic temperature that scaled like $(I\,\lambda^2)^{0.6}$. In the case of the SiO_2 target with an intermediate plasma scale-length $(0.1\lambda - 0.5\lambda)$ relativistic electrons jets were observed close to the specular direction. The energy distribution of the jet electrons differed significantly from the expected Maxwellian and exhibited a high-energy group forming a spectral peak close to 780 keV. Although the nature of the heating mechanisms producing the high-energy group are not fully understood, the dependence of the peak energy on the scale-length suggests that the jet electrons are guided and accelerated by quasi-static fields generated by the relativistically driven charged particles close to the critical surface.

Both simulations and experimental studies are necessary to further the understanding of the relativistic jets. For instance, a finer scan of the plasma scale-length could yield an even hotter spectrum. Also, changing the focal spot size while keeping a fixed intensity could be insightful since the quasi-static fields are strongly dependent on the transverse density gradients. From practical perspective, this result marks the first time relativistic electron beams were generated at kilohertz repetition rates from a laser-solid interaction. These beams, believed to have a temporal duration comparable to that of the driving laser, could be used for time-resolved electron diffraction experiments. Furthermore, if their energy were increased to beyond the MeV level – the threshold for pair production, they could be used to drive a laser-produced positron source with applications in material sciences.

Pioneering laser-plasma experiments were also undertaken in an equally interesting but fundamentally different regime, that of high peak power, high average power fiber lasers. This has been enabled by the emergence of large mode area fibers capable of supporting millijoule-level nanosecond pulses in a near-diffraction limited beam. Moreover, due to the excellent thermal properties of fibers, these lasers are

potentially capable of reaching the kilowatt range [103, 104], which make them an appealing driver for high-yield x-ray sources.

In one experiment, a Ni Kα source driven by an ultrafast fiber laser has been demonstrated at 1 kHz repetition rate. The intensities achieved in this experiment, up to 2×10^{15} W/cm^2, were believed to be the highest that had been achieved from a fiber system and the conversion efficiency into the Ni Kα line was comparable to those obtained by Ti:sapphire lasers with a similar pulse energy ($\sim$ 100 μJ). Although, the total x-ray yield produced by this source was too low for practical applications, there exist several approaches that could significantly increase the photon count. First, the scaling of the pulse energy to the millijoule level [57] is expected to increase the conversion efficiency by over two orders of magnitude [12]. Secondly, the scaling of repetition rate to the 100 kHz range is a straight forward approach especially since KW-range lasers haven been demonstrated [14]. And thirdly, the multiplexing of many fiber laser beams is an active area of research [112, 113, 114, 115] that promises to push fiber lasers to even higher intensities.

At much lower intensities ($\sim 10^{10}$ W/cm^2), the efficient generation of extreme UV generation has been demonstrated for the first time using nanosecond fiber lasers. This is relevant in the context of next generation lithography that requires a bright source of 13.5 nm radiation in order to attain the 32 nm half-pitch node by year 2011. In a proof-of-principle experiment, a bulk Sn target was irradiated with up to 3.3 mJ, 3 ns pulses from a ytterbium-doped all-fiber laser system at 1064 nm. The emitted radiation was characterized using a grazing incidence spectrometer and a cross-calibrated photodiode. At the intensity of 1.3×10^{10} W/cm^2 the conversion efficiency into the half-space within 2% bandwidth centered at 13.5 nm was 0.6%. Subsequent experiments with an upgraded fiber laser and a mass limited Sn droplet source yielded a conversion efficiency in excess of 2%. Although the EUV yield obtained in these experiments was too low to meet the requirements set by the

semiconductor industry, the high average power and monolithic properties of fiber lasers offer a promising solution that could power a production-worthy lithography tool.

BIBLIOGRAPHY

[1] D. Strickland and G. Mourou. Compression of amplified chirped optical pulses. *Opt. Comm.*, 56:219–221, 1985.

[2] Xiaoyan Liang, Yuxin Leng, Cheng Wang, Chuang Li, Lihuang Lin, Baozhen Zhao, Yunhua Jiang, Xiaoming Lu, Minyuan Hu, Chunmei Zhang, Haihe Lu, Dingjun Yin, Yongliang Jiang, Xingqiang Lu, Hui Wei, Jianqiang Zhu, Ruxin Li, and Zhizhan Xu. Parasitic lasing suppression in high gain femtosecond petawatt ti:sapphire amplifier. *Opt. Express*, 15:15335–15341, 2007.

[3] S. W. Bahk, P. Rousseau, T. A. Planchon, V. Chvykov, G. Kalintchenko, A. Maksimchuk, G. A. Mourou, and V. Yanovsky. Generation and characterization of the highest laser intensities. *Optics Lett.*, 29:2837–2839, 2004.

[4] G. Mourou, Z. Chang, A. Maksimchuk, J. Nees, S. V. Bulanov, V. Yu. Bychenkov, T. Zh. Esirkepov, N. M. Naumova, F. Pegoraro, and H. Ruhl. On the design of experiments for the study of relativistic nonlinear optics in the limit of single-cycle pulse duration and single-wavelength spot size. *Plasma Phys. Rep.*, 28:12–27, 2002.

[5] A. Couairon, J. Biegert, C. P. Hauri, W. Kornelis, F. W. Helbing, U. Keller, and A. Mysyrowicz. Self-compression of ultra-short laser pulses down to one optical cycle by filamentation. *J. Mod. Opt.*, 53:75–85, 2006.

[6] C. P. Hauri, A. Trisorio, M. Merano, G. Rey, R. B. Lopez-Martens, and G. Mourou. Generation of high-fidelity, down-chirped sub-10 fs mj pulses through filamentation for driving relativistic laser-matter interactions at 1 khz. *Appl. Phys. Lett.*, 89:151125, 2006.

[7] J. Nees, B. Hou, B. Bowes, N. Naumova, A. Mordovanakis, E. Power, M. C. Downer, and G. Mourou. Distinctive physical effects and applications approaching the relativistic lambda-cubed regime. *IEEE J. Sel. Top. Quantum Electron.*, 12:223–232, 2006.

[8] X.-W. Chen, X.-F. Li, J. Liu, P.-F. Wei, X.-C. Ge, R.-X. Li, and Z.-Z. Xu. Generation of 5 fs, 0.7 mj pulses at 1 khz through cascade filamentation. *Opt. Lett.*, 32:2402–2404, 2007.

[9] J. Nees, N. Naumova, E. Power, V. Yanovsky, I. Sokolov, A. Maksimchuk, S.-W. Bahk, V. Chvykov, G. Kalintchenko, B. Hou, and G. Mourou. Relativistic generation of isolated attosecond pulses: a different route to extreme intensity. *J. Mod. Opt.*, 52:305–319, 2005.

[10] N.M. Naumova, J. Nees, and G. Mourou. Relativistic attosecond physics. *Phys. Plasmas*, 12:056707, 2005.

[11] N. Naumova, I. Sokolov, J. Nees, A. Maksimchuk, V. Yanovsky, and G. Mourou. Attosecond electron bunches. *Phys. Rev. Lett.*, 93:195003, 2004.

[12] B. Hou, J. A. Nees, W. Theobald, G. Mourou, L. M. Chen, J-C. Kieffer, A. Krol, and C.C. Chamberlain. Dependence of hard x-ray yield on laser pulse parameters in the wavelength-cubed regime. *Appl. Phys. Lett.*, 84:2259–2261, 2004.

[13] A. Galvanauskas, Z. Sartania, and M. Bischoff. Millijoule femtosecond fiber-cpa system. In *Advanced Solid-State Lasers*, page postdealine paper PD3, January 28-31 2001.

[14] V. Fomin, A. Mashkin, M. Abramov, A. Ferin, and V. Gapontsev. 3 kw yb fibre lasers with a single-mode output. In *International Symposium on High-Power Fiber Lasers and their Applications*, June 26-30 2006.

[15] B. Hou, J. Nees, A. Mordovanakis, M. Wilcox, G. Mourou, L.M. Chen, J.-C. Kieffer, C.C. Chamberlain, and Krol A. Hard x-ray generation from solids driven by relativistic intensity in the lambda-cubed regime. *Appl. Phys. B*, 83:81–85, 2006.

[16] D. Boschetto, A. Mordovanakis, D. Kumah, J. Nees, B. Hou, G. Mourou, R. Clarke, and A. Rousse. Spatial coherence properties of a compact and ultrafast laser-produced plasma kev x-ray source. *Appl. Phys. Lett.*, 90:011106, 2007.

[17] K.-H. Liao, A. G. Mordovanakis, B. Hou, G. Chang, M. Rever, G. Mourou, J. Nees, and A. Galvanauskas. Generation of hard x-rays using an ultrafast fiber laser system. *Opt. Express*, 15:13942 – 13948, 2007.

[18] A. Mordovanakis, K.-C. Hou, Y.-C. Chang, M.-Y. Cheng, J. Nees, B. Hou, A. Maksimchuk, G. Mourou, and A. Galvanauskas. Demonstration of fiber-laser-produced plasma source and application to efficient extreme uv light generation. *Opt. Lett.*, 31:2517–2519, 2006.

[19] P. Gibbon. *Short Pulse Laser Interaction with Matter*. Imperial College Press, London, 2005.

[20] W. L. Kruer. *The physics of laser plasma interaction*. Westview Press, Boulder Co, 2003.

[21] T. W. Johnston and J. M. Dawson. Correct values for high-frequency power absorption by inverse bremsstrahlung in plasmas. *Phys. of Fluids*, 16:722–722, 1973.

[22] N.G. Denisov. On a singularity of the field of an electromagnetic wave propagated in an inhomogeneous plasma. *Sov. Phys. JETP*, 4:544–553, 1957.

[23] V. L. Ginzburg. *Propagation of electromagnetic waves in plasma*. Gordon and Breach, New York, 1961.

[24] D. W. Forslund, J. M. Kindel, and K. Lee. Theory of hot-electron spectra at high laser intensity. *Phys. Rev. Lett.*, 39:284–288, 1977.

[25] F. Brunel. Not-so-resonant, resonant absorption. *Physical Review Letters*, 59:52–55, 1987.

[26] G. Bonnaud, P. Gibbon, J. Kindel, and E. Williams. Laser interaction with a sharp-edge, overdense plasma. *Laser Part. Beams*, 9:339–354, 1991.

[27] P. Gibbon and A. R. Bell. Collisionless absorption in sharp-edged plasmas. *Phys. Rev. Lett.*, 68:1535–1538, 1992.

[28] K. G. Estabrook and W. L. Kruer. Absorption of the energy of a short laser pulse obliquely incident of a highly inhomogeneous plasma. *Tech. rept. Lawrence Livermore National Laboratory*, UCRL50021-86, 1986.

[29] A. A. Andreev, J. Limpouch, and A. N. Semakhin. Absorption of the energy of a short laser pulse obliquely incident of a highly inhomogeneous plasma. *Bull. Russ. Acad. Sci.*, 58:1056–1063, 1994.

[30] W. L. Kruer and K. Estabrook. $\boldsymbol{j} \times \boldsymbol{b}$ heating by very intense laser light. *Phys. Fluids*, 28:430–432, 1985.

[31] S. C. Wilks, W. L. Kruer, M. Tabak, and A. B. Langdon. Absorption of ultra-intense laser pulses. *Phys. Rev. Lett.*, 69:1383–1386, 1992.

[32] J. Jackson. *Classical Electrodynamics*. Wiley, New York, 1998.

[33] F. Ráksi, K. R. Wilson, Z. Jiang, A. Ikhlef, Ch. Y. Côté, and J.-C. Kieffer. Ultrafast x-ray absorption probing of a chemical reaction. *J. Chem. Phys.*, 104:6066–6069, 1996.

[34] A. C. Thompson. *X-ray data booklet*. Center for x-ray optics and advanced light source Lawrence Berkeley National Laboratory, Berkeley, Ca, 2001.

[35] Ch. Reich, P. Gibbon, I. Uschmann, and E. Förster. Yield optimization and time structure of femtosecond laser plasma Kα sources. *Phys. Rev. Lett.*, 84:4846–4849, 2000.

[36] M. Green and V. E. Cosslett. Measurements of K, L and M shell x-ray production efficiencies. *J. Phys. D*, 1:425–436, 1968.

[37] C. Rischel, A. Rousse, I. Uschmann, P.-A. Albouy, J.-P. Geindre, P., Audebert, E. Frster, J.-C. Gauthier, J.-L. Martin, and A. Antonetti. Femtosecond time-resolved x-ray diffraction from laser-heated organic films. *Nature*, 390:490–492, 1997.

[38] T. Feurer, A. Morak, I. Uschmann, Ch. Ziener, H. Schwoerer, E. Forster, and R. Sauerbrey. An incoherent sub-picosecond x-ray source for time-resolved x-ray-diffraction experiments. *Appl. Phys. B*, 72:15–20, 2001.

[39] A. Rousse, C. Rischel, S. Fourmaux, I. Uschmann, S. Sebban, G. Grillon, Ph. Balcou, E. Förster, J.-P. Geindre, P. Audebert, J.-C. Gauthier, and D. Hulin. Non-thermal melting in semiconductors measured at femtosecond resolution. *Nature*, 410:65–68, 2001.

[40] C.W. Siders, A. Cavalleri, K. Sokolowski-Tinten, Cs. Tóth, T. Guo, M. Kammler, M. Horn von Hoegen, K.R. Wilson, D. von der Linde, and C.P.J. Barty. Detection of nonthermal melting by ultrafast x-ray diffraction.

[41] D. Von der Linde and K. Sokolowski-Tinten. X-ray diffraction experiments with femtosecond time resolution. *Journal of Modern Optics*, 50:683–694, 2003.

[42] M. Bargheer, N. Zhavoronkov, M. Woerner, and T. Elsaesser. Recent progress in ultrafast x-ray diffraction. *Chem. Phys. Chem*, 7:783–792, 2006.

[43] A. Bonvalet, A. Darmon, J.-Ch. Lambry, J.-L. Martin, and P. Audebert. 1 khz tabletop ultrashort hard x-ray source for time-resolved x-ray protein crystallography. *Opt. Lett.*, 31:2753–2755, 2006.

[44] J. D. Kmetec, C. L. Gordon, J. J. Macklin, B. E. Lemoff, G. S. Brown, and S. E. Harris. Mev x-ray generation with a femtosecond laser. *Phys. Rev. Lett.*, 68:1527–1530, 1992.

[45] J. Yu, Z. Jiang, J.C. Kieffer, and A. Krol. Hard x-ray emission in high intensity laser-target interaction. *Phys. Plasmas*, 6:1318–1322, 1999.

[46] G. Pretzler, F. Brandl, J. Stein, E. Fill, and J. Kuba. High-intensity regime of x-ray generation from relativistic laser plasmas. *Appl. Phys. Lett.*, 82:3623–3625, 2003.

[47] K.-H. Hong, B. Hou, J. Nees, E. Power, and G. A. Mourou. Generation and measurement of $> 10^8$ intensity contrast ratio in a relativistic khz chirped-pulse amplified laser. *Appl. Phys. B*, 81:447–457, 2005.

[48] O. Albert, H. Wang, D. Liu, Z. Chang, and G. Mourou. Generation of relativistic intensity pulses at a kilohertz repetition rate. *Opt. Lett.*, 25:1125–1127, 2000.

[49] P. D. Rockett, C. R. Bird, C. J. Hailey, D. Sullivan, D. B. Brown, and P. G. Burkhalter. X-ray calibration of kodak direct exposure film. *Applied Optics*, 24:2536–2542, 1985.

[50] N. E. Lanier, J. S. Cowan, and J. Workman. Characterization and cross calibration of agfa d4, d7, and d8 and kodak sr45 x-ray films against direct exposure film at 4.0–5.5 kev. *Rev. Sci. Instrum.*, 77:043504, 2006.

[51] A. Thompson *et al. X-ray data booklet.* Lawrence Berkeley National Laboratory, Berkeley, Ca, 2001.

[52] B. Hou, A. Mordovanakis, A. Krol, J.-C. Kieffer, G. Mourou, and J. Nees. Characterization of a compact hard x-ray source driven by a relativistic wavelength-cubed laser. In *Conference on Lasers and Electro-Optics/Quantum Electronics & Laser Science (CLEO/QELS)*, May 21-26 2006.

[53] M. Schnurer, M. P. Kalachnikov, P. V. Nickles, Th. Schlegel, W. Sandner, N. Demchenko, R. Nolte, and P. Ambrosi. Hard x-ray emission from intense short pulse laser plasmas. *Phys. Plasmas*, 2:3106–3110, 1995.

[54] B. N. Chichkov, C. Momma, A. Tünnermann, S. Meyer, T. Menzel, and B. Wellegehausen. Hard-x-ray radiation from short-pulse laser-produced plasmas. *Appl. Phys. Lett.*, 68:2804–2806, 1996.

[55] J. Badziak, J. Makowski, P. Parys, L. Ryc, J. Wolowski, E. Woryna, and A. B. Vankov. Intensity-dependent characteristics of a picosecond laser-produced cu plasma. *J. Phys. D: Applied Physics*, 34:1885–1891, 2001.

[56] K.-H. Liao, M.-Y. Cheng, E. Flecher, V. I. Smirnov, L. B. Glebov, and A. Galvanauskas. Large-aperture chirped volume bragg grating based fiber cpa system. *Opt. Express*, 15:4876–4882, 2007.

[57] K.-H. Liao. *Novel devices for ultrashort pulse fiber laser technology.* PhD thesis, University of Michigan, 2007.

[58] H.-S. Park, D.M. Chambers, H.-K. Chung, R.J. Clarke, R. Eagleton, E. Giraldez, T. Goldsack, R. Heathcote, N. Izumi, M.H. Key, J.A. King, J.A. Koch, O.L. Landen, A. Nikroo, P.K. Patel, D.F. Price, B.A. Remington, H.F. Robey, R.A. Snavely, D.A. Steinman, R.B. Stephens, C. Stoeckl, M. Storm, M. Tabak, W. Theobald, R.P.J. Town, J.E. Wickersham, and B.B. Zhang. High-energy K_α radiography using high-intensity short-pulse lasers. *Phys. Plasmas*, 13:056309, 2006.

[59] R. B. Stephens, R. A. Snavely, Y. Aglitskiy, F. Amiranoff, C. Andersen, D. Batani, S. D. Baton, T. Cowan, R. R. Freeman, T. Hall, S. P. Hatchett, J. M. Hill, M. H. Key, J. A. King, J. A. Koch, M. Koenig, A. J. MacKinnon, K. L. Lancaster, E. Martinolli, P. Norreys, E. Perelli-Cippo, M. Rabec Le Gloahec, C. Rousseaux, J. J. Santos, and F. Scianitti. k_α fluorescence measurement of relativistic electron transport in the context of fast ignition. *Phys. Rev. E*, 69(6):066414, 2004.

[60] M. Born and E. Wolf. *Principles of Optics*. Cambridge University Press, Cambridge, 1999.

[61] J. Goodman. *Statistical Optics*. Wiley-Interscience, New York, 2000.

[62] L. Mandel and E. Wolf. *Optical Coherence and Quantum Optics*. Cambridge University Press, Cambridge, 1995.

[63] J. E. Trebes, K. A. Nugent, S. Mrowka, R. A. London, T. W. Barbee, M. R. Carter, J. A. Koch, B. J. MacGowan, D. L. Matthews, L. B. Da Silva, G. F. Stone, and M. D. Feit. Measurement of the spatial coherence of a soft-x-ray laser. *Phys. Rev. Lett.*, 68:588, 1992.

[64] I.C.E. Turcu, I. N. Ross, M.S. Schulz, H. Daido, G. J. Tallents, J. Krishnan, L. Dwivedi, and L. Hening. Spatial coherence measurements and x-ray holographic imaging using a laser-generated plasma x-ray source in the water window spectral region. *J. Appl. Phys.*, 73:8081, 1993.

[65] T. Ditmire, E. T. Gumbrell, R. A. Smith, J. W. G. Tisch, D. D. Meyerhofer, and M. H. R. Hutchinson. Spatial coherence measurement of soft x-ray radiation produced by high order harmonic generation. *Phys. Rev. Lett.*, 77:4756–4759, 1996.

[66] A. Rousse, P. Audebert, J. P. Geindre, F. Falliès, J. C. Gauthier, A. Mysyrowicz, G. Grillon, and A. Antonetti. Efficient k_α x-ray source from femtosecond laser-produced plasmas. *Phys. Rev. E*, 50:2200–2207, 1994.

[67] A. Snigirev, I. Snigireva, V. Kohn, S. Kuznetsov, and I. Schelokov. On the possibilities of x-ray phase contrast microimaging by coherent high-energy synchrotron radiation. *Rev. Sci. Instrum.*, 66:5486–5492, 1995.

[68] S. W. Wilkins, T. E. Gureyev, D. Gao, A. Pogany, and A. W. Stevenson. Phase-contrast imaging using polychromatic hard x-rays. *Nature*, 384:335 – 338, 1996.

[69] K. A. Nugent, T. E. Gureyev, D. F. Cookson, D. Paganin, and Z. Barnea. Quantitative phase imaging using hard x rays. *Phys. Rev. Lett.*, 77:2961–2964, 1996.

[70] R. Toth, J.C. Kieffer, S. Fourmaux, T. Ozaki, and A. Krol. In-line phase-contrast imaging with a laser-based hard x-ray source. *Rev. Sci. Instrum.*, 76:083701–0837067, 2005.

[71] R. Kodama, P. A. Norreys, K. Mima, A. E. Dangor, R.G. Evans, H. Fujita, Y. Kitagawa, K. Krushelnick, T. Miyakoshi, N. Miyanaga, T. Norimatsu, S.J. Rose, T. Shozaki, K. Shigemori, A. Sunahara, M. Tampo, K.A. Tanaka, Y. Toyama, Y. Yamanaka, and M. Zepf. Fast heating of ultrahigh-density plasma as a step towards laser fusion ignition. *Nature*, 412:798–802, 2001.

[72] R. Kodama. Nuclear fusion - fast heating scalable to laser fusion ignition. *Nature*, 418:933–934, 2002.

[73] E.E. Fill, S. Trushin, R. Bruch, and R. Tommasini. Diffraction of laser-plasma-generated electron pulses. *Appl. Phys. B*, 81:155 – 157, 2005.

[74] C. Gahn, G. D. Tsakiris, G. Pretzler, K. J. Witte, P. Thirolf, D. Habs, C. Delfin, and C.-G. Wahlström. Generation of mev electrons and positrons with femtosecond pulses from a table-top laser system. *Phys. Plasmas*, 9:987–287, 2002.

[75] H. Chen, S. C. Wilks, P. K. Patel, and R. Shepherd. Generation of mev electrons and positrons with femtosecond pulses from a table-top laser system. *Rev. Sci. Instrum.*, 77:10E703–1 – 10E703–3, 2006.

[76] J. Miyahara, K. Takahashi, Y. Amemiya, N. Kamiya, and Y. Satow. A new type of x-ray area detector utilizing laser stimulated luminescence. *Nuclear Instruments and Methods in Physics Research Section A*, 246(1-3):572–578, 1986.

[77] Kazuo A. Tanaka, Toshinori Yabuuchi, Takashi Sato, Ryosuke Kodama, Yoneyoshi Kitagawa, Teruyoshi Takahashi, Toshiji Ikeda, Yoshihide Honda, and Shuuichi Okuda. Calibration of imaging plate for high energy electron spectrometer. *Rev. Sci. Instrum.*, 76(1):013507, 2005.

[78] M. A. Waggoner. Internal conversion of gamma-ray from cs^{137}. *Phys. Rev.*, 80(3):489, Nov 1950.

[79] J. Easter, B. Hou, E. Power, G. Mourou, and J. Nees. High-contrast millijoule regenerative amplifier. *Rev. Sci. Instrum.*, In preparation.

[80] J. Easter, B. Hou, E. Power, G. Mourou, and J. Nees. Large mode area regenerative amplifier with 10^{-11} ase contrast. In *Conference on Lasers and Electro-Optics/Quantum Electronics & Laser Science (CLEO/QELS)*, May 6-11 2007.

[81] F. N. Beg, A. R. Bell, A. E. Dangor, C. N. Danson, A. P. Fews, M. E. Glinsky, B. A. Hammel, P. Lee, P. A. Norreys, and M. Tatarakis. A study of picosecond laser-solid interactions up to 10^{19} Wcm^{-2}. *Phys. of Plasmas*, 4:447–457, 1997.

[82] N. Zhavoronkov, Y. Gritsai, M. Bargheer, M. Woerner, and T. Elsaesser. Generation of ultrashort ka radiation from quasipoint interaction area of femtosecond pulses with thin foils. *Appl. Phys. Lett.*, 86:244107, 2005.

[83] J. T. Larsen and S. M. Lane. Hyadesa plasma hydrodynamics code for dense plasma studies. *J. Quant. Spectrosc. Radiat.*, 51:179–186, 1994.

[84] G. I. Dudnikova, V. Yu. Bychenkov, A. Maksimchuk, G. Mourou, J. Nees, S. G. Bochkarev, and V. A. Vshivkov. Electron acceleration by few-cycle laser pulses with single-wavelength spot size. *Phys. Rev. E*, 67, 2003.

[85] A. G. Zhidkov, A. Sasaki, I. Fukumoto, T. Tajima, T. Auguste, P. D'Oliveira, S. Hulin, P. Monot, A. Ya. Faenov, T. A. Pikuz, and I. Yu. Skobelev. Pulse duration effect on the distribution of energetic particles produced by intense femtosecond laser pulses irradiating solids. *Physics of Plasmas*, 8:3718–3723, 2001.

[86] U. Teubner, P. Gibbon, E. Förster, F. Falliès, P. Audebert, J. P. Geindre, and J. C. Gauthier. Subpicosecond krf-laser plasma interaction at intensities between 10^{14} and 10^{17} w/cm^2. *Phys. of Plasmas*, 3:2679–2685, 1996.

[87] S. Bastiani, A. Rousse, J. P. Geindre, P. Audebert, C. Quoix, G. Hamoniaux, A. Antonetti, and J. C. Gauthier. Experimental study of the interaction of subpicosecond laser pulses with solid targets of varying initial scale lengths. *Phys. Rev. E*, 56:7179–7185, 1997.

[88] Y. Sentoku, H. Ruhl, K. Mima, R. Kodama, K. A. Tanaka, and Y. Kishimoto. Plasma jet formation and magnetic-field generation in the intense laser plasma under oblique incidence. *Phys. of Plasmas*, 6:2855–2861, 1999.

[89] T. Nakamura, S. Kato, H. Nagatomo, and K. Mima. Surface-magnetic-field and fast-electron current-layer formation by ultraintense laser irradiation. *Phys. Rev. Lett.*, 93:265002, 2004.

[90] Z.-M. Sheng, Y. Sentoku, K. Mima, J. Zhang, W. Yu, and J. Meyer ter Vehn. Angular distributions of fast electrons, ions, and bremsstrahlung X/γ-rays in intense laser interaction with solid targets. *Phys. Rev. Lett.*, 85:5340–5343, 2000.

[91] C. Serbanescu. *K-alpha x-Ray and hot electron emission from microjoule femtosecond laser produced plasmas*. PhD thesis, University of Alberta, 2007.

[92] D. F. Cai, Y. Q. Gu, Z. J. Zheng, T. S. Wen, S. T. Chunyu, Z. B. Wang, and X. D. Yang. Experimental study for angular distribution of the hot electrons generated by femtosecond laser interaction with solid targets. *Physics of Plasmas*, 10:3265–3269, 2003.

[93] M. I. K. Santala, M. Zepf, I. Watts, F. N. Beg, E. Clark, M. Tatarakis, K. Krushelnick, A. E. Dangor, T. McCanny, I. Spencer, R. P. Singhal, K. W. D. Ledingham, S. C. Wilks, A. C. Machacek, J. S. Wark, R. Allott, R. J. Clarke, and P. A. Norreys. Effect of the plasma density scale length on the direction of fast electrons in relativistic laser-solid interactions. *Phys. Rev. Lett.*, 84:1459–1462, 2000.

[94] H. Ruhl, Y. Sentoku, K. Mima, K. A. Tanaka, and R. Kodama. Collimated electron jets by intense laser-beam plasma surface interaction under oblique incidence. *Phys. Rev. Lett.*, 82(4):743–746, Jan 1999.

[95] R. Kodama, K. A. Tanaka, Y. Sentoku, T. Matsushita, K. Takahashi, H. Fujita, Y. Kitagawa, Y. Kato, T. Yamanaka, and K. Mima. Long-scale jet formation with specularly reflected light in ultraintense laser-plasma interactions. *Phys. Rev. Lett.*, 84(4):674–677, Jan 2000.

[96] Z. Li, H. Daido, A. Fukumi, A. Sagisaka, K. Ogura, M. Nishiuchi, S. Orimo, Y. Hayashi, M. Mori, M. Kado, S. V. Bulanov, T. Zh. Esirkepov, Y. Oishi, T. Nayuki, T. Fujii, K. Nemoto, S. Nakamura, and A. Noda. Measurements of energy and angular distribution of hot electrons and protons emitted from a p- and s-polarized intense femtosecond laser pulse driven thin foil target. *Physics of Plasmas*, 13(4):043104, 2006.

[97] Y. T. Li, X. H. Yuan, M. H. Xu, Z. Y. Zheng, Z. M. Sheng, M. Chen, Y. Y. Ma, W. X. Liang, Q. Z. Yu, Y. Zhang, F. Liu, Z. H. Wang, Z. Y. Wei, W. Zhao, Z. Jin, and J. Zhang. Observation of a fast electron beam emitted along the surface of a target irradiated by intense femtosecond laser pulses. *Phys. Rev. Lett.*, 96(16):165003, 2006.

[98] Y. Sentoku, K. Mima, H. Ruhl Y. Toyama, R. Kodama, and T.E. Cowan. Laser light and hot electron micro focusing using a conical target. *Phys. of Plasmas*, 11:3083–3087, 2004.

[99] H. Habara, K. Adumi, T. Yabuuchi, T. Nakamura, Z. L. Chen, M. Kashihara, R. Kodama, K. Kondo, G. R. Kumar, L. A. Lei, T. Matsuoka, K. Mima, and K. A. Tanaka. Surface acceleration of fast electrons with relativistic self-focusing in preformed plasma. *Physical Review Letters*, 97(9):095004, 2006.

[100] A. Galvanauskas. High power fiber lasers. *Opt. Photonics News*, 15:42–47, 2004.

[101] J. Sakai and T. Kimura. Bending loss of propagation modes in arbitrary index profile optical fibers. *Appl. Opt.*, 17:1499–1506, 1978.

[102] M. E. Fermann. Single-mode excitation of multimode fibers with ultrashort pulses. *Opt. Lett.*, 23:52–54, 1998.

[103] F. Röser, J. Rothhard, B. Ortac, A. Liem, O. Schmidt, T. Schreiber, J. Limpert, and A. Tünnermann. 131 w 220 fs fiber laser system. *Opt. Lett.*, 30:2754–2756, 2005.

[104] A. Galvanauskas, M.-Y. Cheng, K.-C. Hou, and K.-H. Liao. High peak power pulse amplification in large-core yb-doped fiber amplifiers. *IEEE J. Sel. Top. Quantum Electron.*, 13:559–566, 2007.

[105] V.T. Jordanov, J.A. Pantazis, and A.C. Huber. Thermoelectrically-cooled cadmium zinc telluride detectors (CZT) for x-ray and gamma-ray detection. *Radiation*, 43:–, 1996.

[106] A.C. Huber, J.A. Pantazis, and V.T. Jordanov. High performance, thermoelectrically cooled x-ray and gamma ray detectors. *Nuclear Instruments and Methods in Physics Research Section B*, 99:665–668, 1995.

[107] M.O. Krause and J. H. Oliver. Natural widths of atomic k and l levels, kα x-ray lines, and several kll auger lines. *J. Phys. Chem. Ref. Data*, 8:329 – 329, 1979.

[108] M. Hagedorn, J. Kutzner, G. Tsilimis, and H. Zacharias. High-repetition-rate hard x-ray generation with sub-millijoule femtosecond laser pulses. *Appl. Phys. B*, 77:49–57, 2003.

[109] F. He, J. H. V. Price, A. Malinowski, A. Piper, M. Ibsen, D. J. Richardson, J. W. Dawson, C. W. Siders, and Ch. P. J. Barty. High average power, high energy, femto-second fiber chirped pulse amplification system. In *Conference on Lasers and Electro-Optics*, page paper CMEE5, May 6-11 2007.

[110] O. M. Efimov, L. B. Glebov, and V. I. Smirnov. High-frequency Bragg gratings in a photothermorefractive glass. *Opt. Lett.*, 25:1693–1695, 2000.

[111] Q. Chang, C.-H. Liu, K.-H. Liao, V. Smirnov, L. Glebov, and A. Galvanauskas. 50 w chirper volume bragg grating based fiber cpa at 1055 nm. In *Conference on Lasers and Electro-Optics/Quantum Electronics & Laser Science (CLEO/QELS)*, page paper CMEE4, May 6-11 2007.

[112] T. H. Loftus, A. Liu, P. R. Hoffman, A. M. Thomas, M. Norsen, R. Royse, and E. Honea. 522 w average power, spectrally beam-combined fiber laser with near-diffraction-limited beam quality. *Opt. Lett.*, 32:349–351, 2007.

[113] J. Anderegg, S.J. Brosnan, M. E. Weber, H. Komine, and M.G. Wickam. 8-w coherently phased 4-element fiber array. In L.N. Durvasula, editor, *Advances in Fiber Lasers*, volume 4974 of *Proc. SPIE*, pages 1–6, 2003.

[114] E. Cheung, M. Weber, and D. Mordaunt. Mode-locked pulsed fiber array scalable to high power. In L.N. Durvasula, editor, *Fiber Laser: Technology, Systems, and applications*, volume 5335 of *Proc. SPIE*, 2003.

[115] G. A. Mourou, D. Hulin, and A. Galvanauskas. The road to high peak power and high average power lasers: Coherent-amplification-network (can). In M. Lontano and D. Batani, editors, *Third International Conference on Superstrong Fields in Plasmas*, volume 827 of *Superstrong Fields in Plamsas*, pages 152–163, 2006.

[116] D. Attwood. *Soft x-rays and extreme ultraviolet radiation : principles and applications*. Cambridge University Press, Cambridge, New York, 2000.

[117] D. Brandt. Laser-produced plasma presents most viable route to EUV lithography. *Laser Focus World*, 43:66–67, 2007.

[118] B. J. Lin. Sober view on extreme ultraviolet lithography. *J. Microlith., Microfab., Microsyst.*, 5:033005, 2006.

[119] K. Kemp and S. Wurm. EUV lithography. *C. R. Physique*, 7:875–886, 2006.

[120] J. Jonkers. High power extreme ultra-violet (EUV) light sources for future lithography. *Plasma Sources Sci. and Technol.*, 15:8–16, 2006.

[121] A. A. Andreev, J. Limpouch, N. B. Voznesensky, A. P. Zhevlakov, and V. E. Yashin. Enhancement of laser/euv conversion by shaped laser pulse interacting with li-contained targets for euv lithography. In G. A. Kyrala, J.-C. J. Gauthier, C. A. MacDonald, and A. M. Khounsary, editors, *Laser-Generated and Other Laboratory X-Ray and EUV Sources, Optics, and Applications*, volume 5196 of *Proc. SPIE*, pages 128–136. SPIE, 2004.

[122] W. N. Partlo, I. V. Fomenkov, and D. L. Birx. EUV (13.5-nm) light generation using a dense plasma focus device. In Yuli Vladimirsky, editor, *Emerging Lithographic Technologies III*, volume 3676 of *Proc. SPIE*, pages 846–858. SPIE, 1999.

[123] F. Jin and M. Richardson. New laser plasma source for extreme-ultraviolet lithography. *Appl. Opt.*, 34:5750–5751, 1995.

[124] M. A. Klosner and W. T. Silfvast. Xenon-emission-spectra identification in the 5–20-nm spectral region in highly ionized xenon capillary-discharge plasmas. *J. Opt. Soc. Am. B*, 17(7):1279–1290, 2000.

[125] Y. Ueno, T. Ariga, G. Soumagne, T. Higashiguchi, S. Kubodera, I. Pogorelsky, I. Pavlishin, D. Stolyarov, M. Babzien, K. Kusche, and V. Yakimenko. Efficient extreme ultraviolet plasma source generated by a CO[sub 2] laser and a liquid xenon microjet target. *Appl. Phys. Lett.*, 90:191503, 2007.

[126] B. A. M. Hansson and H. M Hertz. Liquid-jet laser-plasma extreme ultraviolet sources: from droplets to filaments. *J. of Phys. D: Appl. Phys.*, 37(23):3233–3243, 2004.

[127] R. C. Spitzer, T. J. Orzechowski, D. W. Phillion, R. L. Kauffman, , and C. Cerjan. Conversion efficiencies from laser-produced plasmas in the extreme ultraviolet regime. *J. Appl. Phys.*, 79:2251, 1996.

[128] D. C. Brandt, I. V. Fomenkov, A. I. Ershov, W. N. Partlo, D. W. Myers, N. R. Böwering, A. N. Bykanov, G. O. Vaschenko, O. V. Khodykin, J. R. Hoffman, E. L. Vargas, R. D. Simmons, J. A. Chavez, and C. P. Chrobak. LPP EUV source development for HVM. In M. J. Lercel, editor, *Emerging Lithographic Technologies XI*, volume 6517 of *Proc. SPIE*, page 65170Q, 2007.

[129] K. Takenoshita, S. A. George, T. Schmid, C.-S. Koay, J. Cunado, R. Bernath, Ch. Brown, M. M. Al-Rabban, W. T. Silfvast, and M. C. Richardson. Characterization of the tin-doped droplet laser plasma EUVL sources for HVM. In Michael J. Lercel, editor, *Emerging Lithographic Technologies XI*, volume 6517 of *Proc. SPIE*, page 651730. SPIE, 2007.

[130] S. A. George, W. T. Silfvast, K. Takenoshita, R. T. Bernath, C.-S. Koay, G. Shimkaveg, and M. C. Richardson. Comparative extreme ultraviolet emission measurements for lithium and tin laser plasmas. *Opt. Lett.*, 32:997–999, 2007.

[131] C.-S. Koay, S. George, K. Takenoshita, R. Bernath, E. Fujiwara, M. Richardson, , and V. Bakshi. High conversion efficiency microscopic tin-doped droplet target laser-plasma source for EUVL. In R. S. Mackay, editor, *Emerging Lithographic Technologies IX*, volume 5751 of *Proc. SPIE*, page 279, 2005.

[132] T. Tomie, T. Aota, Y. Ueno, G. Niimi, H. Yashiro, J. Q. Lin, I. Matsushima, K. Komiyama, D.-H. Lee, K. Nishigori, and Hiroshi Yokota. Use of tin as a plasma source material for high conversion efficiency. In R. L. Engelstad, editor, *Emerging Lithographic Technologies VII*, volume 5037 of *Proc. SPIE*, page 147, 2003.

[133] H. Komori, Y. Ueno, H. Hoshino, T. Ariga, G. Soumagne, A. Endo, and H. Mizoguchi. EUV radiation characteristics of a CO2 laser produced Xe plasma. *Appl. Phys. B*, 83:213–218, 2006.

[134] M.-Y. Cheng, Y.-C. Chang, A. Galvanauskas, P. Mamidipudi, R. Changkakoti, and P. Gatchell. High-energy and high-peak-power nanosecond pulse generation with beam quality control in 200-mm core highly multimode Yb-doped fiber amplifiers. *Opt. Lett.*, 30:358, 2005.

[135] T. Kita, T. Harada, N. Nakano, and H. Kuroda. Mechanically ruled aberration-corrected concave gratings for a flat-field grazing-incidence spectrograph. *Appl. Opt.*, 22:512–513, 1983.

[136] N. Nakano, H. Kuroda, T. Kita, and T. Harada. Developement of a flat-field grazing-incidence XUV spectrometer and its application in picosecond xuv spectroscopy. *Appl. Opt.*, 23:2386–2392, 1984.

[137] M. Krumrey, E. Tegeler, J. Barth, M. Krisch, F. Schäfers, and R. Wolf. Schottky type photodiodes as detectors in the VUV and soft x-ray range. *Appl. Opt.*, 27:4336–4336, 1998.

[138] J. F. Meekins, R. G. Cruddace, and H. Gursky. Optimization of layered synthetic microstructures for narrowband reflectivity at soft x-ray and EUV wavelengths. *Appl. Opt.*, 25:2757–2763, 1986.

[139] E. Spiller, S. L. Baker, P. B. Mirkarimi, V. Sperry, E. M. Gullikson, and D. G. Stearns. High-performance Mo-Si multilayer coatings for extreme-ultraviolet lithography by ion-beam deposition. *Appl. Opt.*, 42:4049–4058, 2003.

[140] K.-C. Hou, S. George, A. G. Mordovanakis, K. Takenoshita, J. Nees, B. Lafontaine, M. Richardson, and A. Galvanauskas. High power fiber laser driver for efficient EUV lithography source with tin-doped water droplet targets. *Opt. Express*, 16:965–974, 2008.

[141] S. A. George, K.-C. Hou, K. Takenoshita, A. Galvanauskas, and M. C. Richardson. 13.5 nm EUV generation from tin-doped droplets using a fiber laser. *Opt. Express*, 15:16348–16356, 2007.